ALMA MATER STUDIORUM
UNIVERSITÀ DI BOLOGNA

DOTTORATO DI RICERCA IN

SCIENZE E TECNOLOGIE DELLA SALUTE

Ciclo 37

Settore Concorsuale: 09/E1 - ELETTROTECNICA

Settore Scientifico Disciplinare: ING-IND/31 - ELETTROTECNICA

CHARACTERIZATION OF A COLD ATMOSPHERIC PLASMA GENERATED BY CUSTOM-DESIGNED DIELECTRIC BARRIER DISCHARGE REACTOR FOR BIOAEROSOL DECONTAMINATION

Presentata da: Silvia Giuditta Scaltriti

Coordinatore Dottorato

Igor Diemberger

Supervisore

Gabriele Neretti

Co-supervisore

Gianandrea Pasquinelli

Esame finale anno 2025

Acknowledgements

Alla mia famiglia. A mio padre e a mia madre che hanno permesso letteralmente tutto questo. che mi hanno sostenuta dal primo giorno ma che soprattutto mi hanno sempre insegnato a non mollare mai e a mettermi sempre in gioco, nel bene e nel male. Che dire, questa tesi è anche vostra. A mia sorella, che è sempre stata l'esempio di ciò che vorrei essere, capace di reinventarsi sempre e mai stanca di trovare nuovi stimoli. Grazie a tutti voi. Vi voglio bene. Un grazie anche a Chuck che con la sua energia positiva è sempre pronto a strapparti un sorriso. Ai miei nonni, Laura, Livio e Savina, che anche se non sono presenti, sono sicura che stanno vegliando su di me con orgoglio, ovunque siano.

Vorrei ora ringraziare me stessa in primis, per essere arrivata fino in fondo nonostante i momenti di sconforto e frustrazione, immancabili durante un percorso di ricerca, la cui assenza potrebbe indicare che qualcosa è andato storto. Ma soprattutto vorrei ringraziare Gabriele, il mio supervisore, che con la sua mente geniale e la sua genuina simpatia ha sempre alleggerito quei momenti di abbattimento e sempre trovato una via per ripartire. Sono molto grata di essere stata sotto la sua ala in questi anni, dove grazie a lui ho imparato molto ed ho scoperto un amico che so mi accompagnerà ancora per un po' (sicuramente finchè non pubblichiamo l'articolo! ;).

Non so nemmeno come iniziare a ringraziare Voi, voi che ci siete davvero sempre state e che non so immaginare il mio percorso senza di voi, senza le nostre sessioni di studio, le nostre bevute (forse troppe?), le risate e i pianti che ci hanno accompagnato ogni giorno. Maddoz, Ele e Li, GRAZIE. Vi voglio bene. Un grande grazie a tutte le persone che ho conosciuto in questi anni, che in qualche modo hanno fatto parte di questo lungo percorso, anche solo con un consiglio, un sorriso o una pacca sulla spalla quando ce ne è stato bisogno. Siete davvero tanti e impossibili da nominare uno ad uno, ma anche solo il fatto che stiate leggendo questi ringraziamenti, vuole dire che siete una di quelle persone. Un ringraziamento speciale a Sos, che oltre ad avermi introdotto al mondo tossico di League of Legends, è stata una perfetta transizione tra i coinquilini storici, e l'inizio del dottorato.

Now I switch to English because I want to wholeheartedly thank Ivo for welcoming me into his laboratory and allowing me to carry out literally all the experiments that compose my research. I continue by thanking all the people I met at SPC, you are too many to thank, but a special thanks goes to my colleagues from the Hike and Beer Consortium, where the beer quota has definitely exceeded the hike. Thank you for accompanying me during this crazy last year, we will meet again very soon.

A special thanks to Rita, Lore, Leo, Simon and Felicio (I'm writing in English only because you haven't learned Italian yet, come on man!). You have been fundamental both inside and outside the laboratory, and I don't know how to thank you enough; You guys have made my stay in Switzerland truly magical, something I'll always cherish.

Per ultimo, ma non in termini di importanza, voglio ringraziare Te, Bronz. Difficile elencare i motivi per cui ti voglio ringraziare, e non volendo cadere nell'ovvio non mi dilungherò su cose che sai già, ma voglio dirti che la tua attitudine alla vita mi ha sempre spronato a volere qualcosa di più, a ricercare sempre il posto migliore che potessi trovare e a pormi sempre nuove sfide. Il fatto che io abbia accettato di iniziare il dottorato e sia riuscita ad arrivare in fondo a questa follia è davvero merito anche della tua persona. Vorrei dire tante cose, ma a volte basta davvero poco e la semplicità è la cosa migliore. Grazie. Grazie per tutto. Grazie per essere sempre al mio fianco. Grazie di essere la persona che sei.

Concludo dicendo che ogni traguardo è solo l'inizio di un nuovo viaggio verso nuove sfide. È grazie a tutti voi se sono arrivato fin qui, e spero davvero che continuiate a supportarmi (e sopportarmi) ancora a lungo. Come disse T.S. Eliot: *"To make an end is to make a beginning. The end is where we start from"*.

Grazie, per tutto

Abstract

Cold Atmospheric Plasma (CAP) based technology represents a promising approach for the disinfection and reduction of bioaerosols. CAP, also known as non-thermal plasma (NTP), generates a mixture of ions, electrons, and reactive species at room temperature, making it suitable for various applications without damaging materials. This technology works by exposing bioaerosols to the plasma discharge area, leading to the inactivation of microorganisms through mechanisms such as cell membrane disruption and oxidative stress. Studies have shown that cold plasma devices are effective in reducing airborne bacteria, viruses, and fungal spores. Nevertheless, few studies focus on plasma reactors specifically dedicated to the treatment of contaminated air. In this context, the development of a CAP reactor, named GAPS - Grid-like Air Plasma Sanitizer, for bioaerosol treatment could represents a promising advancement in these field. This study presents the design, development, and comprehensive characterization of a novel Dielectric Barrier Discharge (DBD) reactor, GAPS, specifically engineered for continuous bioaerosol treatment. The research aimed to optimize the interaction between CAP and bioaerosols and maximizing the inactivation efficiency. Electrical and fluid dynamic characterizations verified the GAPS stability and homogeneity. Computational Fluid Dynamics (CFD) simulations provided essential insights into airflow patterns, ensuring uniform bioaerosol distribution within the reactor chamber and effective plasma interaction with the airflow. At full capacity, the operating specific power was found to be $\simeq 0.014 W/cm^2$. Chemical analysis of the plasma environment, conducted using Fourier-transform infrared (FTIR) spectroscopy, identified the generation of reactive oxygen and nitrogen species (RONS), specifically ozone and Nitrous oxide. Under operational conditions, the device produced approximately 9 ppb of O_3 and less than 2 ppm for N_2O when the system reached steady-state conditions. The biological efficacy of the CAP DBD reactor was validated through microbial viability assays, which confirmed a significant reduction in aerosolized non-pathogenic *Escherichia Coli*, a well-known representative gram-negative bacteria. The CAP system achieved 4-log reduction within 25 ms of treatment. Notably, the reactor's Electrical Energy per Order

(EEO) was measured to be of $2x10^{-4}kWh/m^3$ per order, lower than other plasma-based air sanitization devices found in literature, indicating superior energy efficiency and cost-effectiveness for bacterial inactivation. While these results are promising, several challenges remain. Variability in bioaerosol composition and environmental conditions may affect disinfection efficacy, highlighting the need for further research to optimize reactor performance across different scenarios. Future studies should also focus on scaling the reactor for practical applications and enhancing energy efficiency to support broader use. Additionally, refining bioaerosol measurement set-up could improve inactivation potential, achieving greater microbial load reduction assessment. In summary, this thesis presents GAPS, a CAP-based reactor designed for air sanitization, demonstrating efficiency, efficacy, and stability. The results provide a basis for further research and potential integration into existing air purification systems. CAP technology remains a promising approach for improving indoor air quality, offering an energy-efficient method to mitigate airborne contaminants.

Contents

List of Abbreviations

AC	alternating current
BLAM	blaustein atomizing modules
CAD	computer-aided design
CAP	cold atmospheric plasma
CFD	computational fluid dynamics
CFU	colony-forming unit
DBD	dielectric barrier discharge
DC	direct current
DI	deionized water
EEO	electrical energy per order
ESP	electrostatic sampler
FTIR	fourier transform infrared spectroscopy
GAPS	grid-like air plasma sanitizer
HEPA	high efficiency particulate air
HV	high voltage
HVAC	heating, ventilation, and air conditioning.

LB	Luria-Bertani
LTP	low-temperature plasma
MERS	middle east respiratory syndrome
MOSFET	metal oxide semiconductor field-effect transistor
OD	optical density
PBR	packed bed reactor
PBS	phosphate-buffered saline
PCB	printed circuit board
PCO	photocatalytic oxidation
PU	Polyurethane
PWM	pulse width modulation
RH	relative humidity
RONS	reactive oxigen and nitrogen species
SAL	sterility assurance level
SARS	severe acute respiratory syndrome
SARS-CoV-2	severe acute respiratory syndrome coronavirus 2
SDBD	surface dielectric barrier discharge
SLAG	sparging liquid aerosol generator
SPA	single pass atomization
UV	ultraviolet
UV-C	germicidal UV
UVGI	ultraviolet germicidal irradiation
VDBD	volume dielectric barrier discharge
VOC	volatile compupaunds

WHO	world health organization

List of Symbols

Variables, parameters, and functions

$\dot{V}$	Air flow rate $[m^3/s]$
ϵ_r	Permittivity of the dielectric material
η_{impinger}	Sampling efficiency of the impinger [%]
$\eta_{\text{nebulizer}}$	Nebulization efficiency [%]
ν	Frequency of the infrared radiation [Hz]
$\sigma(\nu)$	Absorption cross-section per molecule at frequency ν [cm^2/molecule]
A	Absorbance
$A(\nu)$	Absorbance at frequency ν
C_{air}	Concentration of bacteria in the airflow [CFU/LPM]
C_{air}	Concentration of bacteria in the airflow [CFU/ml]
C_{impinger}	Concentration of bacteria inside the impinger [CFU/ml]
C_{initial}	Initial concentration inside the syringe [CFU/ml]
C_{input}	Initial concentration of bacteria in the syringe [CFU/ml]
Cl_2	Chlorine
D	Reciprocal of the lowest dilution factor

I	Transmitted radiant powers [W/m²]
$I(\nu)$	Radiant power ν
I_0	Incident radiant powers [W/m²]
j_1	Number of plates counted at the lowest dilution level
j_2	Number of plates counted at the next higher dilution level
L	Path length of absorption [cm]
n	Density of the absorbing species [molecules/cm^3]
n_0	Density of the gas [molecules/cm^3]
N_2	Nitrogen
N_2O	Nitrous oxide
n_i	Density of species i [ppm]
N_{colonies}	Cumulative count of colonies on all plates included in the counting process [CFU]
N_{impinger}	Total number of bacteria collected in the impinger [CFU]
N_{initial}	Total number of colonies in the initial solution [CFU]
N_{injected}	Total number of bacteria injected [CFU]
$N_{\text{nebulized}}$	Total number of bacteria nebulized [CFU]
NO_2	Nitrogen dioxide
O_2	Oxygen
O_3	Ozone
P_n	Cumulative count of colonies on all counted plates
Q_{dilution}	Dilution airflow rate [LPM]
$Q_{\text{nebulizer}}$	Airflow rate from the nebulizer [LPM]

Q_{total}	Total airflow rate after dilution [LPM]
$t_{\text{nebulization}}$	Nebulization time [min]
t_{sampling}	Sampling time [min]
t_{res}	Residence time inside reactor
T_r	Transmittance
$V_{\text{bioaerosol}}$	Volume traversed by the bioaerosol flow [m^3]
C_d	Value of the capacitance across the dielectric [F]
C_g	Value of the capacitance across the gas gap [F]
C_m	Value of the monitor capacitance [F]
C_{OFF}	Value of the DBD reactor capacitance without discharge [F]
i_m	Instantaneous value of the measured electric current [A]
i_z	Instantaneous value of the discharge current [A]
i_{dis}	Instantaneous value of the displacement current [A]
$P_{average}$	Average power [W]
Q	Instantaneous charge across a monitor capacitor [C]
$R(t)$	Variable resistance [Ω]
T	Period [s]
v_c	Instantaneous value of the voltage across monitor capacitor [V]
v_d	Instantaneous value of the voltage across the dielectric barriers [V]
v_g	Instantaneous value of the voltage across the gas gap [V]
v_m	Instantaneous value of the measured electric voltage [V]
v_{DBD}	Instantaneous value of the voltage across the DBD reactor [V]

W_c	Total stored energy [J]

Constant

$\dot{Q}_{\text{BLAM}}$	BLAM output flow rate [LPM]
$\dot{Q}_{\text{impinger}}$	Single impinger flow rate [LPM]
$\dot{Q}_{\text{tot}}$	Total bioaerosol flow rate inside the system [LPM]
$V_{\text{evaporated}}$	Volume of evaporated liquid [ml]
V_{impinger}	Initial volume of liquid in the impinger [ml]
V_{injected}	Volume of solution injected [ml]
$V_{\text{remaining}}$	Volume of liquid in the impinger after evaporation [ml]

Introduction

The epidemics of SARS, MERS and the recent pandemic SARS-CoV-2 have highlighted the critical importance of air quality and the need to develop effective methodologies to reduce the spread of infectious diseases. During the pandemic, numerous studies demonstrated that poorly ventilated indoor spaces significantly increased the risk of viral transmission [1]. This realization has driven a renewed focus on improving indoor air quality in public places such as schools, offices, healthcare facilities, as well as public transportation [2], and has led to the development of new technologies that will significantly impact our lives and contribute to healthier indoor environments post-pandemic.

To address the challenges posed by poor air quality, a variety of technologies are currently employed to enhance indoor air environments. Ventilation systems are designed to increase the rate of air exchange, thereby diluting the concentration of indoor pollutants and reducing the risk of airborne transmission. The technologies most commonly adopted for air sanitization in closed environments are High Efficiency Particulate Air (HEPA) filters [3] and ultraviolet germicidal irradiation (UVGI) [4]. HEPA filters can capture a wide range of airborne particles, including bacteria and viruses, helping to decrease the airborne concentration of small particles within a room (Hinds, 1999; Farnsworth et al., 2006), but filtering only affects the efficacy of the pathogen transport. UVGI is another widely adopted technology that uses UV-C light to inactivate microorganisms in the air and on surfaces, offering an additional layer of protection [5][4]. However, UVGI sanitization only reduces infectivity and requires compliance with specific threshold values regarding the intensity and exposure time to radiation produced by germicidal lamps. The efficiency of UV inactivation also depends on the susceptibility of the pathogen and often requires the prior collection of the pathogen on the surface of a HEPA filter. Air purifiers that combine HEPA filtration with activated carbon filters are also popular, as they can remove both particulate matter and volatile organic compounds (VOCs) from the air. Moreover, emerging technologies such as

Photocatalytic Oxidation (PCO) and bipolar ionization are gaining attention due to their potential to enhance air purification by breaking down contaminants at the molecular level, exploiting both UV light and a photocatalyst [6]. Recent reviews have thoroughly compared the advantages and drawbacks of conventional technologies with emerging methods[7].

Among emerging technologies, atmospheric pressure non-thermal plasma (NTP) generated by Dielectric Barrier Discharge (DBD) has attracted significant attention in the biomedical field over the past few decades. To refer to this technology the most common name are Low-Temperature Plasma (LTP) or Cold Atmospheric Plasma (CAP) . While the fundamental principles of an NTP reactor have been understood for more than a century, their applications in industrial and biomedical fields remain an active area of research, with continuous advancements expanding their potential [8]. In the context of sterilization and disinfection, NTP based technology presents highly promising results, indicating its potential as a future alternative to address current and upcoming challenges [9–11]. Among the various NTP reactor configurations, the DBD is the most widely used due to its homogeneous discharge, inherent electrical insulation, and energy efficiency, making it a dependable and reliable source for decontamination treatments [9].

Although CAP has been widely studied for surface sterilization [12], there is a noticeable lack of research focused on its use in air sanitization [13]. Currently, standardized protocols for bioaerosol inactivation are not well established, and significant research is needed to link the results of biological inactivation with the plasma properties of CAP devices [14]. Moreover, the processes for generating and sampling bioaerosols in laboratory settings lack standardized guidelines, which complicates the reproducibility and comparability of results across different laboratories [15].

Depending on the operative conditions, NTP produces a rich "cocktail" of reactive species, including reactive oxygen species (ROS) and reactive nitrogen species (RNS), electric fields, charged particles, and ultraviolet radiation (UVR), which have been shown to play pivotal roles in observed biomedical outcomes [16–18]. While the state of knowledge regarding plasma-generated agents is advanced, several subcellular and molecular mechanisms remain under debate or are not fully understood [19, 20]. Although multiple NTP reactor designs have demonstrated encouraging results for PBAs disinfection [10, 21–26], the reactors described are often far from being optimized. Indeed, the precise inactivation pathways of cold plasma remain partially unclear, but various factors, such as gas composition, reactor geometry, electrode configuration, direct/indirect treatment and power supply, undoubtedly influence the antimicrobial efficacy.

Previous studies, including those by Friedman et al., suggest that direct interaction between contaminated air and the plasma discharge zone achieves higher disinfection efficiency compared to relying solely on long-living reactive species like ozone [14, 27]. This observation underscores the importance of reactor designs that maximize direct contact between bioaerosols and the plasma zone.

The objective of this thesis is the design and characterization of a novel atmospheric-pressure DBD reactor intended for air disinfection, named **GAPS — Grid-like Air Plasma Sanitizer**. This involves creating a complete setup, from bioaerosol generation to sampling, to evaluate the device's efficacy. GAPS aims to maximize the plasma discharge and bioaerosol contact surface to enhance treatment efficiency. The research includes electrical characterization to determine power consumption, chemical analysis to identify the products and active agents involved in the disinfection process, and biological assessment to validate the treatment effectiveness of GAPS reactor.

The mechanism and design of the CAPs are introduced and explained in Section 1.2, following a brief overview of sanitization processes in Section 1.1. Additional details about the specific CAP device configuration used in this research are provided in Chapter 2.

Chapter 1.1 presents an introduction to bioaerosol microorganisms and disinfection with a focus on the existing guidelines and protocols on air quality. The chapter will explain how CAP technology can be a good alternative for bioaerosol disinfection and how this technology works.

Section 1.1 discusses the general aspects of bioaerosol inactivation, with subsections 1.1.1 and 1.1.2 providing a deeper insight into microorganisms and sterilization processes, respectively. Additionally, Section 1.1.3 provides an overview of various sterilization methods used for both surfaces and air. Following this, Chapter 1.2 introduces the concept of low-temperature plasma (CAP), focusing on its characteristics (Section 1.2.2) and different types of low-temperature plasma discharges (Section 1.2.3). Sections 1.2.4 and 1.2.5 explore the types of CAP devices and the application of dielectric barrier discharge (DBD) in bacterial inactivation.

Chapter 2 describes the experimental setup and methodologies used throughout the research. Section 2.1 covers bioaerosol nebulization, including the preparation of *Escherichia coli* solutions (Section 2.1.2). Section 2.2 focuses on bioaerosol sampling techniques, with a particular emphasis on CFU methods (Section 2.2.2) and quantification of antibacterial activity (Section 2.2.3). The bioaerosol treatment using a DBD reactor is described in Section 2.3, along with details on GAPS design (Section 2.3.1), power

supply design (Section 2.3.2), and chemical characterization of the treatment process (Section 2.3.4).

Chapter 3 presents the results obtained from the experimental investigations. Section 3.1 focuses on the physical characterization of the system, including power measurements (Section 3.1.1) and fluid dynamic characterization (Section 3.1.3). Section 3.2 examines the biological treatment of bioaerosols, while Section 3.3 evaluates the efficiency of GAPS, introducing the EEO index for performance analysis.

Finally, Chapter 4 concludes the thesis by summarizing the main findings and contributions and proposing directions for future research.

Chapter 1

Cold Atmospheric Plasma for Bioaerosol Disinfection

This chapter provides a comprehensive overview of Cold Atmospheric Plasma (CAP) and its application in bioaerosol disinfection, establishing the foundation for the experimental approaches detailed in subsequent chapters. The chapter is structured into two primary sections, beginning with the basics of bioaerosol disinfection and leading into the specifics of low-temperature plasma technologies. This structure aims to present the fundamental principles of CAP and its potential as a disinfection method, as well as the variety of devices utilized to generate non-thermal plasma for microbial inactivation.

Section 1.1 introduces bioaerosols, their significance in public health, and the need for effective disinfection technologies. This section also covers the types of microorganisms present in bioaerosols, such as bacteria, viruses, and fungi, which are potential vectors for infectious diseases. The concept of sterilization and disinfection is then explored to contextualize the role of CAP as an innovative solution for bioaerosol inactivation.

Section 1.2 delves into the concept of Low-Temperature Plasma (LTP), with a focus on the mechanisms that enable CAP to function effectively at room temperature, making it suitable for bioaerosol disinfection. This section begins by categorizing the different types of low-temperature plasma devices, detailing the unique characteristics and application areas of each configuration. Special attention is given to the Dielectric Barrier Discharge (DBD device, a CAP source known for its efficiency in generating reactive species under atmospheric pressure without significant heat, allowing it to be applied safely on sensitive materials.

Finally, Section 1.3 discusses CAP's specific role in bacterial inactivation, highlighting the interaction of reactive oxygen and nitrogen species (RONS) with microbial structures.

This section sets the stage for the experimental focus of this research, emphasizing CAP's potential in reducing bioaerosol-borne pathogens and presenting the primary principles and parameters that influence its antimicrobial efficacy. The insights provided here will inform the design choices and parameters described in Chapter 2, where the experimental setup is discussed in detail.

1.1 Bioaerosol Disinfection

In this section, the fundamentals of bioaerosol disinfection are introduced, including an overview of bioaerosols, the critical importance of their disinfection, and the main existing technologies for achieving this goal. Among these technologies, plasma-based disinfection is briefly introduced and it will be thoroughly presented in the following section.

1.1.1 Introduction to Microorganisms

Bioaerosols are airborne particles that contain or are associated with biological material. These particles are a complex mixture that includes bacteria, viruses, fungal spores, pollen, endotoxins, mycotoxins, and fragments of plants or animals. The size of bioaerosols can vary significantly, ranging from less than one micron to over 100 microns in diameter (Figure 1.1). Due to their diverse composition, bioaerosols are ubiquitous in various environments, including outdoor settings such as forests, agricultural fields, and urban areas, as well as indoor environments like homes, hospitals, and workplaces. The presence and concentration of bioaerosols in a given environment are influenced by multiple factors, including geographic location, weather conditions, and human activities [28].

In the context of sterilization, microorganisms are the primary targets because the goal of sterilization is to eliminate all forms of microbial life to prevent contamination and ensure safety in environments such as healthcare settings, laboratories, and food production facilities. Understanding the various types of microorganisms, their structures, and their resilience to different sterilization techniques is essential for developing effective decontamination methods.

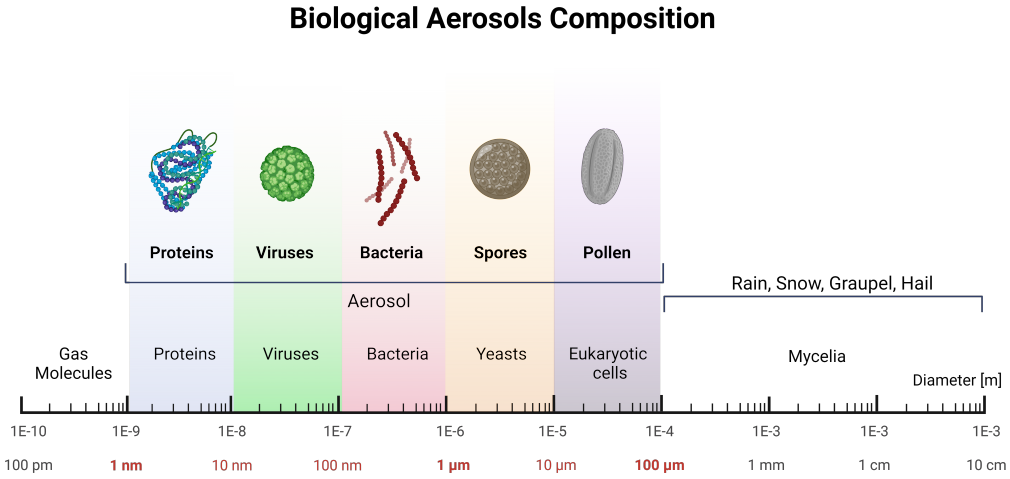

Figure 1.1 – Biological aerosol composition. Characteristic size ranges of atmospheric particles and bioaerosols (adapted from [29]).

Viruses

Viruses are acellular entities that consist of genetic material (DNA or RNA) enclosed within a protein coat called a capsid. Some viruses also possess an outer lipid envelope derived from the host cell membrane. Unlike other microorganisms, viruses lack independent metabolism and can only replicate by infecting a host cell, making them unique in the microbial world and posing specific challenges for sterilization.

Viruses can be classified based on the presence or absence of an envelope. Enveloped viruses, such as influenza and HIV, have a lipid membrane that makes them more susceptible to disinfectants. Non-enveloped viruses, like norovirus and poliovirus, lack this lipid layer and are generally more resistant to harsh conditions, including some chemical disinfectants, requiring more rigorous sterilization methods.

- *Influenza*: An enveloped virus responsible for respiratory infections. Its lipid envelope makes it vulnerable to many disinfectants, which is advantageous for sterilization efforts.
- *HIV*: Another enveloped virus that causes AIDS. Its susceptibility to disinfectants is due to its fragile envelope, requiring specific sterilization in healthcare settings.

- *Norovirus*: A non-enveloped virus that causes gastroenteritis. Known for its resilience, norovirus is resistant to alcohol-based sanitizers, necessitating alternative disinfection methods.
- *Poliovirus*: A non-enveloped virus associated with polio. Its robust structure makes it resistant to many disinfectants, presenting challenges in achieving complete inactivation.

Bacteria

Bacteria are unicellular organisms capable of thriving in diverse environments. Characterized by their simple structure without a true nucleus, bacteria are classified by shape, oxygen requirement, and, crucially, cell wall composition, which can be identified using the Gram staining technique.

Bacteria are commonly used in sterilization studies due to their ease of cultivation and range of resistance levels. This diversity makes them suitable model organisms for evaluating sterilization methods.

- *Staphylococcus aureus*: A Gram-positive bacterium commonly found on human skin and in nasal passages. It is a major cause of healthcare-associated infections (HAIs) and is notable for its resistance to multiple antibiotics, including methicillin (MRSA).
- *Bacillus subtilis*: A spore-forming, Gram-positive bacterium. Its spores are highly resistant to heat, desiccation, and disinfectants, making it a model organism for testing the limits of sterilization processes, especially autoclaving.
- *Escherichia coli* (E. coli): A Gram-negative bacterium commonly found in the intestines. While most strains are harmless, pathogenic strains can cause severe illness. It serves as a model organism due to its well-characterized genome and ease of cultivation.
- *Pseudomonas aeruginosa*: A Gram-negative bacterium known for its antibiotic resistance and biofilm formation, making it a challenging target for sterilization. It is a significant cause of infections in immunocompromised individuals.

Fungi

Fungi are eukaryotic organisms that include yeasts and molds. Unlike bacteria, they have a more complex cellular structure, including a nucleus and organelles. Fungal spores, which are produced asexually, are highly resistant to environmental stressors, making them challenging targets for sterilization processes.

Fungi are relevant in bioaerosol studies as their spores can remain airborne for extended periods, posing risks for infections and allergies.

- *Aspergillus niger*: A mold known for its production of highly resistant black spores. It is commonly used as a standard test organism in sterilization studies due to its resilience against heat and chemical disinfectants.
- *Candida albicans*: A yeast commonly found in human microbiota, which can cause infections in immunocompromised individuals. Its biofilm-forming ability on medical devices poses significant challenges for sterilization in healthcare settings.
- *Penicillium notatum*: Known for its historical role in the discovery of penicillin, this mold is also used in studies for its resilience and widespread presence in indoor environments.

For practical and safety reasons, highly pathogenic microorganisms are often replaced with non-pathogenic surrogates that exhibit similar resistance traits. These surrogates are chosen based on structural and biochemical characteristics that mimic those of the target pathogens, allowing for safer experimentation without compromising data validity. Non-pathogenic strains of *Escherichia coli* serve as models for more pathogenic Gram-negative bacteria, allowing standardized testing of various disinfection methods without the risks associated with highly virulent strains.

1.1.2 Sterilization and Disinfection

Sterilization refers to the complete elimination of all forms of microbial life, including bacteria, viruses, fungi, and spores, from surfaces or environments. It is a critical process in medical, laboratory, and pharmaceutical settings where absolute sterility is required to prevent contamination and ensure safety. However, achieving, proving, and maintaining complete sterilization in real-world scenarios can be challenging due to the complexity of environments and the limitations of current technologies.

While surface sterilization is well-defined and standardized, particularly by organizations like the World Health Organization (WHO), air sterilization lacks universally

recognized standards. Current guidelines emphasize ventilation, filtration, and monitoring rather than achieving complete sterility. The continued development of new technologies, including CAP, holds promise for advancing both air and surface sterilization practices. However, comprehensive regulations and standards for air quality and microbial control in enclosed spaces are needed to ensure public safety and health.

WHO defines sterilization for surfaces as achieving a Sterility Assurance Level (SAL) of 10^{-6}, described as a one-in-a-million probability that a viable microorganism remains following the sterilization process. In practical terms, this value is frequently associated (by international standards ISO 11135, 11137, 17665, EN 556, ANSI/AAMI ST67, ecc.) with achieving a "6-Log" reduction in microbial load through the *overkill* approach, although strictly speaking, SAL is a probabilistic concept rather than an exact mathematical equivalent of 6-log reduction. This high inactivation level is typically achieved through established methods such as autoclaving or chemical sterilization, and it is a benchmark for declaring an environment or surface as sterile [30].

In contrast, no universally standardized SAL exists for air sterilization. Guidance documents from the WHO and other regulatory bodies emphasize air decontamination rather than full sterilization, particularly because it is exceptionally challenging to maintain a SAL of 10^{-6} in continuously changing, open-air environments. Consequently, a formal SAL target—comparable to that used for surfaces—has not been adopted for air, reflecting the inherent complexity and dynamic nature of airborne microbial control.

Several guidelines and recommendations have been developed to ensure air quality and minimize the transmission of pathogens [31]:

- **Ventilation**: Increased ventilation is recommended to ensure a steady flow of fresh air and the dilution of airborne contaminants. Systems should ideally provide a complete air change every 20-30 minutes in crowded spaces.
- **Filtration**: The use of High-Efficiency Particulate Air (HEPA) filters is advised for HVAC systems, particularly in critical environments like hospitals, where they can capture up to 99.97% of particles as small as 0.3 microns.
- **CO_2 Monitoring**: CO_2 levels are used as a proxy for air quality, with recommended thresholds below 800-1000 ppm, indicating effective ventilation and lower risks of airborne transmission.
- **Microbial Limits**: While there are no standardized microbial limits for general public spaces, a count of fewer than 500 CFU/m^3 is generally considered safe in non-critical environments. For critical areas such as operating rooms, much stricter

limits apply, often below 10 CFU/m³, though these are based on guidelines rather than hard regulations.

Overview of Sterilization Methods

Sterilization methods vary depending on the application, with each method offering specific advantages and limitations. Below is a summary of the main methods currently used for sterilization in various settings:

Autoclaves

Autoclaves are widely used in hospitals, laboratories, and research facilities to sterilize instruments, utensils, and waste materials. They operate by using pressurized steam at around 121°C to inactivate microorganisms. The minimum duration required for sterilization is typically 20 minutes, excluding the time required for temperature buildup and subsequent drying. While highly effective, autoclaving is not suitable for all materials, particularly those sensitive to heat and moisture. Additionally, autoclaves consume significant amounts of energy and water, contributing to environmental concerns. Autoclaves are included in the list for sake of completeness, but they cannot be used for bioaerosol disinfection.

Chemical Sterilization

Chemical sterilization is often used for thermo-sensitive materials that cannot withstand the high temperatures of autoclaving. Common chemicals used include ethylene oxide (EtO) and formaldehyde. These gases are effective in inactivating microorganisms but pose significant risks to human health due to their toxicity. Ethylene oxide, for example, is a toxic gas that targets cellular proteins and nucleic acids, while formaldehyde is a known carcinogen. The use of chemical sterilants requires careful handling and appropriate safety measures to prevent harmful exposure.

Radiation Sterilization

Radiation sterilization, particularly with gamma rays from Cobalt-60, is a highly effective method for sterilizing medical products, including needles and tissue grafts. Gamma radiation causes significant damage to the DNA or RNA of microorganisms, leading to their inactivation. This method is ideal for sterilizing large batches of products but requires strict safety protocols due to the handling of radioactive materials.

Ozone Sterilization: Ozone is an emerging sterilization technique that creates a highly oxidizing environment capable of inactivating a wide range of microorganisms, including highly resistant spores like *Geobacillus stearothermophilus*. While promising,

ozone sterilization requires longer exposure times to achieve effectiveness and must be carefully controlled to prevent potential health hazards due to ozone's reactive nature.

Hydrogen Peroxide Sterilization: Hydrogen peroxide (H_2O_2) is widely used in gas plasma sterilizers, where it is ionized to enhance its sterilizing properties. While effective, the term "plasma sterilizer" is sometimes misleading, as the sterilization effect is primarily due to the chemical action of H_2O_2 rather than the plasma itself. H_2O_2 sterilization is suitable for sensitive materials and is commonly used in hospital settings.

Low-Temperature Plasma (LTP) Sterilization: Low-Temperature Plasma (LTP) sterilization is a newer technology that offers several advantages over traditional methods. LTP systems use ionized gases at low temperatures to generate reactive species that inactivate microorganisms. This method is particularly beneficial for sterilizing heat-sensitive and water-sensitive materials. Compared to autoclaving, LTP sterilization is more energy-efficient, requires shorter treatment times, and does not produce hazardous residues (if kept under guidelines limit). LTP is being developed as a promising alternative for sterilization in various industries, although more research is needed to fully commercialize this technology. When the system operates at atmospheric pressure it is referred to as Cold Atmospheric Plasma (CAP).

1.2 Low-Temperature Plasma

Introduction to Plasma

Plasma, often referred to as the fourth state of matter, is a gas that is partially or fully ionized, composed of free electrons, ions, and neutral atoms or molecules. This state is characterized by collective behaviors resulting from long-range electromagnetic interactions between the charged particles. Irving Langmuir first systematically defined plasma in the 1920s.

Plasmas are ubiquitous in the universe, constituting approximately 99.9% of the observable matter, predominantly found in stars, nebulae, and the interstellar medium. On Earth, plasmas are naturally observed in phenomena such as auroras, lightning, and even fire. Plasmas can be broadly classified into two categories based on their thermal characteristics: thermal plasmas and non-thermal plasmas.

Thermal plasmas, also known as equilibrium plasmas, are characterized by the presence of thermal equilibrium among all species within the plasma. This means that the temperatures of electrons, ions, and neutrals are equal. These are known as Local Thermodynamic Equilibrium (LTE) plasmas, where collisions among particles are

frequent enough to establish a common temperature across the species. These plasmas are typically found in high-energy environments, such as the core of stars or fusion reactors, where temperatures can range from 10^4 K in arc discharges to 10^8 K in fusion processes [32].

In contrast, *non-thermal plasmas*, or non-equilibrium plasmas, exhibit significant differences in temperature between the species. In these plasmas, electrons tend to have much higher temperatures than ions and neutrals. Here, electrons are much more energetic than ions and neutrals, creating a non-equilibrium or Partial Local Thermodynamic Equilibrium (PLTE) condition. This discrepancy arises because the collision rate is not high enough to allow full thermal equilibration among particles. Such non-equilibrium conditions enable the generation of highly reactive species at relatively low gas temperatures, making non-thermal plasmas suitable for applications where heat-sensitive materials are involved, such as biomedical and environmental disinfection.

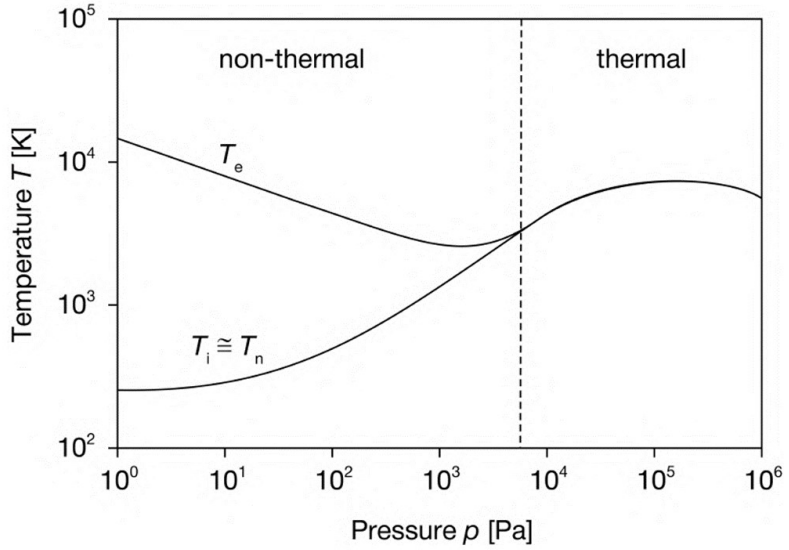

Figure 1.2 – Evolution of the plasma temperature with the pressure in a mercury plasma arc. T_e, T_i and T_n represent the temperature of the electrons, ions, and neutrals, respectively [32]

As shown in Figure 1.2, non-thermal plasmas are typically generated at low pressures (below 10^4 Pa) because collision frequency depends on gas density, which increases with pressure. At higher pressures, collisions become more frequent, promoting both chemical reactions through inelastic collisions and heating of heavier particles (neutrals T_n and ions T_i) via elastic collisions. This results in a reduced temperature difference between T_e (electron temperature) and T_h (temperature of heavy particles), bringing the plasma closer to thermal equilibrium. However, non-thermal plasma can also be generated at atmospheric pressure, where input power plays a key role. Generally, high

power yields thermal plasmas, like arc plasmas, while non-thermal plasmas are more likely to form with lower or pulsed power sources.

Low-pressure plasmas, often operated in vacuum chambers, are another important category used in industrial processes, including surface treatment, etching, and thin-film deposition. At low pressures, the mean free path of particles increases, leading to unique plasma characteristics that differ from atmospheric plasmas. The regime in which these low-pressure plasmas operate is often referred to as the Townsend regime. In this regime, ionization occurs primarily through electron impacts rather than through thermal excitation, leading to a controlled, low-temperature plasma that can sustain a discharge even at minimal applied electric fields. This regime is named after John Sealy Townsend, whose work laid the foundation for understanding ionization mechanisms in gases.

In practical terms, plasmas in the Townsend regime are highly valued in applications requiring precise control over ion energy and density, such as semiconductor manufacturing and surface modification. The ability to operate at low pressures and control the plasma characteristics offers flexibility in adjusting parameters to achieve desired chemical reactions without excessive thermal input. This property makes low-pressure, non-thermal plasmas particularly effective in processes where material integrity must be preserved, as well as in emerging fields like bioaerosol disinfection, where low-energy, highly reactive species are needed to neutralize pathogens without damaging surrounding materials or environments, thus maintaining the temperature around room temperature.

Plasma Characteristics

One of the fundamental properties of plasma is the *plasma frequency*, which represents the natural frequency of oscillations of the electron component relative to the ions. This frequency is given by:

$$\omega_p = \sqrt{\frac{n_e e^2}{\epsilon_0 m_e}}$$

where n_e is the electron density, e is the electron charge, ϵ_0 is the permittivity of free space, and m_e is the electron mass. The plasma frequency is crucial for determining the plasma's response to electromagnetic fields and is a key parameter in distinguishing between different plasma regimes.

Another critical characteristic is the Debye length, λ_D, which is the scale over which electric potentials are screened out in the plasma. It is defined as:

$$\lambda_D = \sqrt{\frac{\epsilon_0 k_B T_e}{n_e e^2}}$$

where k_B is the Boltzmann constant and T_e is the electron temperature. The Debye length dictates the spatial extent over which the plasma can be considered quasi-neutral, meaning that charge imbalances are negligible over distances larger than λ_D.

The temperature of plasma species is a fundamental parameter that influences the plasma's behavior and applications. Electron temperature (T_e) typically governs the rates of excitation and ionization processes, while ion temperature (T_i) and neutral temperature (T_n) affect the momentum transfer and energy exchange within the plasma. Plasma densities, including electron density (n_e) and ion density (n_i), determine the plasma's ability to conduct current and sustain electromagnetic waves.

Low-Pressure Plasma Discharges

In low-pressure environments, plasma discharges exhibit distinct characteristics, which can be described through various regimes such as the *Townsend discharge* and the *glow discharge*. The Townsend discharge occurs at very low pressures and voltages, where ionization is initiated by free electrons that gain energy from the electric field and subsequently ionize neutral gas atoms through collisions. The process is self-sustaining as secondary electrons are emitted from the cathode due to ion impacts, leading to further ionization. The Townsend regime, characterized by low current and high resistance, is the initial stage of a plasma discharge. As the current increases, the plasma transitions to different modes, including the α-mode, where ionization is driven primarily by electron impact, and the γ-mode, where secondary electron emission from the cathode plays a significant role [32]. At higher voltages and pressures, the plasma transitions into a glow discharge, characterized by distinct regions such as the cathode fall, negative glow, and positive column. The glow discharge is marked by its visible light emission and is used in various applications, including neon signs and plasma displays.

The *breakdown voltage* is the minimum voltage required to initiate a self-sustaining plasma discharge in a gas. Paschen's law describes the relationship between breakdown voltage, gas pressure, and electrode gap distance:

$$V_b = \frac{B \cdot p \cdot d}{\ln(A \cdot p \cdot d) - \ln(\ln(1 + 1/\gamma))} \tag{1.1}$$

where A and B are constants dependent on the gas type, p is the pressure, d is the gap distance, and γ is the secondary Townsend coefficient. This relationship is crucial for designing plasma devices, especially in applications where low-pressure discharges are employed.

1.2.1 Types of Low-Temperature Plasma Devices

There are various types of low-temperature plasma configurations and devices, each with distinct characteristics and applications. Among these, Dielectric Barrier Discharge (DBD plasmas are particularly noteworthy for their versatility in applications such as surface treatment, sterilization, and ozone generation. The main types of low-temperature plasma devices are summarized in Table 1.1.

Table 1.1 – Types of Low-Temperature Plasma (LTP) devices and their applications [32].

Type of LTP Device	**Description**
Capacitively Coupled Plasma (**CCP**)	CCP devices generate plasma between two parallel electrodes using a high-frequency alternating current. CCPs are widely used in semiconductor manufacturing for processes such as etching and deposition due to their ability to produce a uniform plasma over a large area.
Inductively Coupled Plasma (**ICP**)	ICP devices utilize a radio-frequency electromagnetic field to ionize the gas, creating a high-density plasma. ICPs are particularly valuable in analytical chemistry for techniques such as mass spectrometry and optical emission spectroscopy, where high plasma density is essential for accurate measurements.
Dielectric Barrier Discharge (**DBD**)	DBD devices generate plasma using two electrodes separated by a dielectric material, which prevents the formation of a continuous arc. DBDs are used in various applications, including ozone generation, surface treatment, and sterilization.

Continued on next page

Type of LTP Device	Description
Atmospheric Pressure Plasma Jets (**APPJs**)	APPJs produce plasma at atmospheric pressure in the form of a jet, making them ideal for surface modification, biomedical treatments, and environmental applications. These devices operate at low temperatures, allowing for the treatment of heat-sensitive materials.
Corona Discharge	Corona discharge devices generate plasma in a high electric field region near a pointed electrode, causing ionization of the surrounding gas without creating a complete arc. They are commonly used for pollutant abatement, air purification, and surface treatment to enhance material adhesion.

Understanding the fundamental properties and behaviors of plasmas is essential for harnessing their potential in various technological applications. Low-temperature plasmas, with their unique non-equilibrium characteristics, offer a versatile tool for industries ranging from materials processing to biomedicine. The ability to control plasma parameters such as temperature, density, and discharge mode through the design of specific devices like CCP, ICP, and DBDs underscores the importance of continued research and development in this field.

1.2.2 Dielectric Barrier Discharge

Dielectric Barrier Discharge (DBD) plasma systems present diverse configurations, each suited for specific applications. A common setup, as depicted in 1.3 (A), consists of two electrodes separated by a dielectric barrier, with a working gas introduced in the gap. When a high electric field is applied, plasma forms in this region, characterizing a volume-DBD (VDBD) plasma. In VDBD systems, the sample is typically placed within the discharge region. In the configuration shown in 1.3 (B), the dielectric is between the electrodes, creating plasma on both sides of the dielectric, which is advantageous for thin-film processing applications [33].

An alternative is the cylindrical DBD plasma configuration (1.3 (C)), where a cylindrical dielectric houses electrodes inside and outside, generating plasma within the cylinder. This setup allows for the production of gas-phase products at the outlet instead of direct plasma exposure, making it effective for gas-phase catalysis [34]. Solid catalysts can be loaded within the cylinder to improve catalytic reactions, though the restricted discharge space limits the device's use for larger samples [35].

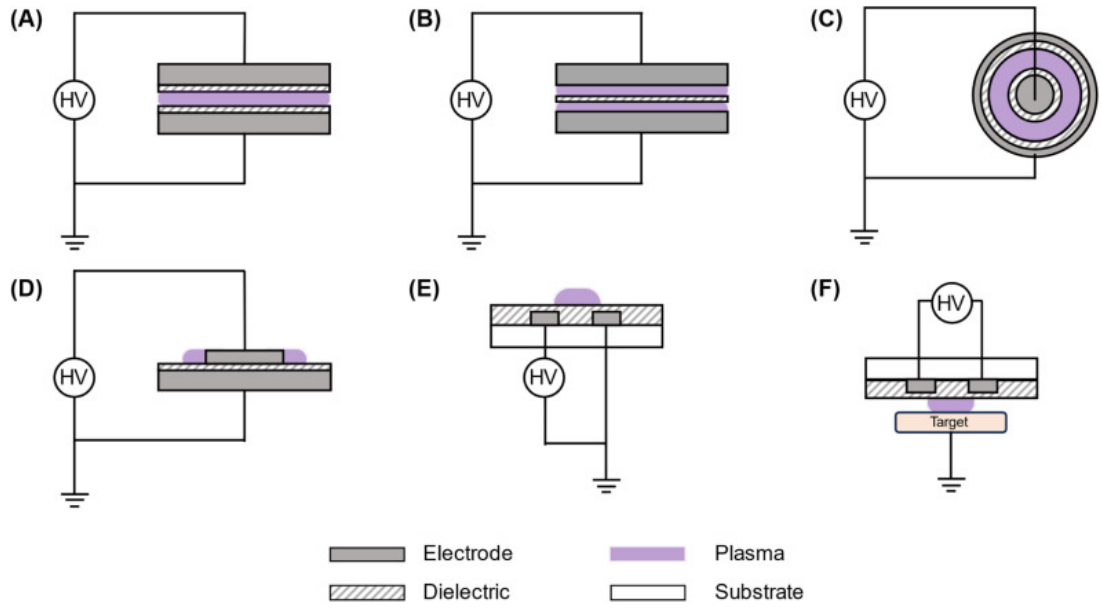

Figure 1.3 – Types of DBD plasma system: (A), (B) Volume DBD plasma. (C) Cylindrical volume DBD plasma. (D), (E) Surface DBD plasma. (F) Floating DBD plasma. Source: [36]

To address the spatial limitations of VDBD systems, surface DBD (SDBD) devices were developed (1.3 (D)). Initially designed for flow control in aeronautics, due to their ability to produce ionic wind [37], SDBD devices are now used in broader applications, including surface disinfection and wound healing. This setup embeds one or both electrodes within the dielectric, allowing for a large discharge area on the surface and overcoming dimensional restrictions, as shown in 1.3 (E [38].

Floating-electrode DBD (FE-DBD) plasma devices add further flexibility. In these setups, only one electrode is embedded in the dielectric, while the other "floating electrode" is the sample itself (1.3 (F)). Plasma is generated due to the potential difference between the high-voltage electrode and the floating sample, making FE-DBD devices suitable for sensitive biological applications, such as wound treatment and disinfection [39].

1.3 CAP for Bacterial Inactivation

Cold Atmospheric Plasma (CAP) sterilization leverages a variety of bioactive agents that, in combination, produce significant antimicrobial effects. These agents include neutral particles, reactive species, charged particles, UV radiation, and electromagnetic fields, each contributing uniquely to the plasma's sterilization efficacy. A summary is provided in Figure 1.4. Studies have shown that cold plasma devices are effective in reducing airborne bacteria, viruses, and fungal spores [12]. Below is a detailed summary of the main plasma components used in sterilization.

- **Neutral Particles**
  - **Metastables and Atoms**: Metastable atoms and molecules, such as Ar*, He*, N, and O, possess high energy that can transfer to other molecules, facilitating chemical reactions. These species are primarily identified through emission and absorption spectroscopy.
  - **Effect**: Metastable particles assist in the excitation and ionization of reactive species, initiating processes that disrupt microbial structures.
- **Electromagnetic Fields**
  - **Static and Amplified Electric Fields**: CAP devices generate static electric fields or localized field amplification that can penetrate microbial cells, disrupting cellular functions.
  - **Effect**: These fields are detected through spectroscopic measurements and Pockels effect-based methods, contributing to the direct disruption of microbial cell integrity.
- **Heat Transfer**
  - **Temperature of Neutrals, Ions, and Electrons**: While CAP is generally a non-thermal plasma, localized heating of neutral particles, ions, and electrons can occur, potentially affecting microbial viability.
  - **Effect**: The temperature of gas species is often measured by Boltzmann plots, ensuring that the thermal impact remains within safe limits for biological applications.
- **Radiation (UV/VIS/IR)**
  - **UV Emission**: CAP produces UV radiation, spanning from UV-A to UV-C, capable of causing direct DNA damage in microbes, leading to mutagenic and cytotoxic effects.
  - **Effect**: Spectroscopic measurements assess the emission of excited species from UV to infrared, targeting microbial DNA and cellular components.
- **Reactive Species**
  - **Reactive Oxygen and Nitrogen Species (RONS)**: Reactive species such as hydroxyl radicals (OH), ozone (O_3), and nitric oxide (NO) play a central role in plasma's antimicrobial action.

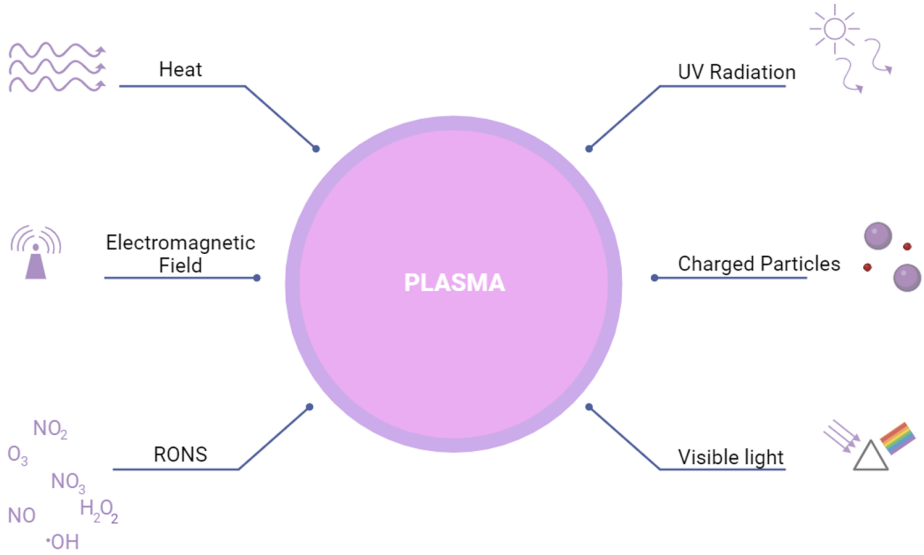

Figure 1.4 – Representation of the complex components of non-thermal plasma treatment.

  - **Effect**: Visualized through Laser-Induced Fluorescence (LIF) and absorption measurement methods, these species disrupt cell walls and interfere with microbial metabolism and DNA.

- **Charged Particles**
  - **Electrons and Ions (Ar^+, N_2^+, O^-)**: Charged particles in CAP play a crucial role in maintaining plasma conditions and interacting with microbial surfaces.
  - **Effect**: Charged particles are measured by mass spectrometry, modeling, and spectroscopic techniques. They facilitate electron collisions that lead to the excitation and ionization of other species, enhancing the overall antimicrobial efficacy.

Chapter 2

Complete Description of the Experimental Setup: from Bioaerosol Generation to Sampling through Plasma Treatment

This chapter outlines the experimental approach used to develop and characterize a setup for a bioaerosol plasma treatment and sampling in order to ensure accurate and reliable results. The chapter is divided into three main sections, detailing bioaerosol generation, treatment, and sampling. Each section provides a detailed description of the experimental setup and procedures, as summarized in Figure 2.1, forming the basis for the results presented in Chapter 3, which covers the electrical, chemical, and biological characterization. The entire generation and sampling setup was funded by the Swiss Plasma Center (SPC) at EPFL in Lausanne and utilized in the Bio-plasma laboratory at SPC.

Section 2.1 begins with a discussion on the nebulization process, a critical step for generating bioaerosols in controlled experimental conditions. This section introduces the principles of nebulization and explains the selection of the BLAM (Blaustein Atomizing Modules) produced by CH Technologies.

Section 2.2 describes the methods used for sampling the generated bioaerosols, which is crucial for subsequent microbial viability and concentration analysis. The section begins with a brief overview of various bioaerosol sampling techniques and then focuses on the selected SKC BioSampler ®, a liquid impinger known for its efficiency in collecting viable microorganisms from air samples. Details on the preparation of *Escherichia coli*

solutions and the CFU counting method, including specific dilution steps for quantifying viable cells, are also provided.

Finally, Section 2.3 delves into the novel custom atmospheric pressure Dielectric Barrier Discharge (DBD) reactor, named **GAPS - Grid-like Air Plasma Sanitizer**, for plasma treatment of *E. coli* bioaerosol. This section covers the design of GAPS and its power supply configuration. The reactor's electrical and chemical characterization methods will be presented and explained. The results obtained in the explained configuration are presented in the final Chapter 3.

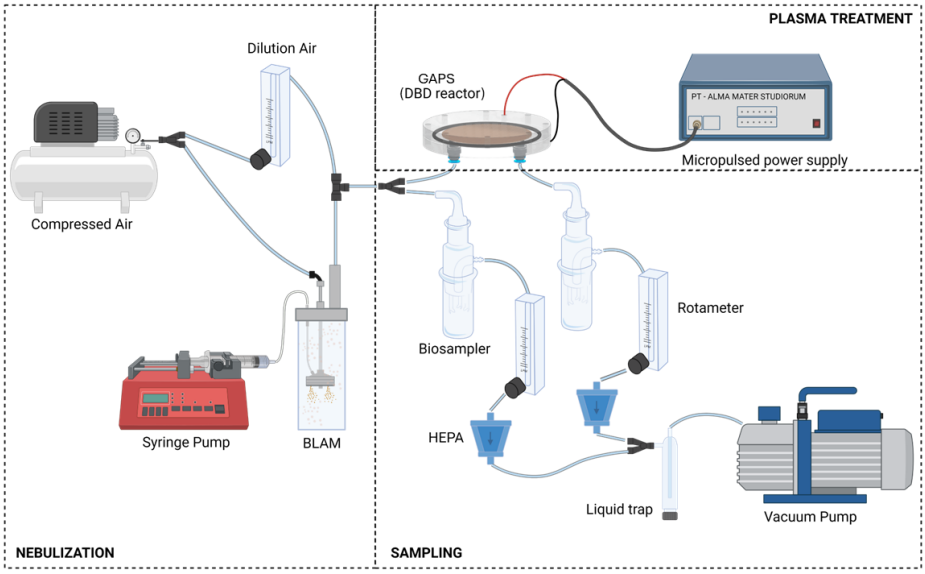

Figure 2.1 – Bioaerosol generation, treatment, and sampling set-up. From the syringe pump contaminated liquid, through the DBD reactor (GAPS) for the plasma treatment, to the sampling impinger before and after the treatment.

2.1 Bioaerosol Generation

Nebulization plays a pivotal role in the generation of bioaerosols for experimental applications, as it affects both the physical characteristics and the biological integrity of the aerosolized particles. This section briefly explores the principles behind nebulization, providing an overview of commonly used technologies and their relevance to bioaerosol studies. The Blaustein Atomizing Module (BLAM) by CH Technologies was selected for this study based on its demonstrated ability to reduce mechanical and thermal stress during nebulization, leading to improved particle viability and greater efficiency in both nebulization and subsequent sampling processes. Details on the specific configuration

of the BLAM system utilized in the experiments, including operational parameters such as flow rates, are explained. These parameters were optimized to ensure the consistent generation of bioaerosols for the subsequent treatment and analysis stages, laying the groundwork for reliable experimental outcomes.

What is Nebulization

Nebulization is the process of breaking down a liquid into small droplets or particles that can be dispersed into the air as aerosols. This process is essential in various fields, including research, industry, and medicine, where it is used to generate aerosols of liquids for drug delivery, bioaerosol creation, and other specific applications. In the context of bioaerosol generation, nebulization plays a critical role as it allows the creation of particles containing microorganisms, cells, or other biological materials.

The basic principle of nebulization involves applying mechanical energy to a liquid to overcome surface tension, thereby fragmenting it into small droplets. The type of energy applied varies depending on the device used, which may employ shear forces, impacts, or other fragmentation techniques to generate the desired particles. The properties of the liquid, such as viscosity, density, and surface tension, influence the fragmentation process and, consequently, the size and distribution of the generated particles.

- *Natural bioaerosols* are airborne biological particles that can be transported thousands of kilometers before settling [40]. These particles play a vital role in the global distribution of biological material and can originate from a variety of natural sources. Broadly, natural sources of bioaerosols can be divided into two categories: dry bioaerosols (particles) and liquid bioaerosols (droplets).
- *Dry bioaerosols* are typically generated by mechanical processes, such as dust storms or wind lifting biological material from surfaces like soil or vegetation. (Examples include fungal spores, pollen, and fragments of organic matter lifted by the wind. Humans and other organisms can also contribute to the generation of dry bioaerosols through the emission of skin cells or biological fragments during movement.)
- *Liquid bioaerosols* are produced by the fragmentation of natural liquids, such as water from oceans and lakes. (For example, bubbles forming and bursting on water surfaces release droplets containing microorganisms, salts, and other organic substances. Other examples include droplets generated by raindrops that impact biological surfaces and can carry biological material such as bacteria and viruses.)

- *Experimental bioaerosols* are generated in the laboratory to replicate natural processes in a controlled environment. This is essential for studying phenomena such as the viability and transformation of microorganisms in the atmosphere, as well as evaluating the efficiency of bioaerosol collection devices or protective technologies against microbiological risks. (Although bioaerosol concentrations in laboratories are often higher than those found in nature, this facilitates detection and data analysis.)

Escherichia coli was chosen as the test bacterium for the assessment of plasma treatment efficacy for several reasons, as outlined in 1.1.1. Most notably, *E. coli* is extensively used in bioaerosol research, and a large body of literature exists regarding its behavior in various experimental setups. This wealth of information allows for the optimization of bioaerosol generation and sampling systems specifically tuned for *E. coli*. In particular, numerous studies have compared the efficiency of nebulization and bacterial viability using different nebulizers, with *E. coli* emerging as the reference organism due to its frequent use in such experiments.

Comparison of Different Nebulizers

There are various devices for experimental bioaerosol generation, each with specific advantages and limitations and vary depending on the type of bacteria used. These methods are often adapted from techniques used for non-biological materials, which can affect optimization for bioaerosol studies. Table 2.1 provides a detailed summary of the main experimental devices, describing the working principles, advantages, and disadvantages of each method [41].

A key challenge for nebulization devices is delivering high concentrations of viable bacteria while minimizing cell damage. Figure 2.2 illustrates the three devices compared in experiments done by Zehn et al. [42] using *E. coli* as the bacteria to be tested. In these tests, bacterial suspensions were aerosolized, and each nebulizer's efficiency was determined by comparing the number of culturable bacteria collected in the impinger to the total bacteria introduced into the nebulizer. The study focuses on three common systems: the Collison nebulizer, Blaustein Atomizing Modules (BLAM), and Sparging Liquid Aerosol Generator (SLAG), assessing their performance in terms of viable bacterial concentration and nebulization efficiency. Below are the specifics of the generator used:

- **Collison Nebulizer:** The Collison nebulizer is widely used in bio-aerosol research due to its ability to produce high concentrations of aerosols. However, it has drawbacks related to microorganism viability, as the strong impaction and shear

Table 2.1 – Main methods for experimental bioaerosol generation (adapted from [41])

Method	Working Principle	Advantages	Disadvantages
Collison Nebulizer	Fluid shearing	High reproducibility and high aerosol output	Damage to biological material due to recirculation
Bubble Generator	Bubble bursting in liquids	Faithful replication of natural processes	Produces low aerosol concentrations
Ultrasonic Nebulizer	High-frequency vibrations	Better control over droplet size distribution	Requires larger liquid volumes
Centrifugal Atomizer	Rotation of a disk or nozzle	Produces uniform particle size distribution	Sensitive to fluid properties

forces generated during atomization can cause damage to cells. The device works by recirculating the liquid through an air jet, where the liquid is repeatedly sheared, creating droplets. The larger droplets impact against the walls of the jar and are recirculated, while smaller droplets are aerosolized [43]. This repetitive process increases the stress on biological particles and can lead to fragmentation and viability loss. Despite this, the Collison nebulizer remains a popular choice due to its high output.

- **Blaustein Atomizing Modules (BLAM):** The BLAM nebulizer uses a single-pass atomization mechanism, which minimizes cell damage by exposing the bacteria to the air jet only once. The atomizer consists of a nozzle and expansion plate that together create a vacuum effect. When pressurized air passes through the nozzle at sonic velocity, it breaks the liquid into droplets. Larger droplets are retained within the expansion chamber, while smaller droplets are aerosolized [44]. The absence of recirculation makes the BLAM system more suited to experiments requiring higher bacterial viability, and the nebulization process can be tuned based on the properties of the liquid being aerosolized.

- **Sparging Liquid Aerosol Generator (SLAG):** The SLAG nebulizer works by generating aerosol particles through the bursting of bubbles within a liquid film. The process starts by pumping the liquid onto a porous disc where air is bubbled through the film, creating fine droplets that are carried out by an airflow [44]. This gentle bubbling mechanism is expected to reduce mechanical stress on microorganisms, making it an appropriate choice for aerosolizing delicate biological

materials. However, its aerosolization efficiency tends to be lower compared to pneumatic nebulizers like the Collison and BLAM systems.

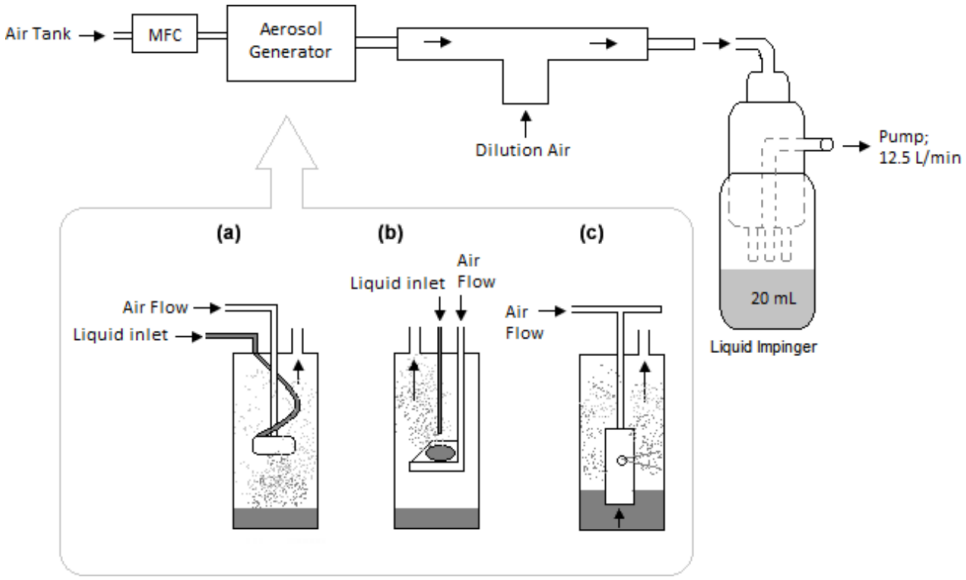

Figure 2.2 – . Experimental setup for the tests with the impinger. (a) BLAM, (b) SLAG, and (c) Collison. Source: [42].

Among the three nebulizers, the BLAM nebulizer demonstrated the highest efficiency, followed by the Collison nebulizer and SLAG [42]. This outcome is largely attributed to the BLAM's single-pass design, which minimizes mechanical stress on bacterial cells. The SLAG system, while offering gentler nebulization, showed lower output concentration due to the reduced aerosolization pressure. In particular, the BLAM showed a nebulization efficiency of approximately 1%, calculated as the number of CFU nebulized and collected in the impinger compared to the initial bacterial concentration in the liquid solution (this efficiency was determined at an airflow rate of 3.5 L/min).

Across all experiments, the viability of *E. coli* was significantly affected by the choice of nebulizer. The single-pass BLAM and SLAG systems preserved higher bacterial viability compared to the recirculating Collison nebulizer. This study underscores the importance of selecting an appropriate nebulizer based on the specific experimental goals, particularly when working with sensitive biological materials.

Given the selection of E. coli as the bacteria to be treated, another relevant study by Zhen et al. [45] is highlighted here, where it is shown that the Single Pass Atomization (SPA) nebulizer from CH Technology is the most effective at preserving the culturability of E. coli. This is attributed to the SPA's design, which prevents the recirculation of biological material, thus reducing mechanical stress and maintaining bacterial viability

during aerosolization. Given these considerations, the SPA mode of BLAM nebulizer was selected for the present work as it provides optimal conditions for generating and sampling bioaerosols of *E. coli* with minimal loss of viability.

In particular, the study by Zhen et al. [45] demonstrated that, compared to the Collison nebulizer, the SPA:

- Better *preserves bacterial viability*, such as *E. coli*, by reducing culturability loss.
- Maintains *greater cell membrane integrity*, as evidenced by the membrane damage index (ID), which was significantly lower than in the Collison nebulizer, especially at high aerosolization pressures.
- Is capable of producing *comparable bioaerosol concentrations* to those of the Collison nebulizer but with less biological damage.

For these reasons, the SPA has proven to be the most suitable bioaerosol generator for experiments requiring the preservation of bacterial integrity and viability, making it ideal for studies involving sensitive bacteria such as *E. coli*.

2.1.1 BLAM in SPA Mode

The following equipment is required for the bioaerosol generation protocol for BLAM, as suggested in [46]:

- Teflon tube for the connection between the compressed air source and the nebulizer (typically ¼" OD tube).
- Mass flow controller to manage the airflow.
- A syringe containing the bacterial solution to be sprayed.
- Silicon tube with Luer-lock connection to connect the syringe to the liquid inlet of the BLAM atomizer.
- A precision pump to feed the BLAM atomizer.
- Liquid impinger BioSampler® from SKC for sample collection.

For the experiment conducted in this research, we used a polyurethane (PU) tube for the connection, as no significant differences were reported compared to Teflon. Additionally, a rotameter followed by a pressure gauge was employed instead of a mass flow controller, as the high flow rates made it a more suitable choice.

The BLAM nebulizer requires a specific setup for proper operation in SPA mode, see Figure 2.3 and 2.4. The following procedure was followed to generate bioaerosols with *Escherichia coli* K-12 MG1655:

1. Use a ¼" OD tube to connect the compressed air line to the inlet of the BLAM. Use appropriate pressure and flow controllers to regulate the airflow. For this experiment, the air pressure was set to 2 bar, which produced an airflow of 8 LPM, using 8 Multi-Jet design at 1 LPM each.
2. Fill the jar with approximately 20–30 ml of test solution, ensuring not to exceed the maximum recommended volume. The solution serves as a soft impaction surface for the aerosol and is not used for atomization.
3. Connect the liquid feed port on the nozzle to the liquid feed bulkhead on the lid using a silicon tube. The bacterial solution (*E. coli* K-12 MG1655 was prepared with a concentration: 10^9 CFU/ml). A precision pump was used to deliver the solution at a flow rate of 0.28 ml/min.
4. When the bacterial solution reached the liquid feed port of the BLAM, the compressed air supply was activated to start the aerosol generation.
5. Using a mass flow controller, the airflow was set to 8 LPM. The injection of 2 ml of bacterial solution was completed in approximately 7 minutes.
6. To stop the aerosol generation, the air supply was turned off, followed by stopping the operation of the precision pump.

Figure 2.3 – View of the Complete Multi-Jet BLAM in SPA mode. Source: [47].

Sampling was performed at the output of the nebulizer, after the addition of the dilution air line, using a liquid impinger (BioSampler® from SKC). Further details can be found in Section 2.2.

For this experiment, the injection of 2 ml of bacterial solution resulted in bioaerosol deposition inside the chamber, as reported in [46]. The bacterial concentration in the nebulized solution was 10^9 CFU/ml, and the sampling confirmed the presence of viable *E. coli* in the liquid impinger after 7 minutes of aerosol generation. Results are shown in Chapter 3.

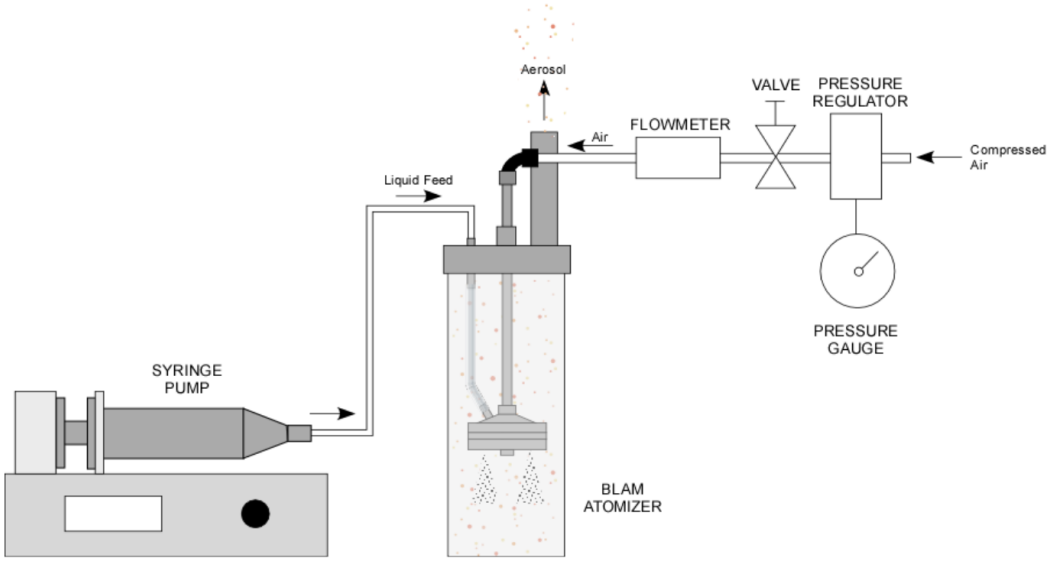

Figure 2.4 – Schematic of BLAM's Setup in SPA mode. Source: [47].

2.2 Bioaerosol Sampling

Bioaerosol sampling is a critical process in environmental and occupational health research, aiming to collect airborne biological particles, such as bacteria, fungi, viruses, and pollen, to evaluate their concentration, diversity, and potential health impacts. The primary goal of bioaerosol sampling is to obtain a representative sample from the air that can be preserved for further analysis using various microbiological and molecular techniques. Effective sampling requires balancing the integrity of the collected microorganisms and the efficiency of the sampler in capturing bioaerosols across a range of particle sizes.

Sampling directly impacts the accuracy and reliability of the microbial analysis performed on collected samples. This section provides an overview of the various bioaerosol sampling methods available and justifies the selection of the SKC BioSampler ®for this study. The efficiency of the sampling process is particularly important for ensuring the viability of microorganisms and for accurate quantification in subsequent analyses.

In sub-section 2.2.1, a review of existing bioaerosol sampling techniques is presented, highlighting the advantages and limitations of different systems in terms of viability preservation, sampling efficiency, and ease of use. Among the options, the liquid impinger method, specifically the SKC BioSampler ®, was selected due to its superior performance in capturing viable microorganisms from air samples. This method was chosen for its ability to efficiently collect viable particles with minimal mechanical stress, which is critical for accurate microbial viability analysis.

In sub-section 2.2.2 explains the colony-forming unit (CFU) counting method employed to quantify the concentration of viable microorganisms in the collected samples. This section details the preparation of samples, including the serial dilution steps required to obtain countable colonies on agar plates. The CFU counting method provides a robust and reproducible measure of microbial concentration in the sampled bioaerosols, forming the basis for assessing the efficacy of the plasma treatment.

Finally, sub-section 2.2.3 introduces the calculation method used to determine the log-reduction of microbial concentration following treatment. The log-reduction metric is used to quantify the extent of microorganism inactivation, with results calculated by comparing the initial microbial load with the post-treatment CFU counts. This metric is essential for evaluating the effectiveness of the plasma treatment and is a key parameter discussed in the subsequent results chapter.

2.2.1 Bioaerosol Sampling Consideration

The selection and use of a bioaerosol sampler can greatly influence study results. Factors such as bioaerosol type, particle size, concentration, environment, and analysis methods must be considered to ensure the collection of representative samples that meet study objectives. Some practical aspects to consider for effective bioaerosol sampling are outlined below, a more detailed discussion can be found in [48] [49].

1. **Selecting a Sampler** : selecting a bioaerosol sampler depends on variables like the bioaerosol type, expected particle size range, concentration, and the sampling environment. One must also consider the required analysis, biomass needs, sampling duration, and frequency. While it is possible to choose a sampler first and adjust study parameters, this may not always provide the best results. Ease of cleaning and disinfecting the sampler is critical to avoid cross-contamination between samples. Liquid-based samplers are preferable when multiple analytical techniques are needed, as filters may introduce particle losses during elution [49].

2. **Collection Medium**: the collection medium choice is as important as the sampler itself. Liquid-based samplers often require replenishment due to evaporation, particularly if the liquid level is not automatically maintained [50] [51]. Some studies use viscous fluids like mineral oil to reduce evaporation, though this complicates microorganism extraction [52]. Common collection fluids include deionized water, NaCl solution, or phosphate-buffered saline (PBS), sometimes with surfactants like Tween-20 or antifoaming agents [53] [54]. PBS is often preferred for its neutral pH, preserving bacterial viability, though some surfactants can increase cell membrane damage, reducing culturability [55].

3. **Physical Losses During Sampling**: physical losses in samplers can occur from particle bounce, re-aerosolization, or adherence to internal surfaces. In liquid-based samplers, these losses may exceed 50% if small amounts of collection fluid are used [56]. Washing the sampler's interior, along with vortexing or sonication, can help recover lost particles. To minimize bounce, viscous collection fluids like mineral oil can be used, though this complicates recovery.

4. **Filter Use**: filter-based samplers are advantageous for long sampling times and ease of use. However, extended sampling can desiccate bioaerosols, reducing culturability and structural integrity [57]. Gelatin filters and wetted porous foams can reduce desiccation but are also prone to drying out during long sampling periods [58] [59]. Gelatin filters can be dissolved in a buffer or placed directly on agar, simplifying analysis. One disadvantage of filters is the potential for sample loss during elution, especially in fibrous filters. However, optimized elution protocols can achieve particle recovery rates of 80% or higher [60].

5. **Sampling Duration and Frequency**: the duration and frequency of sampling should match study objectives, bioaerosol concentration, and sampler type. Personal sampling should match the activity duration, while environmental samples should capture representative concentrations over longer periods. For filters or agar impactors, careful consideration of sampling duration is necessary. For impactors, excessive sampling times can overload the collection surface, while insufficient times may not capture enough data. Some studies limit multi-nozzle impactor sampling to 5 minutes to avoid overloading [61]. Desiccation of agar during prolonged sampling can also reduce culturability [62]. Liquid-based samplers can be used for longer durations without overloading, though the collection fluid may evaporate and require replenishment. Automated samplers with liquid volume control help mitigate this issue [50].

Main Sampling Principles

The central objective of bioaerosol sampling is to capture airborne biological particles and preserve their properties for analysis. Bioaerosol samplers can be broadly categorized into active and passive methods.

Active samplers rely on mechanical devices, such as pumps, to draw air into the sampling device, enabling the quantification of bioaerosols in a given volume of air. These samplers are preferred when accurate concentration measurements are required. However, the need for air movers and power supplies can limit their mobility, particularly in environments where long sampling times or high-pressure drops are encountered.

Battery-powered samplers, while portable, are often constrained by limited operational times due to battery capacity [63].

In contrast, *passive samplers* collect particles through natural forces, such as gravity or electrostatic attraction. These samplers are typically less expensive and easier to deploy but offer only qualitative data because the sampled air volume is unknown. Despite this limitation, passive samplers are useful for monitoring surface contamination in environments like sterile surgical rooms or food production lines [64].

Types of Samplers

There are several types of bioaerosol samplers, see Figure 2.5, each with distinct collection mechanisms and performance characteristics:

- *Filtration-based samplers* capture particles by passing air through a filter, where bioaerosols are trapped and can later be eluted into liquid for analysis. Filters are easy to use and allow for direct examination of particles using techniques such as electron microscopy or culture-based assays. Commonly used filters include polycarbonate, mixed cellulose ester, and gelatin filters. Gelatin filters, in particular, are advantageous for preserving the culturability of microorganisms, as they can be dissolved in a buffer or directly placed on agar for culturing [65] [66].
- *Impaction-based samplers*, such as the Andersen multi-stage impactor, collect particles by inertia, forcing airborne bioaerosols to impact onto a solid surface. These samplers are commonly used in bioaerosol studies because they enable direct culturing of collected microorganisms on agar plates. However, the high velocity of the air streams in these devices can cause mechanical damage to delicate microorganisms, reducing their culturability [67].
- *Liquid-based samplers*, like the BioSampler®from SKC, combine impingement and centrifugal forces to collect bioaerosols into a liquid medium. The BioSampler®is widely used due to its ability to reduce mechanical stress on microorganisms, thus preserving their viability better than traditional impingers. It operates at a flow rate of 12.5 L/min and is often used in conjunction with isotonic collection fluids like phosphate-buffered saline (PBS), which maintain the integrity of bioaerosols during sampling [68] [69].
- *Electrostatic samplers (ESPs)* use an electric charge to attract bioaerosol particles, which are then deposited onto a collection surface through electrostatic forces. These samplers cause less mechanical stress to collected bioaerosols compared to impaction-based methods, preserving their integrity for further analysis. ESPs are

compatible with various collection media, including agar plates, liquid, and solid surfaces. One downside of ESPs is the potential production of ozone during the charging process, which can negatively affect the viability of microorganisms [70] [55].

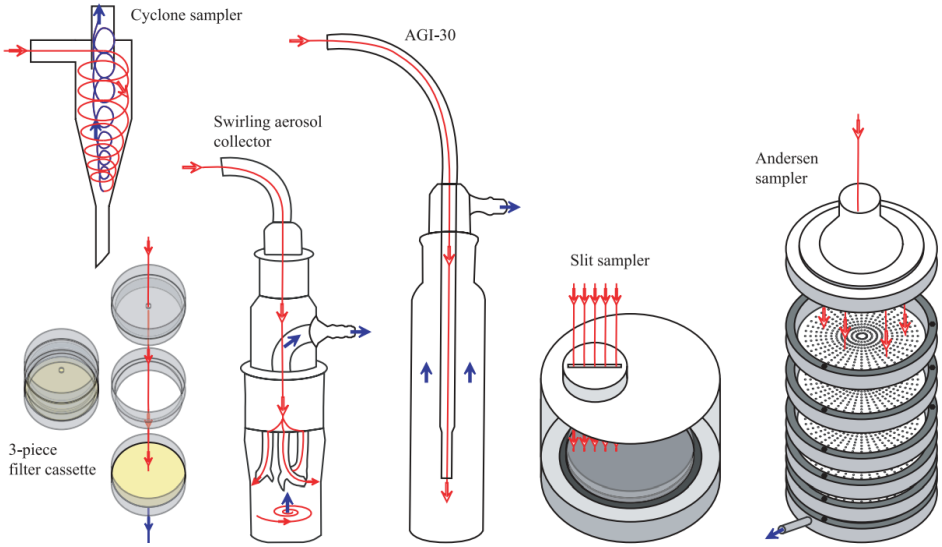

Figure 2.5 – Diagrams of six different bioaerosol samplers. Red lines and arrows represent the airflow into the sampler. Blue arrows represent airflow out of the sampler. These drawings are simplified representations. Source: [71].

Bioaerosol sampling is inherently complex due to several factors:

- **Sampler variability:** Different commercially available samplers, and those described in the literature, operate based on various mechanisms—such as filtration, impaction, impingement, and electrostatic precipitation. These devices differ in their sampling efficiency, cutoff sizes, flow rates, and collection media, which can result in variations in the bioaerosol data they produce. For example, some samplers may be more suited for capturing specific bioaerosol sizes or types (e.g., bacteria versus viruses), leading to inconsistencies when comparing results across different studies [64].

- **Analysis constraints:** The choice of a sampling method often dictates the type of analytical tools that can be employed. For instance, some methods are more compatible with culture-based techniques, which assess the viability of bioaerosols, while others are suited for genetic analysis, such as qPCR or gene sequencing, which quantify total microbial DNA. However, no single sampling method can capture the full spectrum of bioaerosol properties. Recent advances in gene sequencing have expanded our understanding of microbial diversity in air, but

they also introduce challenges in terms of preferential capture and the effects of sampling bias [49].

- **Low bioaerosol concentrations:** Typical indoor and outdoor environments often have low concentrations of bioaerosols or experience temporal fluctuations in bioaerosol levels. Many of the available sampling technologies struggle to capture representative samples over these conditions due to their relatively low flow rates or short sampling durations, which can result in incomplete or misleading data [64].

These challenges have limited the ability to standardize bioaerosol sampling protocols and establish accurate dose–response relationships.

BioSampler ®

The BioSampler ®from SKC, Figure 2.6, a widely recognized liquid-based sampler, was selected for this study because it minimizes stress on bioaerosol particles [15, 69] compared to traditional impingers and has become a *de facto* reference sampler in bioaerosol studies . The BioSampler ®uses a swirling motion to reduce direct impingement forces, lowering the likelihood of damage to cell membranes and maintaining culturability. This feature makes it ideal for preserving the biological activity of captured microorganisms, particularly in environments where short-term sampling is needed.

The BioSampler ®must operate at a flow rate of **12.5 L/min** to ensure proper functioning. At this rate, the air entering through the three 0.630-mm tangential sonic nozzles generates a swirling motion in the collection liquid, which is essential for capturing bioaerosols effectively. If the flow rate is too low, the vortex does not adequately interact with the incoming air, leading to reduced or no bioaerosol capture. Conversely, if the flow rate is too high, there is an increased risk of causing greater stress to the microorganisms, potentially compromising their integrity. This indicates that the 8 LPM exiting the BLAM output is insufficient to meet the required sampling flow rate. Since the system requires two impingers, *Control* and *Treated*, a dilution air line must be introduced. This additional line must provide 17 LPM to achieve the total 25 LPM needed by the impingers. After combining the BLAM output with the dilution air, the bioaerosol is split for sampling both before (*Control sample*) and after (*Treated sample*) the plasma treatment inside the GAPS reactor, as shown in Figure 2.1.

One significant challenge in liquid-based sampling is re-aerosolization, which occurs when captured particles are released back into the air due to evaporation or mechanical agitation. This leads to potential underestimation of bioaerosol concentrations. For

Figure 2.6 – BioSampler ®by SKC company.

instance, the evaporation rate in the BioSampler ®can reach approximately 0.19 ml/min, contributing to re-aerosolization during longer sampling periods [72]. To minimize this, it is crucial to limit sampling durations to avoid excessive evaporation. The evaporation rate is accounted for in the calculation of the results, as detailed in Section 2.2.3.

The choice of collection liquid plays a crucial role in ensuring the viability and integrity of bioaerosols during sampling. Phosphate-buffered saline (PBS) is frequently used due to its isotonic properties, which prevent osmotic stress on microorganisms. It has been shown that PBS provides an ideal environment maintaining the pH and ionic balance, which supports microbial viability without requiring additional osmoprotectants, for short sampling duration, in contrast to deionized water (DI), which can cause osmotic stress, leading to rapid loss of viability [53].

For this study, PBS was selected as the collection liquid due to its ability to preserve microbial integrity during short-term sampling, as the experiments in this research will be conducted within a 5 to 15-minute time frame.

To ensure reliable and reproducible data, two BioSampler were used in the setup, as shown in Figure 2.1. This *dual-impinger* configuration is critical, as it allows for simultaneous sampling, providing a precise internal control for each experiment. The use of a dedicated Control BioSampler for baseline measurements ensures that any bacterial losses occurring within the setup before reaching the Control sampling point do not interfere with the experimental outcomes. This approach ensures that the observed effects are accurately attributed to the experimental treatment and not to incidental losses within the system. This statement is validated by conducting measurements with the plasma turned off to observe the performance of the BioSamplers in the setup.

This approach ensured that both BioSamplers provided consistent results under non-treatment conditions, confirming that they have the same sampling efficiency and can be reliably compared to each other. Additionally, these tests verified that there were no losses between the two sampling points in the experimental setup. Once this consistency was established, any differences observed with the plasma turned on could confidently be attributed solely to the treatment effect. The results of these control experiments are presented in Section 3.3.

2.2.2 CFU Method Introduction

Bioaerosols can be categorized based on their viability and culturability. Culturable bioaerosols are those that can grow under laboratory conditions, providing a direct measure of living microorganisms. Non-viable bioaerosols include those organisms that are dead and thus cannot be cultured. Non-culturable bioaerosols may still be alive but fail to grow in the laboratory environment due to their stringent ecological requirements or dormant state. Depending on the specific objectives of a study, different bioaerosol analysis techniques are employed. These methods vary based on the biological state of the target organisms (culturable, viable, non-viable, or non-culturable) and the type of information required. A brief overview of the principal existing analysis techniques is listed below. A more detailed discussion can be found in [73] [74].

- **Microscopy**: This method allows for the direct visual observation of bioaerosols. Bright-field and phase-contrast microscopy are common, with the latter providing better visualization of cells due to differences in light refraction.
- **Culturing Techniques**: Traditional microbiology methods involve growing organisms on nutrient media. This method is simple and cost-effective but only detects a fraction of the total bioaerosols due to the non-culturable nature of many organisms.
- **Molecular Techniques**: Techniques such as PCR and sequencing allow for the identification of bioaerosols at the molecular level. These methods can detect both culturable and non-culturable organisms but require sophisticated equipment and expertise.
- **Mass Spectrometry**: Used for identifying biochemical markers and profiling microbial communities. It offers rapid analysis and high specificity but requires extensive sample preparation.

- **Immunoassays**: Employ antibodies to detect specific proteins in bioaerosols, providing information about the types of organisms present. These assays are sensitive but can sometimes lack specificity in complex samples.
- **Bioluminescence - ATP Assay**: Detects living cells through the presence of adenosine triphosphate (ATP), giving a direct measure of cell viability. It is quick and effective for assessing microbial contamination.

For the preliminary phase of this research, the Colony Forming Unit (CFU) method was chosen due to its simplicity and effectiveness in measuring viable, culturable bacteria. It provides a direct count of living microorganisms capable of growth in a controlled environment, crucial for assessing the efficacy of antimicrobial treatments. While other methods offer broader information on community composition and non-culturable entities, the CFU approach is particularly suitable for initial studies focusing on microbial viability and treatment validation.

Methodology Overview

Colony counting is restricted to plates with colony counts falling within the range of 10 to 300. Colonies outside this range are excluded from the count due to their potential lack of accuracy. To determine the total number of colonies N in the initial solution, we employ the following equation:

$$N_{\text{initial}} = \frac{N_{\text{colonies}}}{j_1 + 0.1 j_2} \cdot D \tag{2.1}$$

where:

- N_{initial} is the total number of colonies in the initial solution.
- N_{colonies} is the cumulative count of colonies on all plates included in the counting process.
- j_1 represents the number of counted plates at the lowest dilution level considered.
- j_2 denotes the number of counted plates at the next higher dilution level.
- D is the reciprocal of the lowest dilution factor.

Owing to the protocol employed in this study, both j_1 and j_2 consistently assume values of either 0 or 1, as only one plate is prepared for each dilution. Among the six dilutions subjected to treatment, only one or two plates are suitable for counting. Therefore, Equation (1) can be simplified to:

$$N_{\text{initial}} = \frac{N_{\text{colonies}}}{1.1} \cdot D \quad \text{or} \quad N_{\text{initial}} = \frac{N_{\text{colonies}}}{1} \cdot D \tag{2.2}$$

The number of dilutions counted determines whether we have data from 1 or 2 plates, as will be detailed subsequently in 2.2.3.

Preparation of Bacterial Solution

This section elaborates on the procedures involved in preparing, treating, and analyzing the non-pathogenic *Escherichia coli* strain *K-12 MG1655* [75] under experimental setups designed to assess the efficacy of decontamination treatments. This strain is chosen for its rapid replication capabilities and extensive use in biological research as reported in 1.1.1.

Figure 2.7 shows the bacterial growth curve, which illustrates the typical growth phases that bacterial populations undergo over time including lag, exponential, stationary, and death phases. Understanding this curve is crucial for determining the optimal time to apply treatments to achieve accurate and consistent results. The *lag phase* is the initial period where bacteria adapt to their new environment; during this phase, there is little to no increase in cell number as bacteria prepare for future growth by activating specific genes and synthesizing essential enzymes. Following the lag phase is the *exponential (or log) phase*, characterized by rapid bacterial multiplication where the rate of growth is constant and the population size doubles at regular intervals. This phase reflects the maximum rate of cell division under the given conditions. The *stationary phase* is reached when the growth rate slows and stabilizes as nutrient levels deplete and waste products accumulate, leading to a balance between cell division and cell death. Finally, the *death phase* occurs when the rate of cell death exceeds the rate of new cell growth due to the continued depletion of nutrients and the accumulation of toxic waste, leading to a decline in the overall population.

Starting from a stock stored at -80°C, *E. coli* cells are reactivated by inoculating 100 μL into 10 ml of Luria-Bertani (LB) medium and incubated overnight at 37 °C with agitation at 180 rpm. This process is crucial for reviving the cells from their dormant state as shown in Figure 2.8.

Post-incubation, the culture is prepared for nebulization by suspending it in phosphate-buffered saline (PBS), as detailed in Figure 2.9 through centrifuging and washing. This suspension is used in aerosol experiments where bacteria are subjected to plasma treatment. A total of approximately 6 ml of bacterial suspension was obtained and the culture reached an optical density (OD) between 1.3 and 1.9, corresponding to roughly

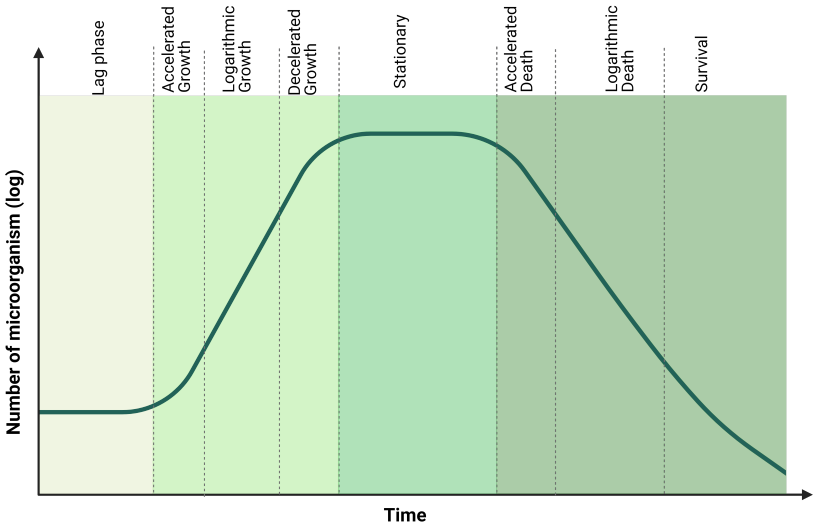

Figure 2.7 – Bacterial growth curve showing different phases of *Escherichia coli* development.

$10^9 CFU/ml$, indicating a high cell density suitable for the experiments. Before the treatment, 1 ml was plated immediately to ascertain the initial bacterial concentration inside the prepared solution. Deciding the initial concentration is not an easy task due to the broad variety of bacterial concentration studied for pathogens disinfection [76]. A good starting point is above $10^9 CFU/ml$.

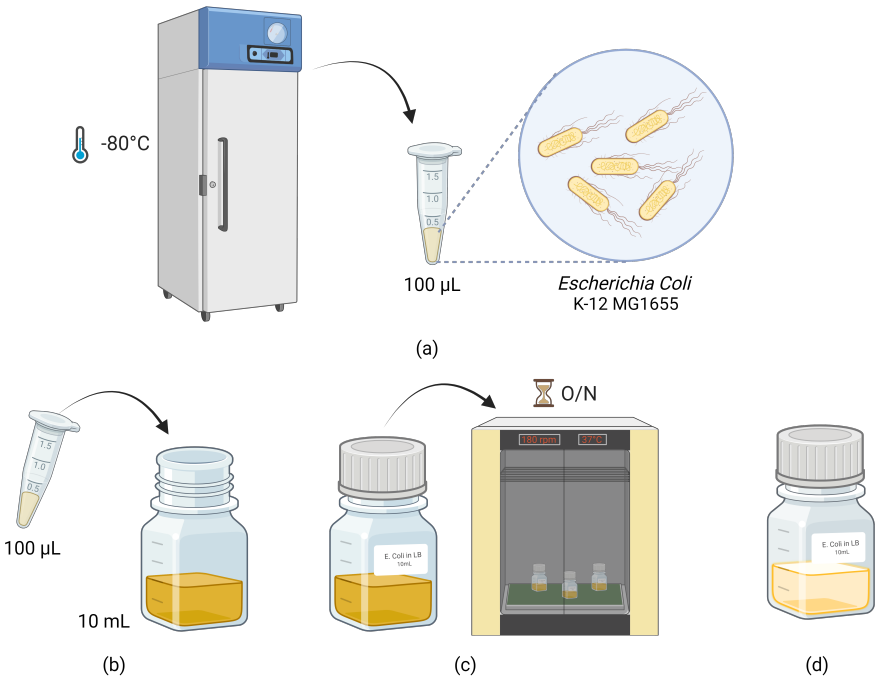

Figure 2.8 – Process of reactivating *E. coli*. (a) a batch of *E. coli* from the $-80°C$ storage. (b) 100 μL *E. coli* inoculated into 10 ml of LB. (c) incubation overnight at $37°C$. (d) final bacterial suspension.

For the plasma treatment, the bacterial suspension in PBS was injected inside the syringe for the syringe pump to use and then pumped into the BLAM jar at a flow rate of 0.28 ml/min with the nebulizer operating in SPA mode for 7 minutes, using only 2 ml of the prepared volume, as explained previously in 2.1.

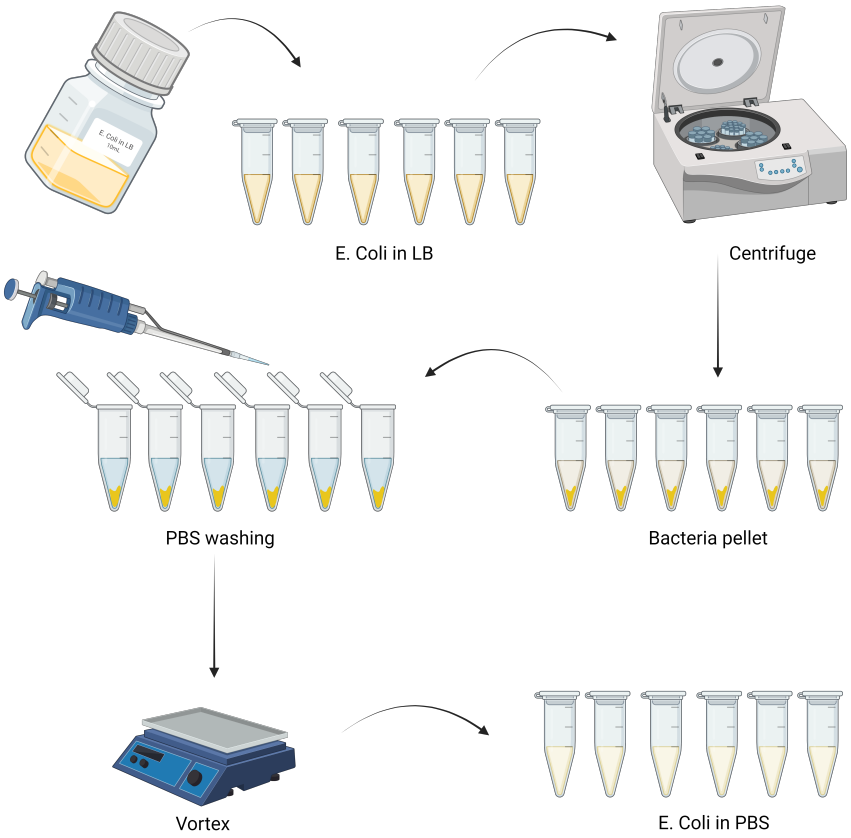

Figure 2.9 – Preparation of *E. coli* suspension in PBS for nebulization. The overnight solution is centrifuged to collect the bacteria pellet for the PBS washing and then the washed solution is used for nebulization.

The viability of bacteria post-treatment is assessed using the colony count assay. This involves creating serial dilutions, plating on LB agar, and counting the resulting colonies. The process, crucial for evaluating bacterial survival, is illustrated in Figure 2.10. The PBS solution collected from the BioSamplers, installed physically before and after the treatment, was designated as *Control* and *Treated* respectively. This solution was mixed thoroughly for 1 minute before conducting serial dilutions and plating for CFU enumeration to ensure maximum homogeneity before taking the sample.

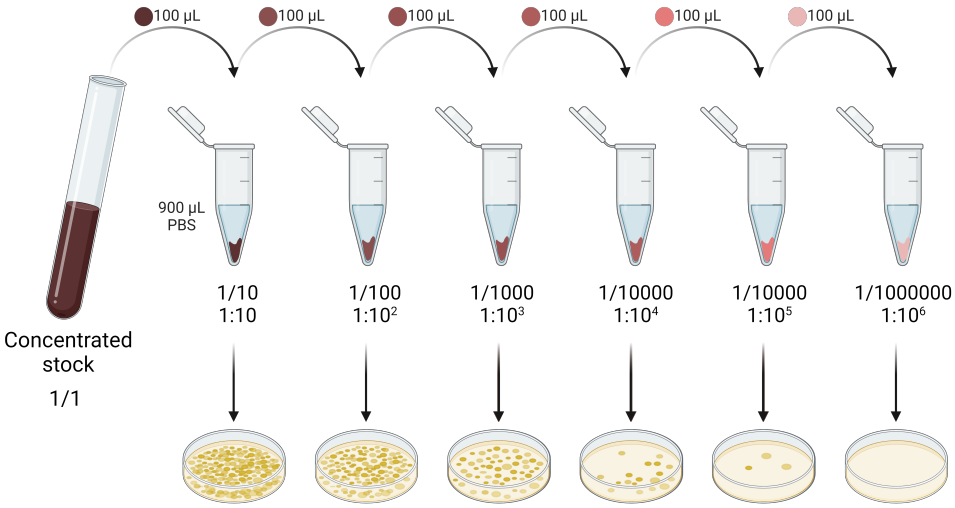

Figure 2.10 – Serial dilution method. This diagram shows the preparation of serial tenfold dilutions from a concentrated bacterial stock (1/1 to 1/1,000,000), including the initial 100 μL transfer into 900 μL PBS, followed by agar plating to assess bacterial growth.

Each step of the CFU method is replicated three times (*technical replicates*) for each experiment to provide a robust evaluation of the decontamination treatments on *E. coli*, ensuring that all procedures are standardized to yield reproducible and accurate results. Each experiment was replicated three times on different days (*biological replicates*) to average the experiment's results. The average ofCFU counting is used to estimate the uncertainty range of the bacterial concentration in the solutions.

2.2.3 Quantification of Antibacterial Activity

The antibacterial activity was quantified using the log reduction formula, an established convention in microbiology:

$$R = \log_{10}(C_b) - \log_{10}(C_a) = \log_{10}\left(\frac{C_b}{C_a}\right) \tag{2.3}$$

where:

- C_b is the concentration of the contaminant before treatment,
- C_a is the concentration of the contaminant after treatment.

A higher value of R indicates a more effective treatment, with each unit of R representing a tenfold reduction in contaminant concentration. For example, an R value of 2 means

the concentration is reduced to one-hundredth of its original level, it can be denoted as 2-log.

Log reduction values are often converted to percentages to provide a more intuitive understanding of the treatment's effectiveness. The percentage reduction P can be calculated as:

$$R_p = \left(1 - \frac{C_a}{C_b}\right) \times 100\% \tag{2.4}$$

Set-up Efficiency

The goal of this section is to calculate the final concentration of colony-forming units (CFU) in the impinger liquid after the bioaerosol sampling process in an ideal situation without mechanical losses due to the set-up. The process begins with an initial bacterial suspension concentration of 10^9 CFU/ml, which is aerosolized and diluted as it moves through the experimental setup.

The initial concentration of *Escherichia coli* in the syringe pump is:

$$C_{\text{initial}} = 10^9\,\text{CFU/ml}$$

For the experiment, a total of 2 ml of this solution is injected into the nebulizer:

$$V_{\text{injected}} = 2\,\text{ml}$$

Thus, the total number of CFU in the injected liquid is:

$$N_{\text{injected}} = C_{\text{initial}} \times V_{\text{injected}} = 10^9\,\text{CFU/ml} \times 2\,\text{ml} = 2 \times 10^9\,\text{CFU}$$

The nebulization process operates at an efficiency of 1% [42], this means only 1% of the total CFU are successfully aerosolized:

$$N_{\text{nebulized}} = N_{\text{injected}} \times \text{efficiency} = 2 \times 10^9\,\text{CFU} \times 0.01 = 2 \times 10^7\,\text{CFU}$$

Thus, 2×10^7 CFU are aerosolized and available for further dilution in the airflow.

The aerosolized CFU are then diluted in the total airflow of $\dot{Q_{\text{tot}}}$ = 25 LPM (liters per minute), consisting of 8 LPM from the nebulizer and an additional 17 LPM of dilution air:

$$C_{\text{air}} = \frac{N_{\text{nebulized}}}{\dot{Q_{\text{tot}}}} = \frac{2 \times 10^7\,\text{CFU}}{25\,\text{LPM}} = 8 \times 10^5\,\text{CFU/LPM}$$

Thus, the concentration of CFU in the airflow is 8×10^5 CFU/LPM.

During the experiment, only 12.5 LPM of the total airflow is sampled through the impinger $\dot{Q}_{\text{impinger}}$:

$$N_{\text{impinger}} = C_{\text{air}} \times \dot{Q}_{\text{impinger}} \times \text{t} = 8 \times 10^5\,\text{CFU/LPM} \times 12.5\,\text{LPM} \times 7\,\text{min}$$

$$N_{\text{impinger}} = 7 \times 10^7\,\text{CFU}$$

Thus, 7×10^7 CFU are collected in the impinger during the 7-minute experiment.

The impinger initially contains $V_{impinger}$ = 20 ml of liquid. However, due to evaporation, the volume decreases over the course of the experiment. The evaporation rate is given as 0.19 ml/min [72], so the total evaporated volume is:

$$V_{\text{evaporated}} = 0.19\,\text{ml/min} \times 7\,\text{min} = 1.33\,\text{ml}$$

Therefore, the remaining volume of liquid in the impinger is:

$$V_{\text{remaining}} = 20\,\text{ml} - 1.33\,\text{ml} = 18.67\,\text{ml}$$

The final concentration of CFU in the remaining liquid in the impinger in an ideal situation can be calculated by dividing the number of CFU sampled by the remaining liquid volume:

$$C_{\text{impinger}} = \frac{N_{\text{impinger}}}{V_{\text{remaining}}} = \frac{7 \times 10^7\,\text{CFU}}{18.67\,\text{ml}} \approx 3.75 \times 10^6\,\text{CFU/ml} \tag{2.5}$$

Thus, the final concentration of CFU in the impinger liquid is approximately 3.75×10^6 CFU/ml. This is the concentration that should be found in the *Control* impinger (previous plasma treatment) in an ideal situation. It is important to note that several factors contribute to the reduction in concentration observed at the *Control* impinger. Losses are introduced by the material and bends of the tubing, the overall length of the tubing, and finally by the sampling efficiency of the impinger itself. These factors ensure that the concentration measured at the *Control* impinger will inevitably be lower than the theoretical value calculated for an ideal system, as reported in Section 3.3.

To prove a high disinfection rate with the log reduction formula, a higher initial concentration should be used. Due to laboratory limitations, the maximum concentration reachable was 10^9 CFU/ml. This means that, given the ideal concentration of 3.75×10^6 CFU/ml, the maximum achievable log reduction will be up to $\leq 6 - log$ (CFU/ml).

Counting Calculation

Colony counting is restricted to plates with colony counts falling within the range of 10 to 300, as counts outside this range may be unreliable. This means that only two dilutions are typically acceptable for accurate counting. However, we performed 8 serial dilutions from the initial solution (which had a high concentration of 10^9 CFU/ml) to ensure the plates were not contaminated and to confirm that the dilutions maintained a consistent order of magnitude difference. For the control and treated samples, since the expected concentration was below 10^6 CFU/ml, due to losses as previously explained, we performed 4 dilutions but only used two for the final count. Each experiment was repeated three times each day for *technical* replicates, for three different days for *biological* replicates. The results presented in Chapter 3 are the average values from these experiments, with corresponding error bars indicating the variability.

2.3 Bioaerosol Treatment

This section provides a comprehensive overview of key factors that must be considered in a plasma treatment. Sub-section 2.3.1 provides an in-depth description of GAPS design, elaborating on the structural components and operational parameters that influence plasma generation. The choice of materials, electrode configuration, and dielectric properties are discussed, emphasizing their role in generating a stable and efficient discharge. Following the description of the reactor's design, sub-section 2.3.2 outlines the design of the custom power supply used to drive the GAPS, focusing on the high-voltage pulsed signal applied to maintain the plasma.

Sub-section 2.3.3 introduces the methods employed for the physical characterization of the DBD reactor, focusing on power measurement techniques, which are essential for understanding the energy input into the system and its relation to the observed treatment effects on bioaerosols.

Finally, sub-section 2.3.4 discusses the chemical characterization of the plasma environment through the technique of Fourier Transform Infrared Spectroscopy (FTIR). The FTIR analysis provides insights into the chemical species generated during the plasma treatment and their potential role in the inactivation of microorganisms. This section lays the groundwork for interpreting the results presented in Chapter 3.

2.3.1 GAPS Reactor Design

The DBD reactor presented in this study, GAPS, is specifically designed to optimize homogeneous plasma generation while ensuring durability and ease of maintenance. The reactor consists of two grid-like electrodes made of stainless steel AISI 301, selected for its resistance to ozone-induced corrosion and moisture. This material choice ensures long-term stability and reliability of the electrodes in harsh operational environments, where both high humidity and reactive oxygen species are present. The grid-like electrodes were designed at the PTL laboratory in Bologna and produced by Chimimetal through a chemical photoetching process, ensuring precise and uniform patterns.

The grid-like electrodes have an external diameter of 92 mm, with a mesh size of 2x2 mm and a spacing of 0.42 mm between the individual wires, see Figure 2.11. One of the electrodes is coated with a dielectric layer made of Rilsan ES ®, a polyamide material known for its high dielectric strength and chemical resistance. The coating process was performed by ZOCCA Coatings, a company specializing in advanced coating solutions. The Rilsan coating is applied to both sides of the electrode, with a thickness of 150 micrometers per side. The dielectric stress rating of Rilsan is 10 kV/mm (from 100 µm thickness), allowing it to safely withstand voltages up to 1.5 kV, ensuring that the applied voltage remains within safe operational limits. The material has a dielectric constant of 3.9, which is typical for polymer dielectrics, and plays a crucial role in limiting current flow and preventing the formation of arcs during plasma generation. This enables the reactor to maintain stable and uniform plasma conditions.

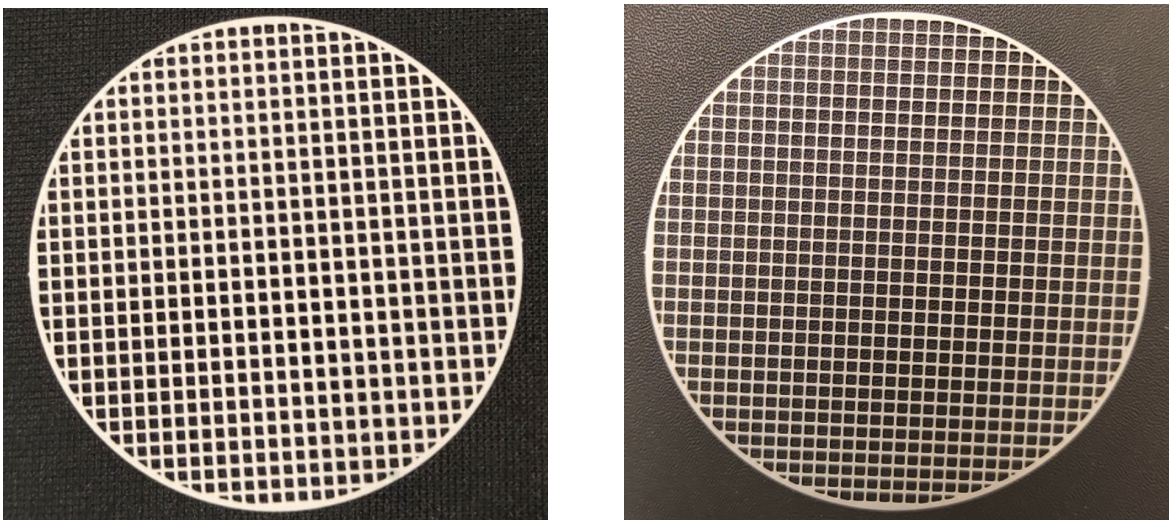

(a) (b)

Figure 2.11 – Photo of the grid-like electrode. (a) coated electrode with Rilsan ES ®. (b) non-coated electrode

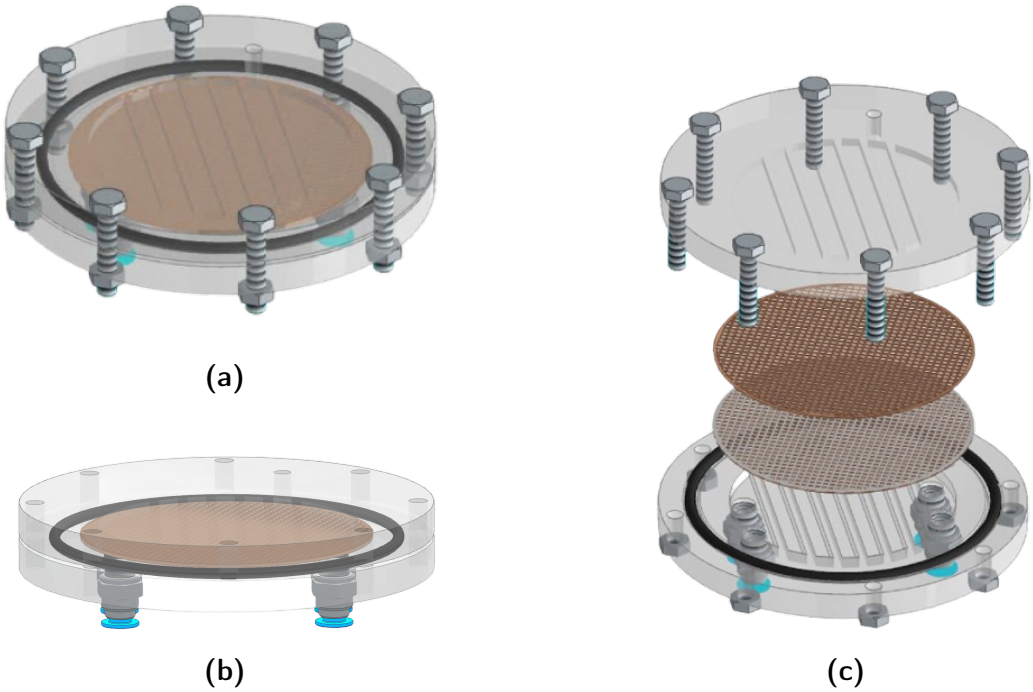

Figure 2.12 – CAD views of GAPS final design. (a) top view, (b) side view, and (c) exploded view for better understanding.

Another key advantage of Rilsan is its excellent chemical inertness, especially against corrosive agents such as ozone, which is often generated during plasma processes. Widely used in the food industry, Rilsan is well known for its resistance to chemical degradation, ensuring that the dielectric layer remains intact and operational over long periods, even under the challenging conditions created by plasma discharges.

Due to the geometry of the reactor, which features a grid mesh with 2 mm spacing, the discharge occurs primarily along the dielectric surface and does not occur in the volume between the grid holes. This happens because the field distribution is not sufficiently confined to induce breakdown within the gas volume. As a result, the plasma remains localized on the dielectric surface in proximity to the mesh, rather than extending through the holes. This makes the discharge an SDBD configuration.

The grid electrodes are held in place by two precision-machined plexiglass discs, fabricated using CNC (Computer Numerical Control) technology. This machining ensures precise alignment of the grids and creates a robust support structure. The transparent plexiglass allows visual inspection of the plasma during operation, facilitating real-time monitoring.

The CNC-etched serpentine path within the plexiglass creates a controlled flow channel for the bioaerosol, maximizing exposure to the plasma. The entire assembly is secured

with bolts and nuts, while an FKM (Viton) O-ring ensures an airtight seal, preventing leakage of the bioaerosol and maintaining the experimental integrity.

GAPS is equipped with four flow ports (two inlets and two outlets) with 6mm Festo connectors, and two SMA connectors for external electrical connections to the grid electrodes.

A detailed exploded view of the reactor's CAD model and photographs of GAPS fully assembled is shown in Figure 2.12. In Figure 2.13 the view of the real GAPS structure is provided.

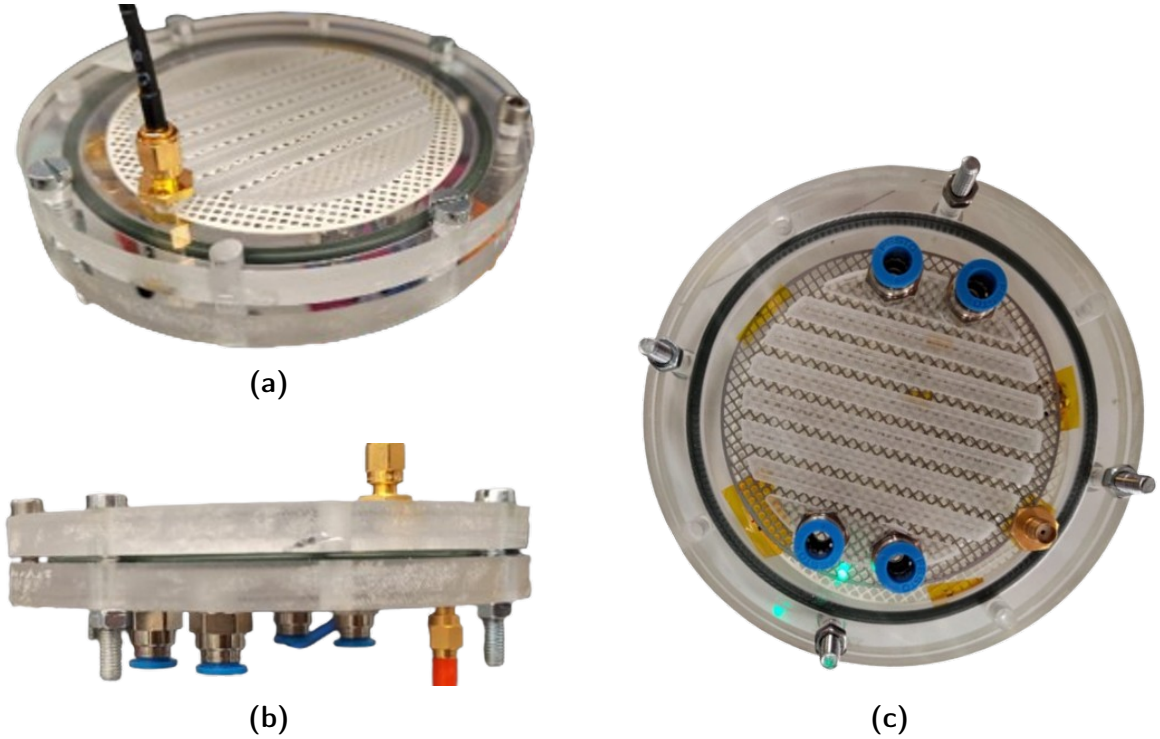

Figure 2.13 – Photo of the final DBD reactor design from different perspectives. (a) top view, (b) side view and (c) bottom view.

The GAPS is specifically designed to maximize the interaction between the bioaerosol and the plasma field, a key factor for achieving effective treatment. The geometry of the reactor ensures that the bioaerosol is directed through a carefully engineered flow path, which promotes prolonged and consistent exposure to the plasma. The CNC-etched serpentine channel within the plexiglass discs guides the bioaerosol in a controlled manner, ensuring that the aerosol flows parallel to the plasma discharge along the surface of the dielectric layer. This design prevents the bioaerosol from bypassing the active plasma region, enhancing the overall efficiency of the treatment process.

Additionally, the reactor's flow ports are strategically positioned to maintain a uniform distribution of the bioaerosol as it enters and exits the treatment zone, preventing areas of stagnant flow or under-treatment. The choice of grid-like electrodes, combined with the (SDBD) configuration, ensures that the plasma is uniformly distributed across the dielectric surface, further optimizing the interaction with the bioaerosol.

A more detailed analysis of how the reactor geometry influences flow patterns and ensures maximal plasma exposure is provided in the subsection 3.1.2, where a computational fluid dynamics (CFD) simulation illustrates the precise behavior of the bioaerosol within the GAPS.

2.3.2 Power Supply Design

To successfully ignite a DBD, an alternating voltage is required to initiate and sustain the plasma formation. In the present setup, a peak voltage of around 1,2 kV was deemed sufficient, as the breakdown voltage for the proposed GAPS system with a thin dielectric layer does not demand significantly higher values.

In order to achieve the desired output voltage, a dedicated power supply was built as follows. The design of the power supply was adapted from a pre-existing 49 multilevel generator [77] developed at PTL (Plasma Technology Laboratory), at the University of Bologna (previously known as Laboratorio di Ingegneria Magnetofluidodinamica e Plasmi (LIMP)). Only two modules from the multilevel were used, each capable of providing ±600 V DC, and were combined to produce a total bipolar output of ±1.2 kV. The configuration allowed for a flexible waveform output, enabling the generation of various bipolar pulse shapes. The unit module and the assembled power supply system are shown in Figure 2.14 and 2.15, respectively. The architecture of the power supply will be briefly introduced, for more details see [77].

Hardware System of the 5-Level H-Bridge Multilevel Inverter

The hardware system of the 5-level H-bridge multilevel inverter is composed of several key components that work together to generate high-voltage AC output. The primary goal of developing the multilevel H-bridge converter was to produce an AC output voltage in the range of 1.2 kV.

To meet these requirements, a 5-level cascaded H-bridge inverter is selected, consisting of 2 elementary units connected in series. Each elementary unit is capable of outputting

$\pm 600V$, allowing the system to reach a total output voltage of 1.2 kV, or 2.4 kV peak-to-peak when both units are active. This design enables high-voltage resolution and provides the flexibility to generate complex waveforms.

Each elementary unit is composed of three key functional parts:

- **Power Supply Stage:** Powered by a AC/DC 220/12V power supply.
- **Regulated Voltage Step-Up Stage:** Implemented using a flyback converter.
- **DC/AC Stage:** Uses an integrated power module to convert the DC input to AC.

Since here only two modules are exploited, no isolation is needed for the transformer unit due to relative low maximum voltage output. The flyback converter is widely used in DC/DC converters because it provides galvanic isolation between the input and output stages through the use of a transformer. The flyback topology was chosen due to its simplicity, robustness, and the minimal number of components required for implementation.

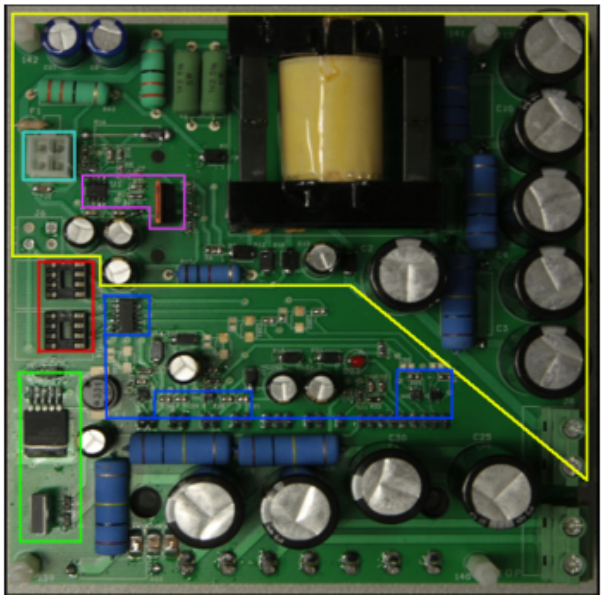

Figure 2.14 – Front of the PCB showing the components layout of the two modules, including flyback converter, DC/AC stage, and fiber optic isolation. Source: [77].

When the switch is turned on, current flows through the primary winding of the transformer, storing energy in the magnetic field. When the switch is turned off, the energy stored in the primary winding is transferred to the secondary winding, generating the output voltage.

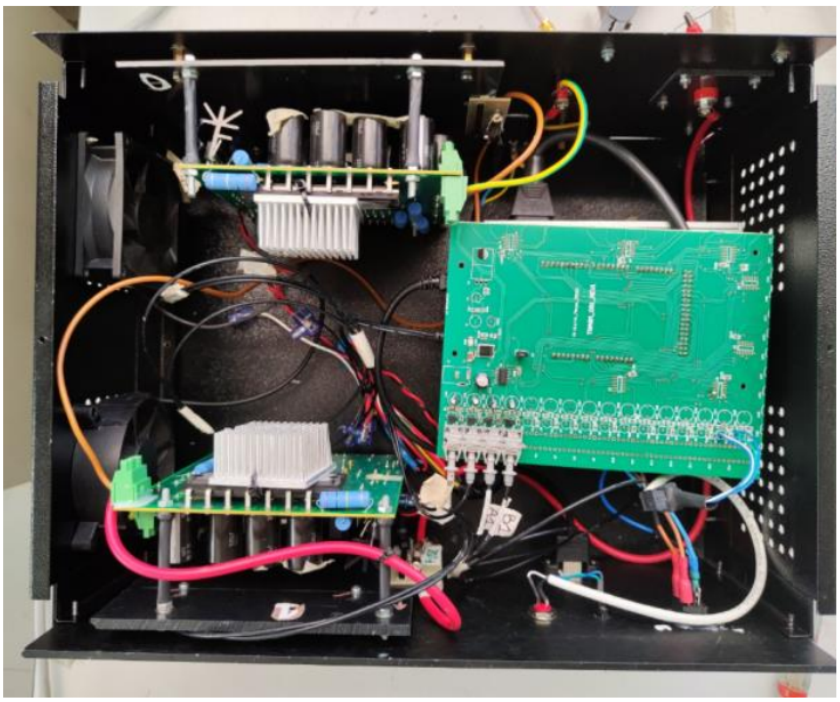

Figure 2.15 – The full generator setup with two modules in series, providing the bipolar ±1.2 kV output for the GAPS.

Each elementary unit of the inverter is implemented on a single printed circuit board (PCB), which integrates both the step-up stage (flyback converter) and the DC/AC inverter stage, see Figure 2.14. The PCB is divided into two main sections:

- **Flyback Converter Section:** Includes the transformer, MOSFET switch, PWM regulator, voltage regulators, and the dead-time generation circuit (yellow box in Figure 2.14).
- **DC/AC Section:** Incorporates the integrated inverter module (Figure 2.16) and associated components (bottom part in Figure 2.14).

The main parts of the flyback are:

- The AC/DC 220/12V power supply input connector (cyan)
- The transformer
- The Mosfet and the PWM regulator (purple)
- The two low voltage regulators (green)
- The placing for the Fiber optics (red)
- The dead time generation circuit (blue)

The flyback converter can operate in two modes: *Continuous Mode:* Some energy remains in the transformer at the end of each switching cycle. *Discontinuous Mode:* All energy stored in the transformer during the "on" period is transferred to the output during the "off" period. For this project, the discontinuous mode was selected to avoid instability and ensure smooth operation. The flyback converter generates a 600V DC output, which forms the DC bus for the DC/AC stage of the elementary unit.

The DC/AC stage of each elementary unit converts the 600V DC generated by the flyback converter into AC. To minimize the size of the unit, an integrated power module was used. This module includes a three-phase inverter based on IGBT technology, with built-in protections against over-current, under-voltage, and overheating. Since the multilevel inverter is a single-phase system, only two legs of the three-phase module are used, with the third leg serving as a backup.

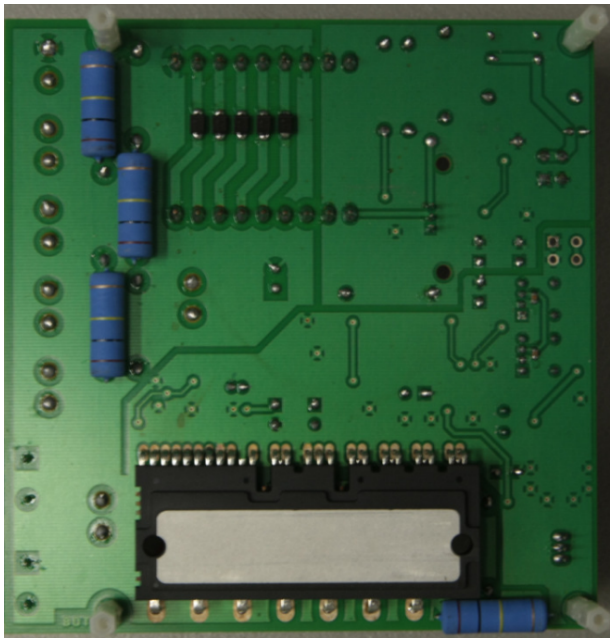

Figure 2.16 – Back of the PCB showing the integrated power module, which incorporates a three phase inverter and the driving circuit. Source: [77].

The control system for the MOSFET switch in the flyback converter is implemented using a current mode PWM controller, powered by the 12V DC power supply. The control signals for the DC/AC stage are transmitted via fiber optics to ensure galvanic isolation between the low-voltage control electronics and the high-voltage output. Additionally, dead-time generation circuits are implemented to prevent simultaneous conduction of the IGBTs in the H-bridge, which could otherwise result in a short circuit. This design ensures safe and reliable operation of the inverter.

The multilayer generator enables an exceptionally fast rise time, approximately $6kV/\mu s$, allowing the system to reach high voltage levels within extremely short timescales. This characteristic facilitates the creation of a strongly non-equilibrium plasma, distinguished by a molecular and atomic excitation dynamic that differs significantly from that achieved with low-voltage excitation methods or slower rise times.

The waveform generation was controlled through an Arduino microcontroller, which was programmed to implement a range of bipolar pulsed waveforms. After several trials with different waveform shapes, a square waveform with a plateau of 4 μs was found to be the most effective in driving the plasma discharge in terms of surface discharge homogeneity, the results are not presented. Thanks to the multilayer generator, adjusting the T_{OFF} time between discharges is both straightforward and feasible, offering an additional level of flexibility in discharge management and plasma configuration according to experimental needs. For this study, an interval of 1 ms was chosen as the T_{OFF} time between discharges to limit the active power of the system and prevent excessive production of undesired chemical species, such as ozone.

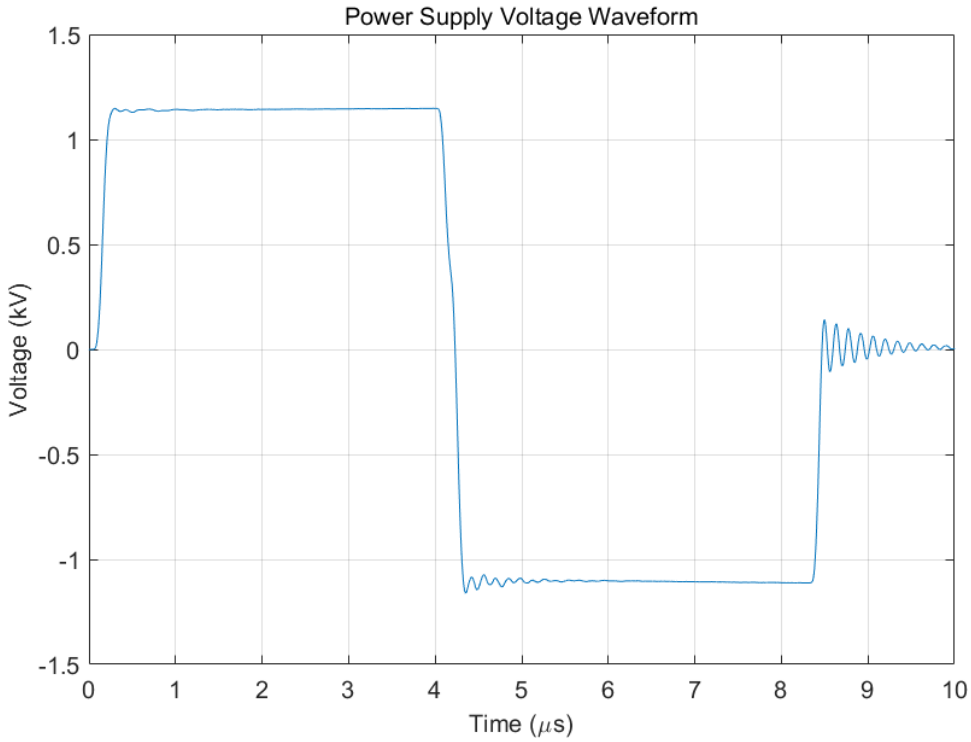

Figure 2.17 – Output square waveform generated by the system without load, showing ±1.2 kV peaks.

The output waveform, measured without load, is shown in Figure 2.17, confirming the generation of a clear square waveform with well-defined peaks at ±1.2 kV. This ensures

that the generator can consistently deliver the required voltage to the GAPS system under various operating conditions.

2.3.3 Physical Characterization Method

Physical characterization of GAPS enables the measurement of the discharge power, which is crucial for bioaerosol treatment, where it directly impacts treatment efficiency. The measurement of the discharge power is not straightforward, mainly for non-sinusoidal waveforms like the micropulsed bipolar waveform used in this study [78][79]. Three different methods are discussed: the classic current-voltage method, the Lissajous figure method, and the equivalent circuit method [80]. These approaches provide complementary insights into the power consumed by the reactor, enabling a more comprehensive evaluation of its efficiency.

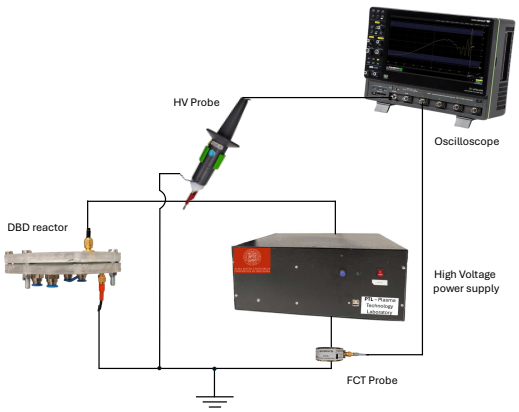

Figure 2.18 – Real electrical measurements circuit set up of GAPS reactor powered by the micropulsed generator, with a high-voltage (HV) probe, highly sensitive current probes and oscilloscope

Voltage-Current Method

The current-voltage method relies on the direct measurement of current and voltage applied to the reactor, as depicted in Figure 2.18. The instantaneous power is calculated as the product of current and voltage, $P(t) = v_m(t) \cdot i_m(t)$, and then integrated over the operating period to obtain the average dissipated power:

$$P_{average} = \frac{1}{T} \int_0^T v_m(t) i_m(t) dt \tag{2.6}$$

where T is the period of the voltage waveform,$v_m(t)$ is the measured voltage and $i_m(t)$ is the measured current . While this method is commonly used, it presents certain challenges, particularly in pulsed DBD systems. One key issue is the need for highly sensitive current probes and oscilloscopes capable of resolving the fast microdischarges that are typical of these systems. These microdischarges occur on the order of 10^{-7} seconds and are randomly distributed both spatially and temporally. As a result, capturing the transient behavior of these discharges requires high-bandwidth measurement equipment. On the other side, this approach offers several advantages: it does not require any a priori knowledge of the reactor's electrical parameters and provides a qualitative estimation of *active* power. It is crucial to ensure that the integration of the acquired data is performed over integer multiples of the discharge time T, or the *reactive* power in the capacitive part of the reactor will not average out to zero.

A significant challenge arises from the fact that the measured current during the plasma ON phase (plasma discharge) includes both capacitive current and plasma-generated current. The capacitive current, caused by the charging and discharging of the dielectric surfaces, must be subtracted to isolate the actual power dissipated in the plasma to actually measure the *instantaneous* power delivery into the discharge. This can be approached analytically by an equivalent circuit analysis.

Equivalent Circuit Method

In order to analyze the discharge current and voltage behavior in a DBD system, it is essential to decompose the components of the total current. One method involves modeling the system through an equivalent circuit approach, which separates the contributions from the dielectric and the gas gap parts [81] [82]. The limitation of this approach relies on the requested prior knowledge of the reactor's electrical parameters, the dielectric capacitance C_d and the gas gap capacitance C_g. The equivalent circuit approach, a method extensively studied and employed in past research, as examples [82] [78], represents the DBD reactor as a series of the dielectric capacitance C_d and the plasma discharge area. The latter is modeled by a parallel between the gas gap capacitance C_g and a plasma impedance Z_g, whish is treated as a 'black-box'.

The capacitance of the DBD reactor, C_{OFF}, is defined by the relationship between the dielectric capacitance, C_{d}, and the gas gap capacitance, C_{g}, according to the formula:

$$\frac{1}{C_{\mathrm{OFF}}} = \frac{1}{C_{\mathrm{d}}} + \frac{1}{C_{\mathrm{g}}}. \tag{2.7}$$

In fact, referring to the equivalent circuit in Figure 2.19, C_{d} and C_{g} are in series when the switch s is open, representing the non-discharging phase. During the plasma-on phase, the switch s is closed and plasma current $i_z(t)$ flows across the gas gap, modeled as a 'black box' in parallel with C_{gap}, due to the gap voltage $v_{\mathrm{g}}(t)$.

Referring to the equivalent circuit in Figure 2.19, the analysis begins with the following relationships :

$$v_d(t) = \frac{Q(t)}{C_d} \tag{2.8}$$

Here, $v_d(t)$ represents the voltage across the dielectric barriers, where C_d is the capacitance associated with the dielectric. The charge $Q(t)$ used to calculate this voltage can be derived by the measured current i_m.

$$v_g(t) = v_m(t) - v_d(t) \tag{2.9}$$

This equation defines the voltage across the gas gap $v_g(t)$, which is the difference between the applied voltage $v_m(t)$ and the voltage across the dielectric $v_d(t)$.

In this step, the displacement current through the gas gap $i_{dis}(t)$ is related to the time derivative of the gas gap voltage $v_g(t)$ and the gas gap capacitance C_g.

$$i_{dis}(t) = C_g \frac{dv_g(t)}{dt} \tag{2.10}$$

The total discharge current $i_z(t)$ is obtained by subtracting the current through the gas gap $i_{dis}(t)$ from the total measured current $i_m(t)$.

$$i_z(t) = i_m(t) - i_{dis}(t) \tag{2.11}$$

By substituting the expression for $v_d(t)$ into the equation for $v_g(t)$, we obtain a more explicit expression for the gas gap voltage:

$$v_g(t) = v_m(t) - \frac{Q(t)}{C_d} \tag{2.12}$$

This shows that the voltage across the gas gap $v_g(t)$ depends on both the applied voltage and the charge stored on the dielectric.

Further, by substituting the expression for $i_{dis}(t)$ into the equation 2.11, we derive the discharge current:

$$i_z(t) = i_m(t) - C_g \frac{dv_g(t)}{dt} \tag{2.13}$$

This equation shows that the total measured current is the sum of the discharge current and the displacement current through the gas gap. It emphasizes that the current $i_z(t)$, associated with plasma discharge, is distinct from the capacitive displacement current.

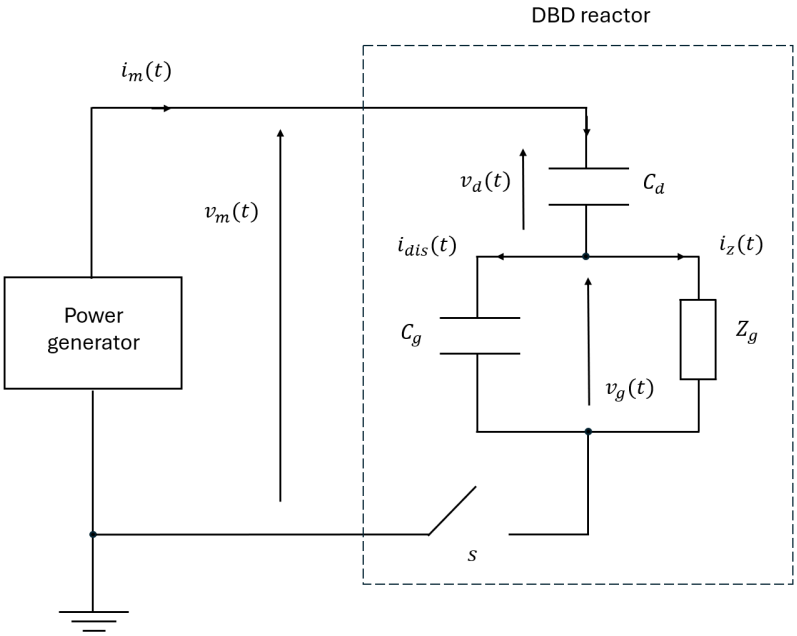

Figure 2.19 – Equivalent electrical circuit of GAPS reactor powered by the micropulsed generator

To develop the analysis further, by substituting the expression for $v_g(t)$ into the equation 2.11, recognizing that the derivative of the measured charge is the total current $\frac{dQ(t)}{dt} = i_m(t)$. This yields the following form of the discharge current:

$$i_z(t) = \left[1 + \frac{C_g}{C_d}\right] i_m(t) - C_g \frac{dv_m(t)}{dt} \tag{2.14}$$

This expression clearly separates the components of the total current into the discharge current $i_z(t)$ and the displacement current component $C_g \frac{dv_m(t)}{dt}$, which is driven by the time rate of change of the applied voltage.

For this analytical method to be effective, accurate values for the dielectric capacitance C_d and the gas gap capacitance C_g must be known. These capacitances directly influence the voltage and current distributions within the system and thus play a critical role in the determination of the discharge current. Without precise knowledge of these parameters, the calculation of $i_z(t)$ becomes unreliable, leading to potential inaccuracies in the power dissipation and other key characteristics of the DBD.

In systems with complex geometries, determining C_d and C_g analytically can be highly challenging due to edge effects, non-uniform electric fields, and variations in dielectric material properties. The equation 2.14 can be rearranged in this form:

$$i_z(t) = \frac{1}{1 - \frac{C_{OFF}}{C_d}} \left[\frac{dQ(t)}{dt} - C_{OFF} \frac{dv_m(t)}{dt} \right] \tag{2.15}$$

where C_{OFF} is the capacitance of the DBD reactor when there is no discharge. In the equation 2.15 the C_g term is no longer explicit and the plasma discharge current can be obtained from measurable quantities. To measure C_{OFF} experimental methods, such as Lissajous figures (Q-V plots), are often employed.

Lissajous Figure Method

Lissajous figures, named after the French physicist Jules Antoine Lissajous, are plots that result from graphing two sinusoidal signals against each other on a Cartesian plane. These figures find extensive applications in the analysis of periodic signals, such as those present in DBDs.

In the context of DBDs, Lissajous figures are used to analyze the charge-voltage ($Q - V$) characteristics of the plasma. The $Q - V$ diagrams, also known as Lissajous figures, are obtained by plotting the instantaneous charge $Q(t)$ across a monitor capacitor, C_m, against the instantaneous voltage applied to the electrodes of the DBD reactor, $v_{DBD}(t)$. This type of representation is useful for diagnosing the electrical properties of DBDs, like C_{OFF}, as well as understanding the discharge behavior during operation.

In the Lissajous method, only a standard voltage probe is needed to measure the voltage across the monitor capacitor, unlike the current-voltage method presented above. Specifically, the basic configuration for measuring a $Q - V$ diagram involves a high-voltage probe to capture the voltage across the DBD electrodes, and a capacitor C_m connected between the reactor and ground to monitor the charge, see Figure 2.20. The charge on the monitor capacitor is given by:

$$Q(t) = C_m \cdot v_c(t), \tag{2.16}$$

where $v_c(t)$ is the voltage across the monitor capacitor.

When dealing with sinusoidal generators, this method results in a characteristic parallelogram shape, see Figure 2.21, where the enclosed area is proportional to the power dissipated by the reactor, $P_{average}$.

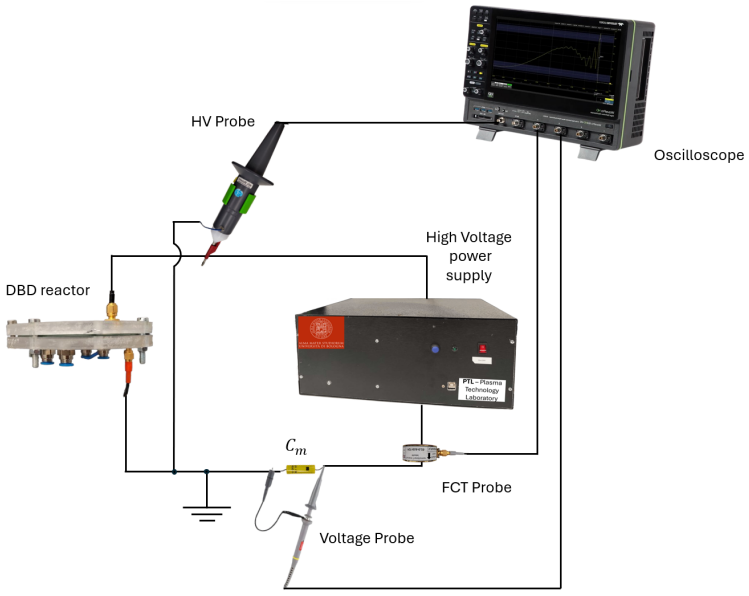

Figure 2.20 – Experimental measurements circuit set up of the DBD reactor for Q-V diagram, with a high-voltage (HV) probe, standard oscilloscope voltage probe, a monitor capacitor C_m.

The ideal parallelogram-shaped $Q - V$ diagram consists of four line segments (AB, BC, CD, and DA), each representing distinct phases of the discharge cycle. In Figure 2.21 the line segments AB and CD correspond to the non-discharging phases (plasma off) of the DBD, where the reactor behaves as two capacitors in series, storing charge from an applied voltage or a plasma discharge. Conversely, segments BC and DA represent the discharging phases (plasma on), where the plasma bridges the gap, reducing the gap voltage v_g and increasing the capacitance effectively seen by the system.

The average power $P_{average}$ can be calculated from the area of the hysteresis loop in the $Q - V$ diagram using the following formula:

$$P = \frac{1}{T} \oint v_m(t)\, dQ(t), \tag{2.17}$$

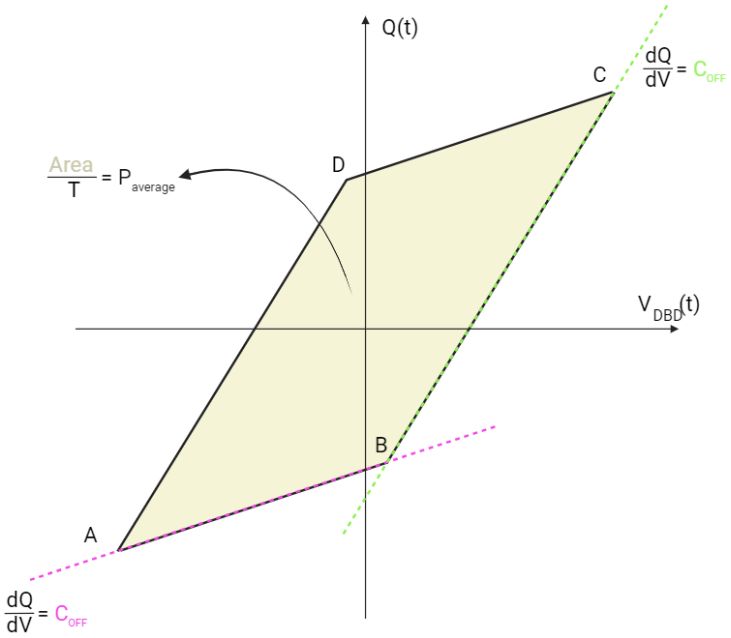

Figure 2.21 – Ideal Q-V diagram with the characteristic parallelogram shape. A-B and C-D are 'plasma off' segments, while B-C and D-A are 'plasma on' segments. The symbols are explained in the text.

where T is the period of the applied voltage.

This integral represents the area enclosed by the $Q - V$ diagram, multiplied by the frequency of the discharge cycle. For accurate power measurements, it is essential to ensure that data acquisition is performed over an exact multiple of the discharge period T, to ensure that reactive power contributions average to zero.

However, when using non-sinusoidal generators, such as the pulsed generator utilized in this project, the resulting Lissajous figures exhibit complex shapes that deviate significantly from the classical parallelogram. This makes interpretation more challenging and can lead to inaccuracies in determining power dissipation. For this reason, the current-voltage method was also employed to provide a broader and more accurate perspective of the reactor's performance. The general principles behind the analysis, however, remain the same for all $Q - V$ diagrams.

In real-world scenarios, deviations from the ideal parallelogram shape can occur due to various factors. The following non-ideal $Q - V$ diagram shapes are commonly observed:

- $Q - V$ **diagrams with slopes less than** C_{diel}**:**
  - *Cause:* Partial surface discharging, where only a fraction of the dielectric area is involved in the discharge.
- **Almond-shaped** $Q - V$ **diagrams:**

  - *Cause:* Gradual expansion of the plasma across the dielectric surface, due to non-uniform breakdown voltages in the gas gap.

- **Elliptical $Q - V$ diagrams:**
  - *Cause:* Continuous plasma current flow due to residual charge carriers during non-discharging phases, or due to measurement circuit issues like parasitic capacitances.

- **Noisy $Q - V$ diagrams:**
  - *Cause:* High-frequency electromagnetic interference from filamentary discharges.

- **Stepped $Q - V$ diagrams:**
  - *Cause:* Discrete microdischarges (streamers) causing sudden jumps in charge transfer.

In Figure 2.22, an example of the *almond shape* for Packed Bed Reactor (PBR) and SDBD is illustrated, extracted from [83], where it is depicted how the gas gap voltage v_g varies during the discharge, unlike the constant voltage observed in the ideal case scenario. This variation results in a non-constant slope in the Q-V diagram, complicating the straightforward calculation of the capacitance C_d. As described in [83]: "In both cases, as the applied voltage increases during the AC cycle, discharging commences at the point where the electric field strength is highest (and the breakdown criterion is first met) and then progressively expands across the electrode surface, as the breakdown criterion is met for increasingly wider gaps. During this plasma expansion, the fractional surface area of the gap capacitance C_{gap} and dielectric capacitance C_{diel}, actively participating in the discharge, increases, leading to an effective capacitance during discharging ζ_{diel} that grows throughout a half-cycle. When the plasma-charged dielectric area reaches its maximum, the gradient of the line will be at its steepest. Similar to the 'ideal' DBD discharges, once the applied voltage $V(t)$ reaches its maximum, no further discharging can occur, as electric field strengths will only begin to decrease. The capacitance is time-dependent, and to determine the value of C_{diel} in these scenarios, one must evaluate the steepest final slope (i.e., ζ_{diel3}), preferably from a Q-V diagram obtained at the highest attainable applied voltage amplitude." As presented in Section 3.1.1, the reactor presented in this study shows an asymmetric almond shape. Consequently, the C_d will be qualitatively derived following the approach used for almond-shaped figures, as described above.

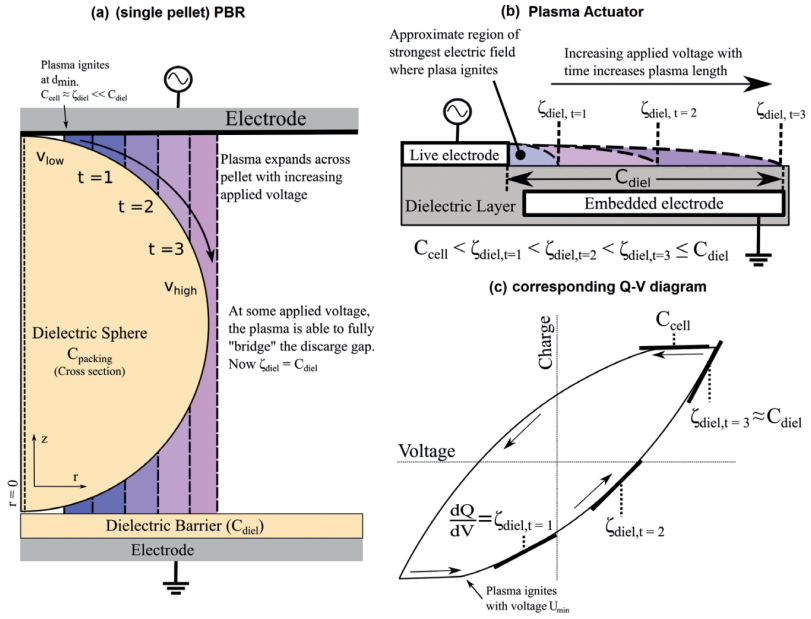

Figure 2.22 – Plasma expansion across (a) a single pellet PBR and (b) a DBD plasma actuator, and (c) its influence on the shape of the Q-V diagram. Source: [83].

Given that any method used for calculating power, when applied to correctly sampled data, should report the active power over a cycle, the results obtained from different methods presented must be comparable in order to assert a reliably calculated power value. As presented in Section 3.1, the average power data obtained using the Lissajous figures and analytical methods show good agreement. Nonetheless, differences have emerged between measurements obtained through these two methods, as expected for pulsed supply SDBD [84].

2.3.4 Chemical Characterization Method

In this section, Fourier Transform Infrared (FTIR) spectroscopy, conducted at the SPC Laboratory of EPFL in Lausanne, is employed to analyze the chemical composition of reactive oxygen and nitrogen species (RONS), such as nitrous oxide (N_2O), nitrogen dioxide (NO_2), and ozone (O_3). This analytical technique is used to characterize the GAPS reactor. Through the application of FTIR spectroscopy, the presence and concentration of RONS are evaluated under various operational conditions of the reactor, as detailed in the physical characterization section. The experimental conditions examined include operating the reactor in static mode and in airflow, using both dry and humid air, at approximately 20% and 70% RH respectively, both maintained at atmospheric pressure and room temperature (22°C). Particularly, the reactor was characterized under an airflow rate of 12.5 LPM to emulate the experiment treatment conditions, see Section 2.2 for more details.

Introduction to Fourier Transform Infrared Spectroscopy

This section offers a concise overview of FTIR spectroscopy, focusing on its fundamental principles rather than comprehensive coverage. For additional information, see [85]. Recognized for its precision in revealing molecular details, FTIR spectroscopy is a critical tool in analyzing the composition and dynamics of chemical species in low-temperature plasma environments [86] [87]. It operates on the principle of infrared radiation interacting with molecules, which allows for the detection of their vibrational and rotational movements. This capability is crucial for identifying chemical species, quantifying their concentrations, and tracking their changes over time. Within the field of low-temperature plasmas, FTIR spectroscopy is crucial for investigating the physical and chemical interactions involved.

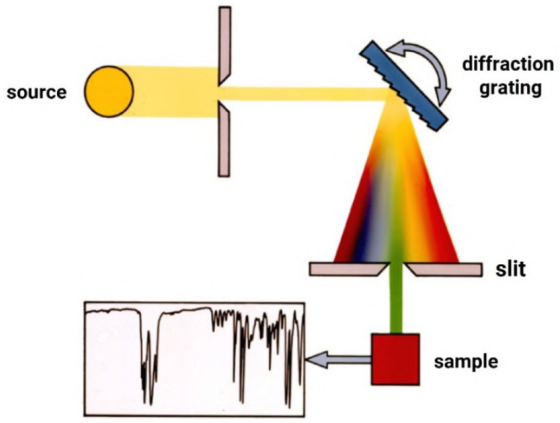

Figure 2.23 – Basic schematics of dispersive IR spectroscopy. Source: [85].

The discovery of infrared light dates back to the early 19th century, when Sir William Herschel identified it as part of the electromagnetic spectrum beyond visible red light. This discovery was pivotal in advancing the field of infrared absorption spectroscopy, which is used to determine molecular structures and concentrations. Infrared radiation excites molecular vibrational states, causing molecules to selectively absorb specific wavelengths. These absorptions alter their electric dipole moments and transition vibrational energy levels from ground to an excited state. The frequency of these absorption peaks is determined by the vibrational energy gap, with the number of observable peaks corresponding to the molecule's vibrational freedoms [85].

Absorption peak intensity reflects changes in the dipole moment and the probability of energy level transitions. Homonuclear diatomic molecules such as O_2, N_2, and Cl_2, which do not exhibit dipole moment changes during vibrations and rotations, are

invisible toFTIR spectroscopy. The spectrum commonly analyzed spans from 4000 to 400 cm^{-1}, capturing the absorption characteristics of most organic and inorganic species. Traditional IR spectroscopy, utilizing a diffraction grating to split the broad-spectrum IR light, is depicted in Figure 2.23. This approach, known as dispersion IR spectroscopy, involves directing a monochromatic IR beam at the sample and measuring its absorbance at that wavelength, repeated across all wavelengths to compile a complete IR spectrum. This method is thorough but slow.

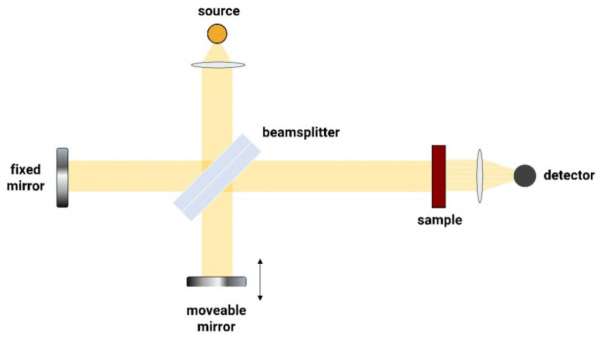

Figure 2.24 – Basic schematics ofFTIR spectroscopy, based on an interferometry system. Source: [86].

In contrast, FTIR spectroscopy employs an interferometer, shown in Figure 2.24, which uses a movable mirror to rapidly cover the entire infrared spectrum. An IR beam is split and directed towards two mirrors, and upon recombination at the beam splitter, the differing path lengths create an interference pattern, capturing various IR wavelengths in the resultant beam. The collected wave pattern, known as an interferogram and illustrated in Figure 2.25 (a), reflects the optical path differences and is transformed into the frequency domain through Fourier transformation, expressed as:

$$f(\nu) = \int_{-\infty}^{\infty} f(t) e^{-i2\pi\nu t} dt \tag{2.18}$$

This interferogram is then converted into an IR absorption spectrum, depicted in Figure 2.25 (b), which plots absorption intensity or percentage transmittance against wavelength or wavenumber. The relationships between transmittance (T_r) and absorbance (A) are defined by:

$$A = \log_{10}\left(\frac{1}{T_r}\right) = -\log_{10} T_r = \log_{10}\left(\frac{I_0}{I}\right) \tag{2.19}$$

where I_0 and I represent the incident and transmitted radiant powers, respectively. Accurate analysis typically includes subtracting background spectra to account for environmental factors, and highlighting peaks that correspond to significant changes in molecular concentration, as illustrated in Figure 2.26.

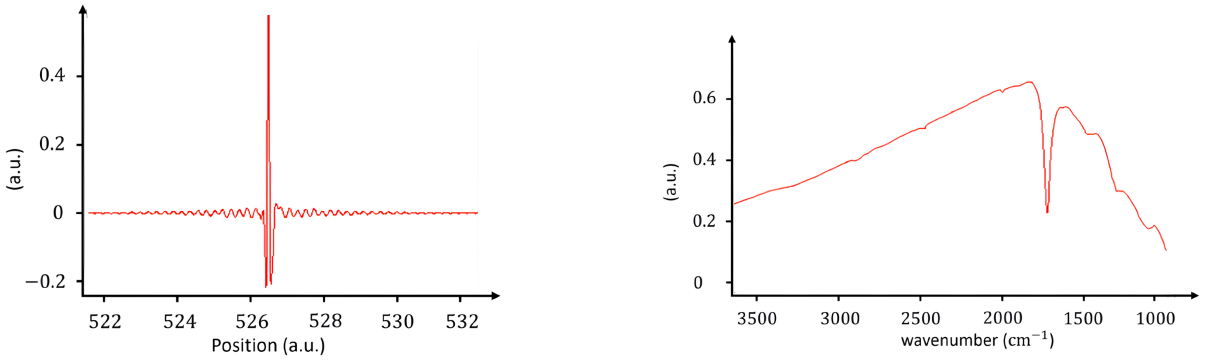

Figure 2.25 – (a) Spatial-domain interferogram of the infrared (IR) signal. (b) Wavenumberdomain absorption spectrum obtained by Fourier-transforming the signal from the spatial domain of the interferogram. Source: [88]

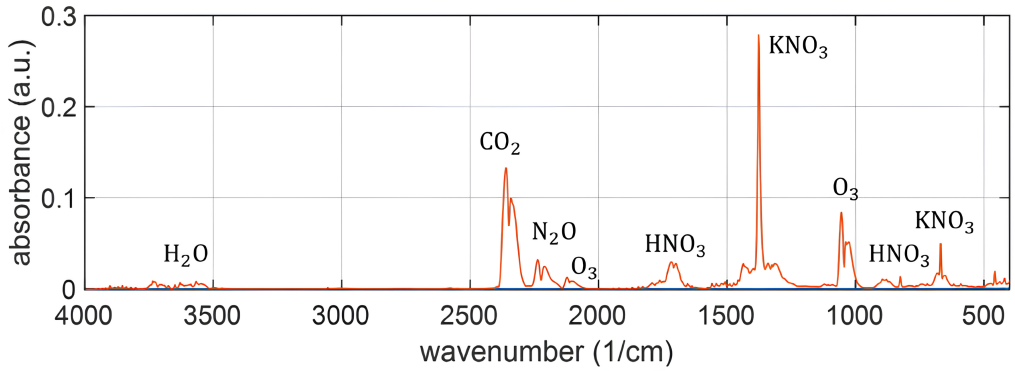

Figure 2.26 – Example of an FTIR spectrum, featuring annotations indicating the corresponding molecule for each distinctive absorbance peak. Source: [88].

Absolute Calibration of FTIR Spectrum

The FTIR spectrum's absolute calibration is conducted via the Beer-Lambert law [89]:

$$I(\nu) = I_0(\nu)e^{-n\sigma_i(\nu)L} \tag{2.20}$$

where $I_0(\nu)$ represents the initial radiant power hitting the sample, and $I(\nu)$ denotes the radiant power that has passed through the sample, both dependent on the frequency ν. The variable n represents the density of the absorbing species, $\sigma(\nu)$ the absorption cross-section per molecule at frequency ν in cm^2/molecule, and L the path length of the absorption in cm.

By rearranging and referring back to the definition of absorbance provided by the FTIR spectrometer in Equation 2.19, we derive:

$$\ln\left(\frac{I(\nu)}{I_0(\nu)}\right) = -n\sigma(\nu)L \tag{2.21}$$

and hence, the absorbance $A(\nu)$ can be calculated as:

$$A(\nu) = \frac{n\sigma(\nu)L}{\ln 10} \tag{2.22}$$

By measuring the absorbance spectrum $A(\nu)$ with the FTIR spectrometer, one can determine the density n_i in molecules/cm^3:

$$n = \frac{A(\nu)\ln 10}{\sigma_i(\nu)L} \tag{2.23}$$

To convert this to parts per million (ppm), assuming $n = n_0 n_i \times 10^{-6}$, where n_i is the density of the species i in ppm and n_0 is the density of the gas, the concentration of a specific molecule can be expressed as:

$$n_i = \frac{A(\nu)\ln 10 \times 10^{12}}{\sigma_i(\nu)L \times n_0} \tag{2.24}$$

where $A(\nu) = \ln\left(\frac{I_0}{I}\right)$ denotes the absorbance at frequency ν, and $\sigma_i(\nu)$ is the absorption cross-section of the species i at ν in cm^2/molecule. The final term $10^{12}/n$ is a necessary conversion factor to switch from molecules/cm^3 to ppm.

In-Situ FTIR Spectroscopic Analysis

Unlike traditional approaches where FTIR spectroscopy is applied post-process to the gas exhausted from plasma sources [90], this work adopts an in-situ method as described in the referenced thesis [91, 92]. The primary advantage of in-situ FTIR spectroscopy is its ability to capture molecular compositions immediately at their point of origin, which

prevents alterations from interactions with surfaces or during transit to a detection system, thereby eliminating modifications by secondary reactions [91].

The Bruker Vertex 80v spectrometer is utilized for the in-situ measurements. The setup focuses the IR beam inside the sample compartment (see point *B* in Figure 2.27), targeting a focal point approximately 8 mm in diameter, with the beam expanding to about 2.5 cm at the aperture of the flap windows. This configuration does not affect the measurements of GAPS, as depicted in Figure 3.20.

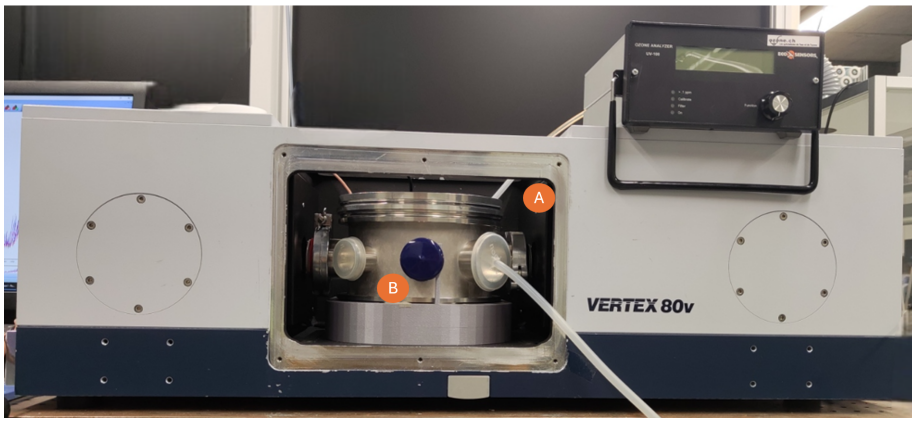

(a) Complete setup of the FTIR spectrometer with ozone analyzer(on the top-right). A: sample compartment. B: bio-plasma reactor.

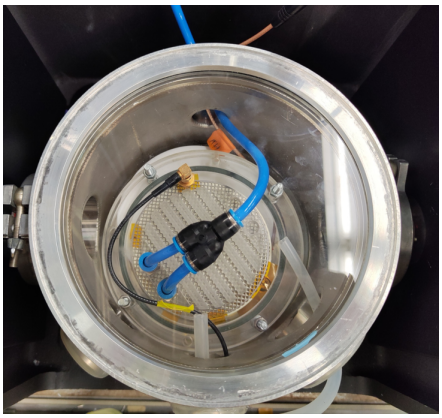

(b) Close-up view of the bio-plasma reactor interior with GAPS inside.

Figure 2.27 – The images show detailed internal and external views of the FTIR spectrometer setup, highlighting its components used for advanced spectroscopic analysis.

The bio-plasma reactor, in which GAPS is placed for the measurements, is strategically placed within the spectrometer's sample compartment, with two flanges facilitating the entry and exit of the IR beam through designated IR windows, which align with the optical pathway. These flanges manage both the inflow-outflow of gases as supporting a static operation mode without any gas circulation or exhaust. A 3D-printed support

ensures the reactor's stability and precise alignment, optimizing the beam's height relative to the reactor windows.

To hermetically seal the bio-plasma reactor, two windows with a diameter of 30 mm are positioned along the line-of-sight of the IR beam. Custom-designed 3D adapters have been manufactured to match the flanges of the bio-plasma reactor, ensuring a sealed fit for the windows. Conversely, the optics bench of the vacuum FTIR spectrometer is sealed using 49.5 mm diameter windows, referred to as "flap" windows, on each side of the sample compartment [88]. The window materials consist of potassium bromide (KBr), known for its favorable infrared transmission characteristics within the range sampled by the FTIR spectrometer. However, KBr is highly susceptible to humidity, leading to surface deterioration and reducing IR transmittance. Additionally, the reaction between reactive species produced by the plasma and the KBr window surface results in the formation of KNO3, a compound that is deposited on the window surface, causing an escalating peak during plasma operation at 1352 cm^{-1}, that obscures other molecular peaks within the same wavelength range. However, KBr was chosen for the bio-plasma reactor windows due to its good transmission characteristics and our understanding of the peaks resulting from its interaction with plasma.

Table 2.2 – Parameters used for FTIR spectroscopy measurements.

Parameter	**Value**
Resolution	4 cm^{-1}
Spectral range	400 to 4000 cm^{-1}
Number of scans	16
Detector	RT-DLaTGS
Aperture	8 mm
Scanner velocity	10 kHz

Due to the integration of electrical connections and gas tubing within the bio-plasma reactor's configuration, the sample compartment was not fully enclosed. As a result, the IR beam passed through a small segment of the ambient air, roughly 2 cm, external to the reactor. This exposure contributed to observable fluctuations in the concentrations of CO_2 and H_2O. These variances render any conclusions about these molecules in this experimental setup unreliable, and they have been excluded from further consideration. The Bruker Vertex 80v spectrometer was configured with a specific array of settings to align with the goals of our experiments. The essential parameters were carefully

chosen and are comprehensively listed in Table 2.2 to minimize the duration of each acquisition cycle to 16 seconds, thereby maintaining the integrity of the spectral data without sacrificing acquisition speed.

Each FTIR spectroscopy measurement is conducted over 16 seconds, comprising 16 individual scans. This setup allows measurements to be taken at regular 30-second intervals. After each acquisition phase, the gathered spectra are meticulously analyzed to correct any baseline drift, which is a frequent issue in FTIR spectroscopy caused by mechanical vibrations along the optical path [93].

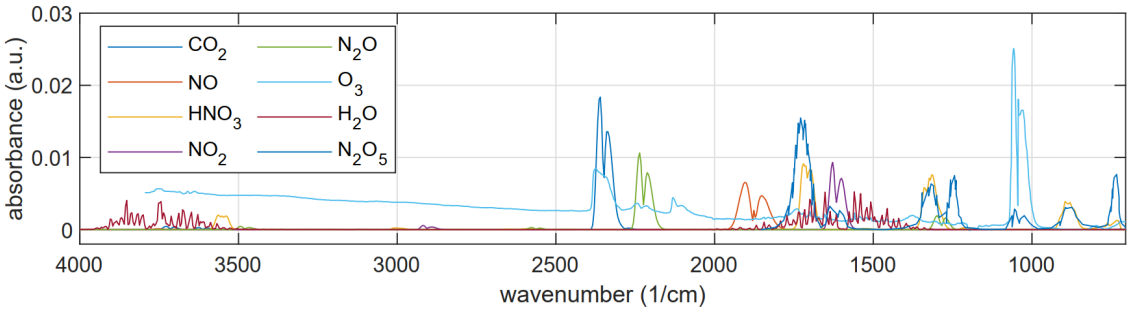

Figure 2.28 – FTIR spectra of specific molecules expressed in arbitrary units, namely O_3, NO, NO_2, N_2O, N_2O_5, HNO_3, CO_2, and H_2O. Source: [88].

After the correction phase, these spectra are then methodically compared to reference spectra of certain gases such as O_3, NO, CO, NO_2, N_2O, N_2O_5, HNO_3, CO_2, and H_2O, detailed in Figure 2.28.These reference spectra are sourced from either Bruker or Hitran (High Resolution Transmission) databases [94], , which help in accurately identifying the peaks corresponding to the various molecular species present in the FTIR measurements.

Calibration of O_3, N_2O, NO_2 and HNO_3

Once the molecular peaks in the FTIR spectra have been identified and associated with specific chemicals, the calibration of the absorption spectrum proceeds according to Equation 2.24. Given that these experiments operate under standard atmospheric conditions at room temperature, the gas density is set at $n_0 = 2.5 \times 10^{25}$ molecules/m^3. With an assumption that the molecular species disperse throughout the entire bio-plasma reactor in less than 16 seconds—the time required for a single spectral acquisition—and considering a path length (L) of 23 cm, which is the distance between the windows of the reactor, this setup allows for calculating the average concentration along the infrared beam's path.

Precise calibration is achievable for the reactive species detected in the FTIR analysis, such as O_3, N_2O, NO_2, and HNO_3, owing to the availability of their absorption cross-sections provided by the HITRAN database [94]. The HITRAN molecular spectroscopic database compiles a wide range of spectral parameters crucial for the simulation and analysis of light transmission and emission through gaseous media, with a particular focus on planetary atmospheres. Given that our experimental conditions are similar to those found at Earth's surface, HITRAN is exceptionally suited for accurately simulating the absorption cross-sections of these specific molecules. Table 2.3 outlines the detailed parameters used to derive the absorption cross-sections for O_3, N_2O, NO_2, and HNO_3, presented in Figure 2.29.

Table 2.3 – Parameters used for O_3, N_2O, NO_2 and HNO_3 absorption cross-section simulation on HITRAN.

Parameter	**Value**
Isotopologues	all
Spectral range	500 to 4000 cm^{-1}
Cut-off intensity	1.0e-28 cm/molecule
Temperature	296 K
Pressure	1 atm
Line profile	Voigt
W	50 halfwidths
WN_{step}	0.00902 (default)
Device function	Gaussian
Resolution	0.1 cm^{-1}
AW	< 50 (default)

To calibrate the signal, a wavelength band has been defined for the three different molecules, corresponding to the highest peak of the absorption cross-section

To calibrate the signal further, wavelength bands have been defined for four molecules corresponding to the highest peak of their respective absorption cross-section, as detailed in Table 2.4. The corresponding FTIR absorbance spectra for these molecules, integrated over their respective wavenumber ranges, are depicted in Figure 2.30.

The primary absorption peaks of NO_2 and HNO_3 at 1570–1650 cm^{-1} and 1670–1740 cm^{-1}, respectively, are partially overlapped by the water absorption peaks. Consequently, for the calibration process of NO_2, the wavenumber range 1592–1600 cm^{-1} is

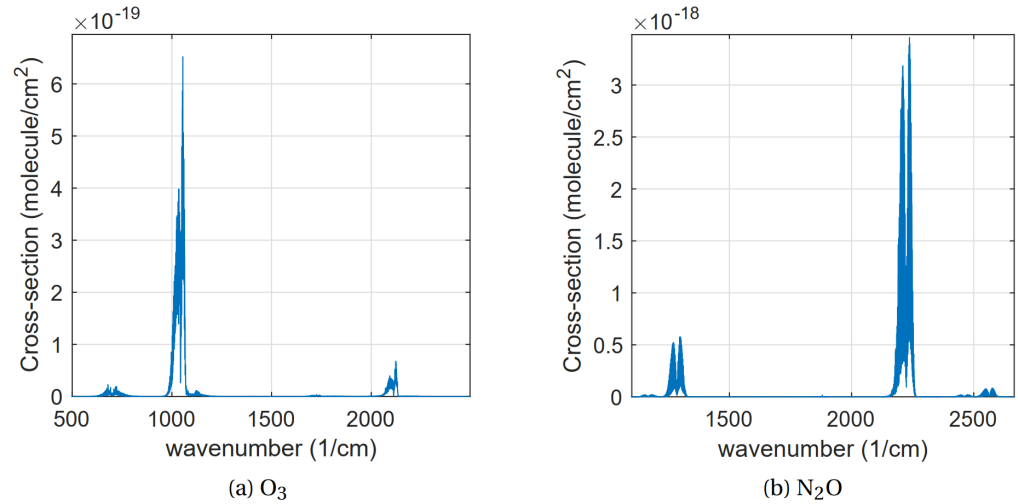

(a) O_3 and N_2O

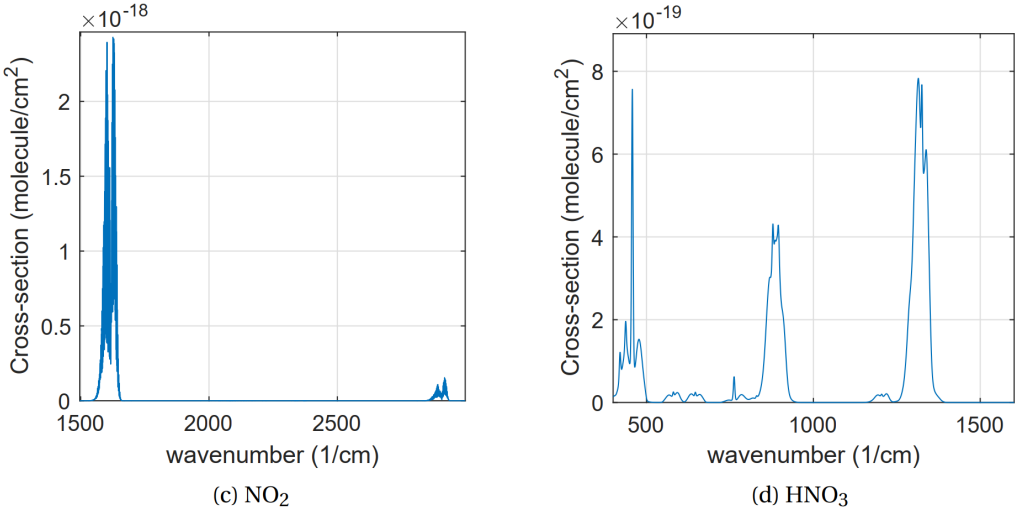

(b) NO_2 and HNO_3

Figure 2.29 – Absorption cross-section in cm^2/molecule of (a) O_3, (b) N_2O, (c) NO_2, and (d) HNO_3, simulated with HITRAN, using the parameters in Table 2.3.

Table 2.4 – Wavenumber range used for O_3, N_2O, NO_2, and HNO_3 calibration.

Gas	**Wavenumber Range (cm^{-1})**
O_3	1010 - 1065
N_2O	2194 - 2250
NO_2	1592 - 1600
HNO_3	850 - 920

selected to avoid the H_2O absorption peaks, since in this range the absorption cross section of H_2O is null. To calibrate HNO_3, instead, a secondary absorption peak at 850 – 920 cm^{-1} is used. Finally, the integrated values are applied to Equation 2.24.

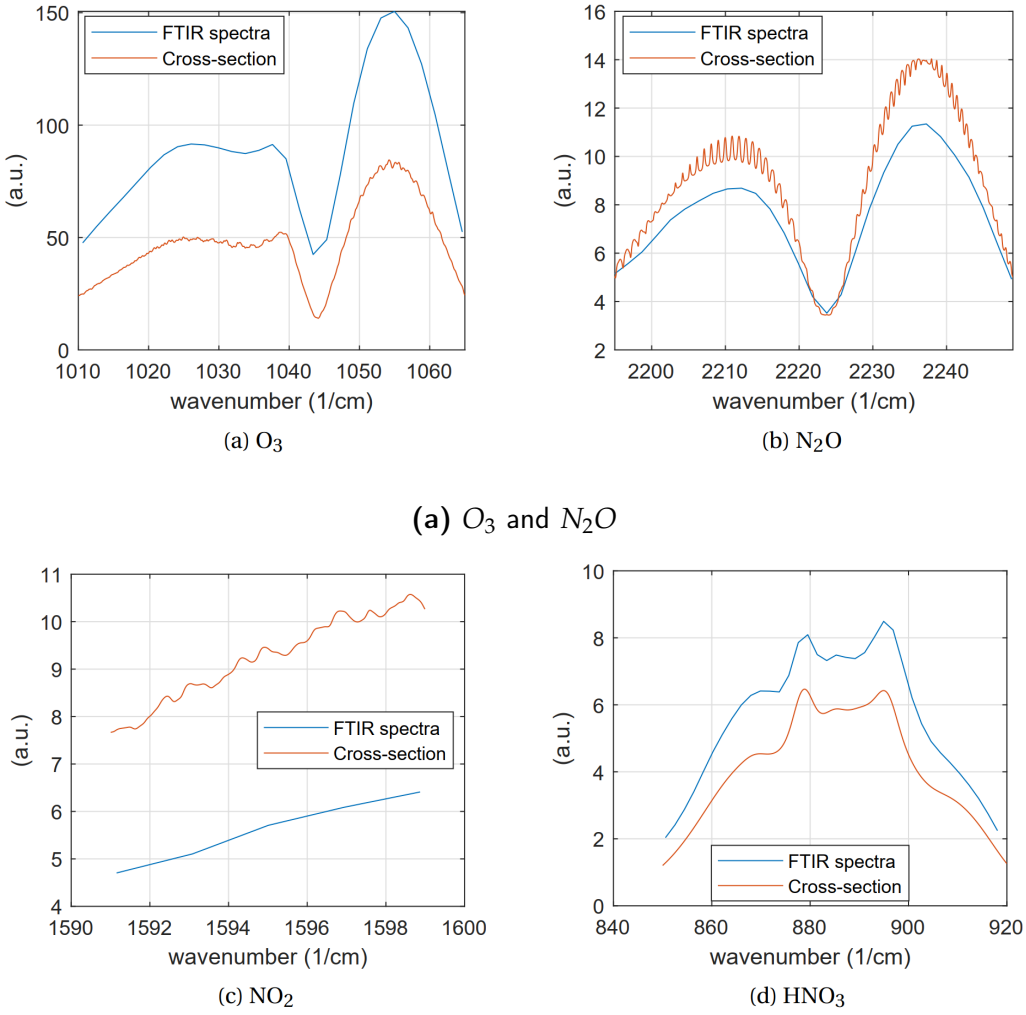

(a) O_3 and N_2O

(b) NO_2 and HNO_3

Figure 2.30 – Absorption cross-section and example of measurement of FTIR absorbance spectra, for the wavelength range over which the signals are integrated for (a) O_3, (b) N_2O, (c) NO_2 and (d) HNO_3.

The calibration and measurements detailed in this chapter have been important for assessing the reactor's performance under different operational scenarios: in static mode and with a gas flow rate of 12.5 LPM, to mirror the environmental settings of the biological experiments. The results are presented and discussed in Section 3.2.

Chapter 3

Physical, Chemical, and Biological Characterization of the CAP Reactor

This chapter presents the results obtained from the experimental setup outlined in Chapter 2, encompassing the electrical, chemical, and biological characterization of the Dielectric Barrier Discharge (DBD) reactor, named **GAPS - Grid-like Air Plasma Sanitizer,** used for bioaerosols treatment. The chapter is divided into three sections, each providing a comprehensive evaluation of the reactor's performance under various operating conditions.

Section 3.1 begins with the physical and electrical characterization results of GAPS reactor. This section includes electrical measurements to quantify the power delivered to the system, establishing a baseline for the reactor's operational stability and efficiency. Additionally, Computational Fluid Dynamics (CFD) simulations are reported to understand the airflow patterns within the reactor, providing insights into the distribution and behavior of bioaerosol during treatment and ensuring homogeneous bioaerosol distribution and efficient interaction with the plasma. The section finishes with the chemical characterization of the plasma discharge, focusing on the identification of key reactive species generated during treatment. Using Fourier-transform infrared (FTIR) spectroscopy, the influence of different operational parameters on the chemical composition of the plasma is analyzed, highlighting the formation of reactive oxygen and nitrogen species (RONS) critical for bioaerosol inactivation.

Finally, Section 3.3 evaluates the biological efficacy of GAPS against *Escherichia coli* bioaerosol. The results obtained through microbial viability assays demonstrate the impact of plasma treatment on bacterial reduction, validating the effectiveness of the developed system.

3.1 Physical Characterization Results

This section focuses on a comprehensive physical characterization of the DBD reactor, aiming to evaluate its performance from multiple perspectives. The analysis begins with an electrical characterization to determine the reactor's power consumption and energy efficiency. Understanding the electrical properties is crucial, as they influence both the plasma discharge's stability and the treatment process's overall energy efficiency. Following the electrical analysis, a Computational Fluid Dynamics (CFD) study is presented to investigate the flow dynamics inside the reactor. This analysis is essential to ensure a homogeneous interaction between the treated airflow and the plasma discharge. A uniform flow distribution promotes consistent exposure of bioaerosols to the active plasma region, thereby enhancing the overall effectiveness of the treatment. Finally, the results of the FTIR spectroscopy are presented to complete the reactor characterization under a chemical point of view.

3.1.1 Power Measurement Results

Q-V Method Results

In this section, results obtained from Lissajous figures of GAPS under various operational conditions are presented. A monitor capacitor C_m of 10 nF was connected in series with GAPS , as shown in Figure 2.20, to capture the voltage v_c. This capacitor value was chosen to balance between maintaining a high enough reactor voltage to initiate the discharge and minimizing noise in the capacitor signal. By plotting charge $Q(t)$ against $v_{DBD}(t)$, the Lissajous figures are obtained for different operative conditions, shown in Figure 3.1. The normalized $v_{DBD}(t)$ and v_c waveform are shown in Figure 3.2.

The different operative conditions for DBD reactor average power measurement are:

- Reactor under static conditions, i.e., in the absence of airflow.
- Reactor with humid airflow at 12.5 LPM to replicate the exact conditions of biological experiments.
- Reactor under static conditions but after the flow was turned off, specifically after 30, 60, 90, 120, and 160 seconds.

Each experiment was conducted with three replicates to obtain average results and corresponding error bars. As depicted in Figure 3.3, the initial static condition shows low power (0.11 W) due to the discharge only affecting about 10% of the available area

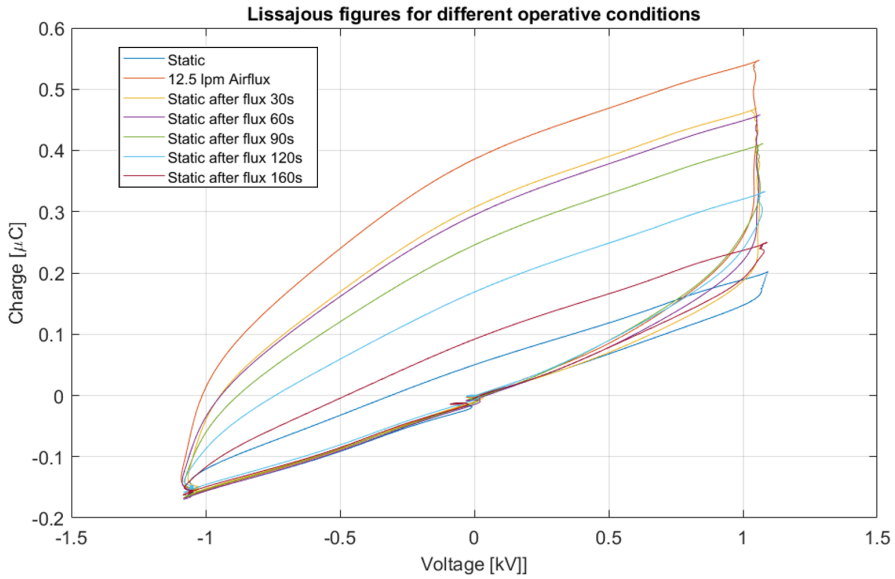

Figure 3.1 – Lissajous Figures for Different Operative Conditions: This graph showcases the dynamic behavior of GAPS under various flow and static conditions by plotting charge μC against voltage (kV). Each curve represents a unique condition, illustrating how the plasma discharge characteristics change over time and with different conditions. The orange line represents the reactor under a flow of 12.5 LPM humid air, showing significantly higher charge accumulation compared to the static conditions, indicated by the blue line. Subsequent green, red, purple, teal and brown lines demonstrate the gradual decrease in charge as the reactor remains static after the airflow is stopped precisely at 30s, 60s, 90s, 120s, and 160s.

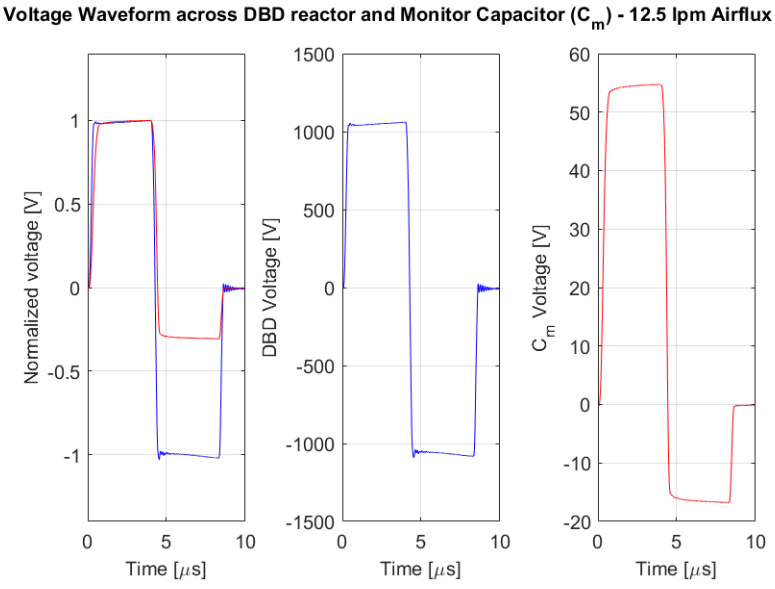

Figure 3.2 – Voltage waveform across GAPS, v_{DBD}, and monitor capacitor, (C_m), under 12.5 LPM airflux condition. The left panel shows the normalized voltage.

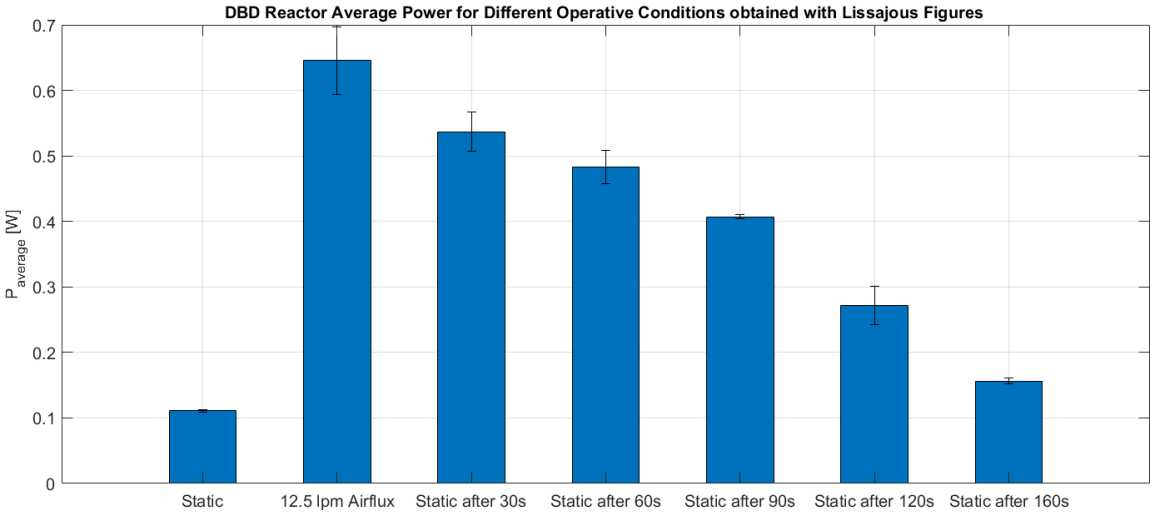

Figure 3.3 – DBD reactor average power, $P_{average}$ for different operative conditions obtained with Lissajous figures. The tallest bar, representing the reactor under a 12.5 LPM air flux condition, shows significantly higher power output (approx. 0.65 W), indicating enhanced plasma activity due to increased airflow. The initial static condition yields the lowest power (approx. 0.15 W). Subsequent bars show power outputs after the air flux is ceased for 30s, 60s, 90s, 120s, and 160s.

(visible plasma), focusing on the sharp corners of the exposed electrode (see Figure 3.4 (d)). Introducing the flow enhances the plasma, igniting over the entire available area as shown in Figure 3.4 (b), reaching 0.65 W. When the airflow is stopped, the plasma contracts back to its initial static condition, as indicated by the decreasing average power values and corresponding plasma discharge images.

The slope of the Lissajous figures (C_{OFF}), observed in the absence of discharge, corresponds with the experimentally measured capacitance value of the DBD reactor, which is $C_{DBD} = 140$ pF, measured using an Aisita AS250 impedence meter. This capacitance value has also been replicated through simulations conducted using the *FEMM* software, which employs an electrostatic model of the DBD reactor, detailed in the subsequent sub-section. The dielectric capacitance C_d was measured at the saturation point under different operational conditions, as explained in sub-section 2.3.3, and the results are reported in Table 3.1. In this study, the Lissajous figures exhibit non-ideal shapes, with a distinctive asymmetric almond-like form. This asymmetry arises from higher charge storage during the positive voltage period, a characteristic influenced by the specific power supply used. Despite its asymmetry, the overall behavior resembles that of an almond-shaped figure, hence the C_d was measured as explained above. The obtained C_d values were subsequently used for calculations in the analytical model.

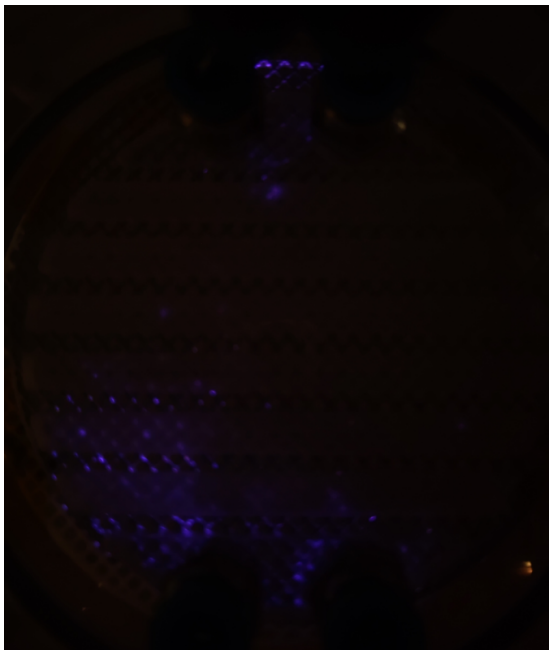

(a) static

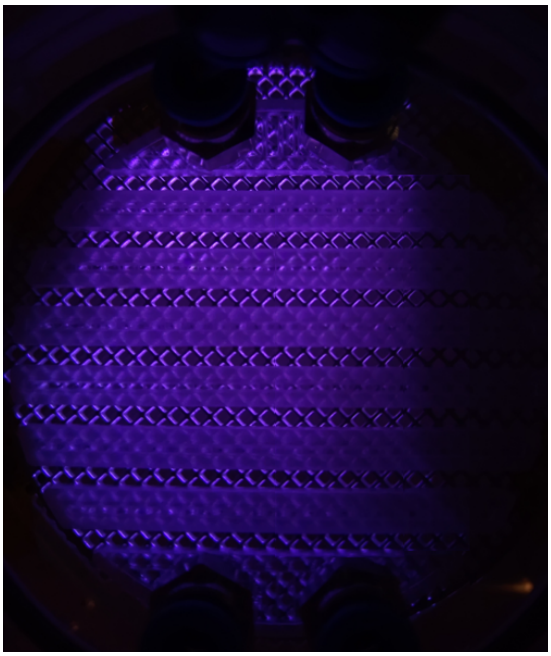

(b) 12.5 LPM humid airflux

(c) static after 60 s

(d) static after 120 s

Figure 3.4 – Sequential visualization of plasma behavior in GAPS under different operative conditions. (a) static, (b) 12.5 LPM humid airflux, (c) static after 60 seconds, (d) static after 120 seconds. Photos are taken with ISO 800 and an exposure time of 20 seconds.

Analytical Model Results

This section presents the average power results obtained with the electrical equivalent circuit method, with replicates to provide average values and respective error bars.

Table 3.1 – Dielectric capacitance C_d of GAPS under different operative conditions.

Operative Condition	C_d [pF]
Static	153
12.5 LPM airflux	420
Static after 30s	327
Static after 60s	300
Static after 90s	250
Static after 120s	200
Static after 160s	180

A graph comparing the Lissajous results and the analytical method is presented to demonstrate the consistency of the results obtained by both methods.

Figure 3.5 shows the results for the average power in different operative conditions, the same used for Lissajous figure measures. At first, one can directly see that the distribution for the different cases compared to the one calculated with Lissajous are in good agreement. For simplicity of analysis, both the bar graphs are reported in one single diagram to show the consistency of the results better. See Figure 3.6. Even if the power should be the same, since the average power over one entire period should be the sole active power, experimental error leads to different results. The differences can be attributed to the procedure of numerical differentiation (sensitive to random noise) and integration (sensitive to small systematic errors). Nonetheless, we can say that in the fluxed case the trend is more similar and comparable, also thanks to the stability of the discharge itself, which we can therefore define around 0.6 W.

The analytical method allowed investigation into the actual power discharge distribution, due to the calculated value of discharge current, i_z (see 2.3.3) and how the energy is transferred to the discharge. The results are shown in Figure 3.7 and 3.8 for the static and dynamic case respectively. A detailed analysis of the electrical discharge phenomena can be done. The differences between positive and negative pulses, the role of charge accumulation, and the resulting electrostatic implications are discussed.

Figure (a) shows the measured voltage and current where three peaks are depicted. In reality, only two discharges happen during one period, one positive and one negative, both initiating at around $\pm 400V$. This figure highlights that both discharges initiate at approximately this voltage level and this observation will be further substantiated by the electrostatic analysis conducted using the FEMM software, which will be discussed in the subsequent section. The lack of a discharge in the last microseconds of the voltage waveform means that the initiation requires an inversion of the electric field, in fact

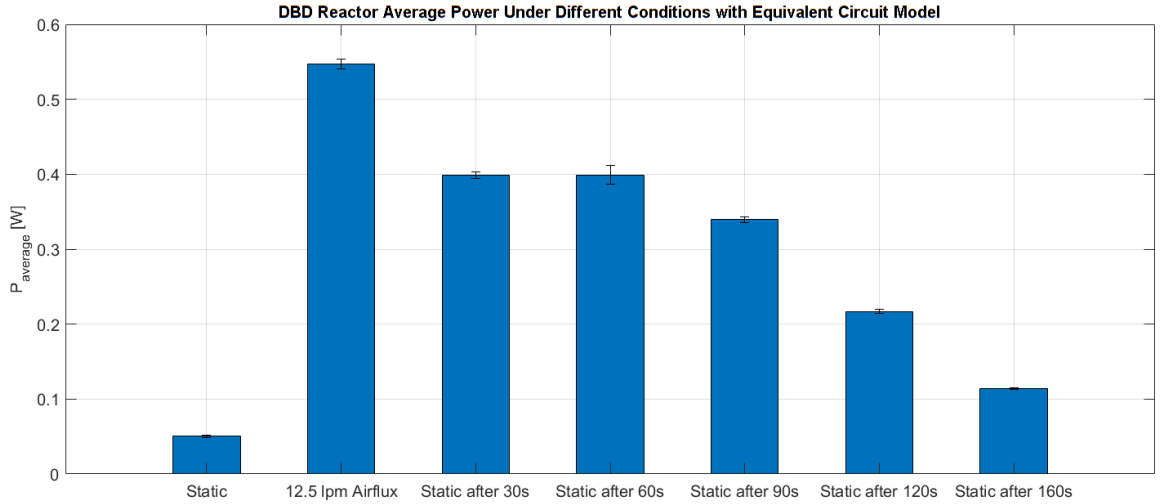

Figure 3.5 – DBD reactor average power, $P_{average}$ for different operative conditions obtained with the equivalent electrical circuit. The tallest bar, representing the reactor under a 12.5 LPM air flux condition, shows significantly higher power output (approx. 0.55 W), indicating enhanced plasma activity due to increased airflow. The initial static condition yields the lowest power (approx. 0.1 W). Subsequent bars show power outputs after the air flux is ceased for 30s, 60s, 90s, 120s, and 160s.

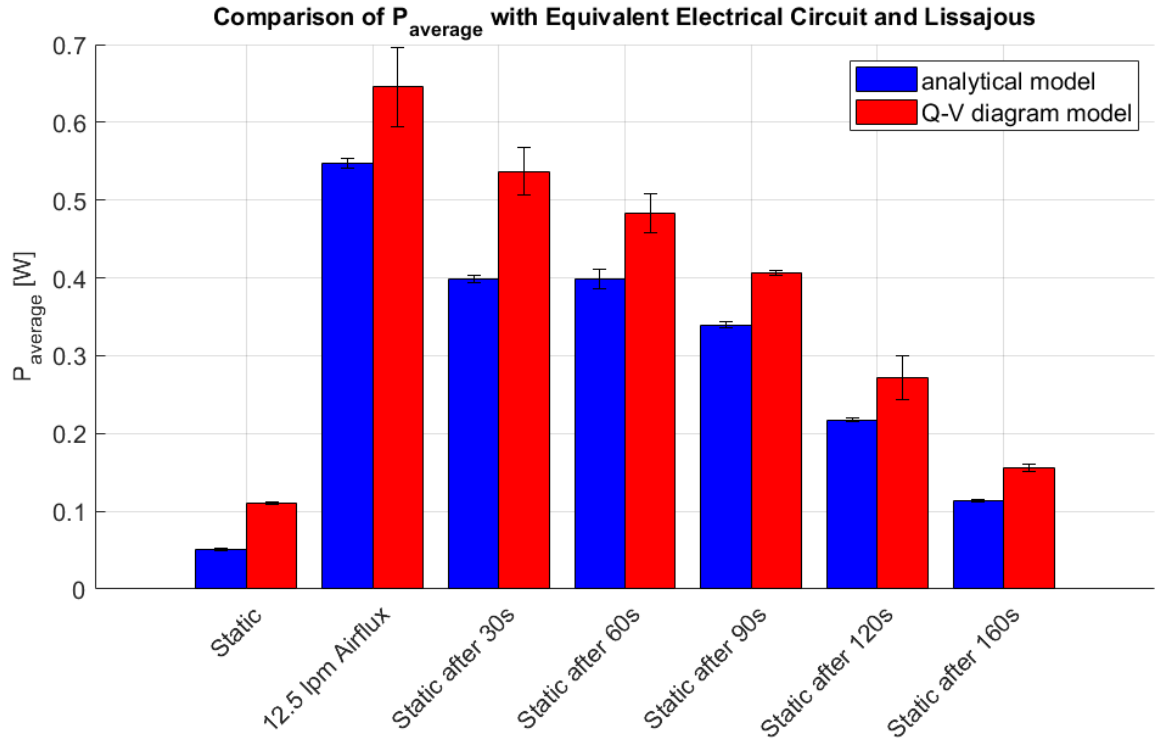

Figure 3.6 – DBD reactor average power, $P_{average}$, obtained with equivalent electrical circuit analytical method and with Lissajous figure.

when transitioning from +1.2 kV to 0 V or from -1.2 kV to 0 V no discharge happen. although the second discharge shows an apparent double ΔV. This effect is due to residual charges that, while not fundamental to discharge initiation (around 400V), screen the field along segments with decreasing voltage. This can be seen by analysing

the integral energy associated with the measured current peaks, where the energy delivered is the same in both discharges, in fact, the ΔV is the same for both. Figure (d) shows that only two discharge pulses happen and also that the energy transferred during both the positive and negative pulses is equivalent. Although the peaks differ, Figure (b), the energy remains consistent across pulses. This constancy is due to the longer duration of the first pulse, which compensates for its lower peak in comparison to the second pulse (c). This behavior can be explained by the fact that with the voltage inverted the resulting electric field is enhanced by the residual charges, which lowers the ignition threshold and enables a new discharge with potentially greater energy. This occurs because the strengthened field can accelerate charged particles more rapidly and intensely, making the subsequent discharge more effective in generating plasma. Those charges are the same that shield the electric field since the voltage is inverted again, thus no discharge happen during voltage decrease.

A more comprehensive analysis of the phenomenon can be conducted by comparing the voltage and current with the Q-V diagram (Figure 3.9). The Lissajous figures illustrate the charge distribution during both positive and negative pulses, showing significantly more charge deposited during the positive pulse. This behavior is attributable to the enhancement effect, i.e., the increase in the electric field caused by positive charges accumulated during the first discharge. Conversely, the second discharge involves negative residual charges that are more mobile, resulting in reduced accumulation and influence on the local electric field during the plateau interval of the applied voltage. The residual charges deposited during each pulse, while not directly influencing discharge initiation (see FEMM results), modify the electric field behavior along decreasing-voltage segments. This screening forced the voltage to be inverted before any discharge to happen.

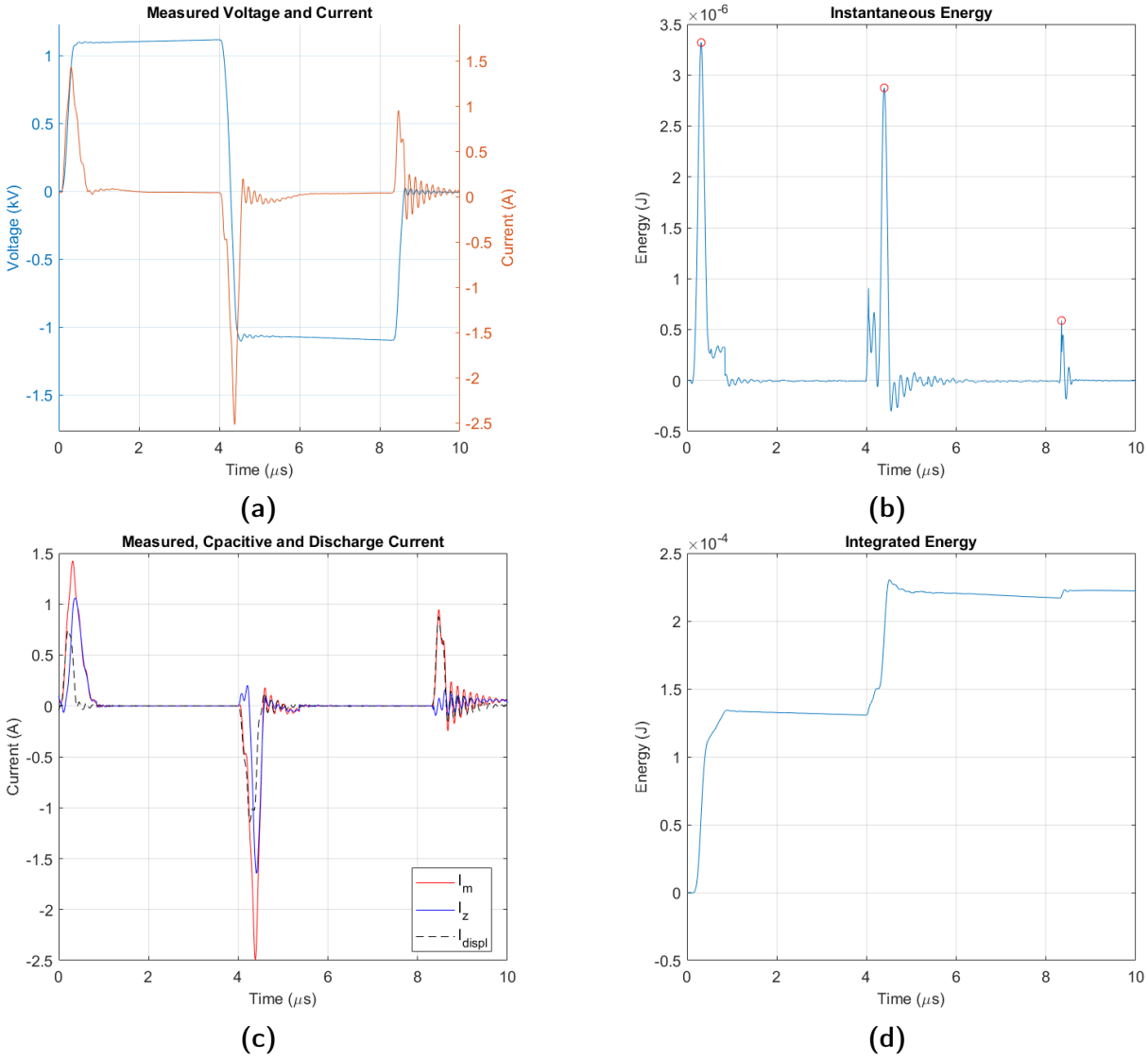

Figure 3.7 – Overview of electrical variables for static discharge condition. (a) measured voltage and current. (b) instantaneous energy. measured, displacement and discharge current. (d) integrated energy.

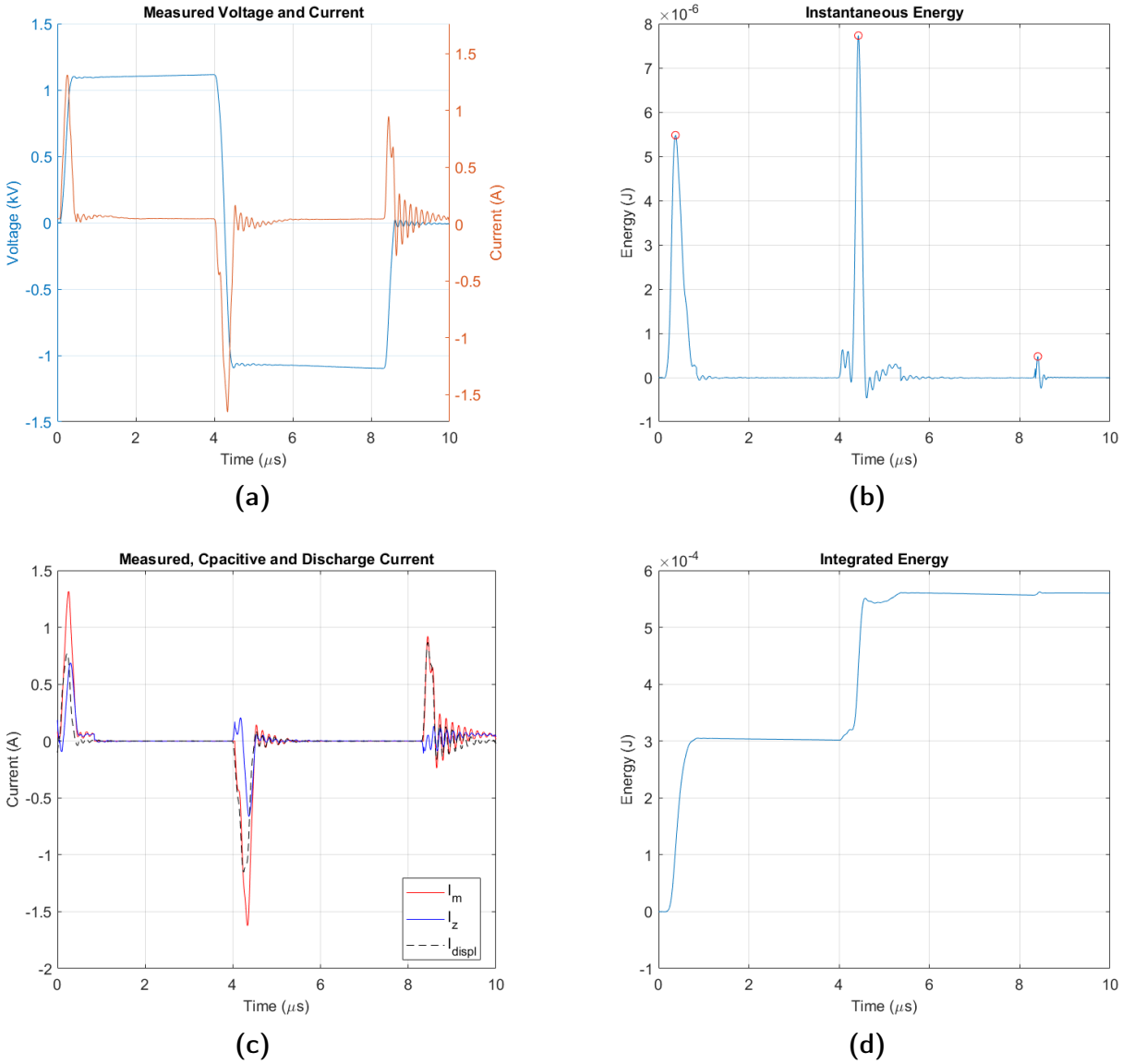

Figure 3.8 – Overview of electrical variables for fluxed discharge condition. (a) measured voltage and current. (b) instantaneous energy. measured, displacement and discharge current. (d) integrated energy.

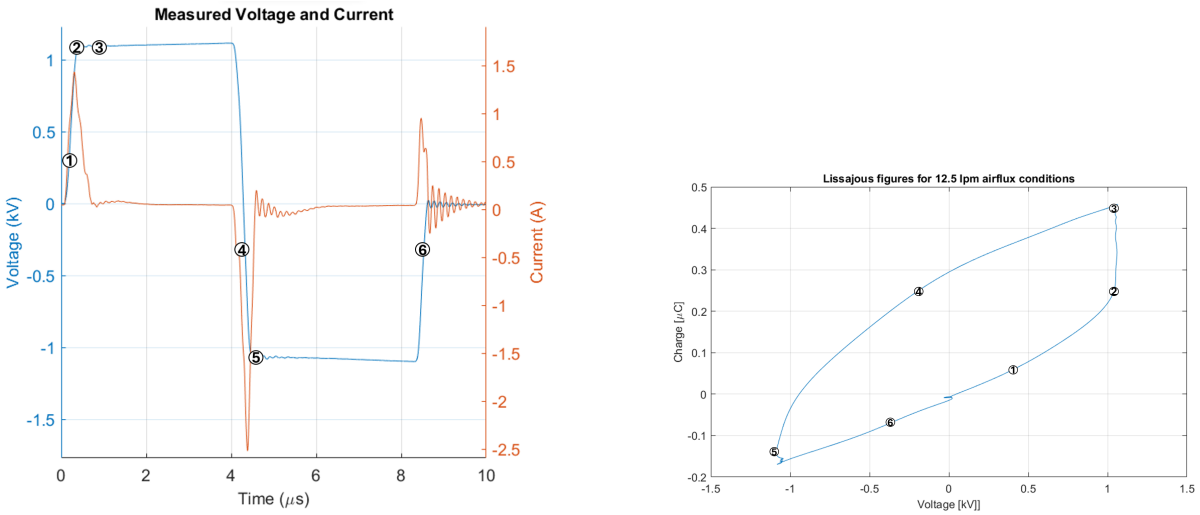

(a) (b)

Figure 3.9 – Measured voltage and current (a) with marked ignition points and the relative Lissajous figure (b) for a comprehensive comparison.

In Figure 3.9 some point is marked for a better understanding. Point (1) represents the first ignition at around 400V. Point (2) represents the highest voltage value, positive peak, where the positive charge start to accumulate and lasts till point (3). After the second ignition (4) it is notable as there is no symmetrical charge accumulation and the discharge is faster and shorter. Point (6) denote the -400V voltage point that is not enough to initiate a discharge due to the charge shield, as explained above.

FEMM Model Results

FEMM (Finite Element Method Magnetics) is a popular software package designed to solve electromagnetic problems using the finite element method. In this research, FEMM has been employed to perform electrostatic simulations, specifically focusing on the dual-cell configuration of the Dielectric Barrier Discharge (DBD) reactor. This application of FEMM allows for the detailed analysis and visualization of electric field distributions and potential gradients. Furthermore, this software can be effectively utilized to qualitatively assess the capacitance of the DBD reactor.

As depicted in Figure 3.11, the 2D electrostatic model includes one electrode encapsulated with Rilsan dielectric material (depicted as an embedded square) and one exposed electrode. The exposed electrode is presented in two distinct configurations: perfectly aligned with the coated electrode and displaced. These configurations are intended to represent two realistic scenarios concerning the arrangement of grid-like electrodes: in one instance, they are perfectly aligned, while in the other, they are slightly misaligned. Such misalignment mirrors actual conditions and can be attributed to mechanical factors associated with the assembly of the reactor itself (due to electrical connections that do not allow perfect alignment). This statement is substantiated by the fact that Figure 3.10 provides a detailed zoomed-in view of the plasma discharge and the distribution of the electrodes. The dielectric layer is uniformly applied, extending 200 μm around the coated electrode. The mesh is finer alongside the area more interested by the electric field.

Capacitance measurements were performed using the formula for the energy stored in a capacitor, given by:

$$W_c = \frac{1}{2} C V^2$$

Rearranging this formula provides the capacitance:

$$C = \frac{2W_c}{V^2}$$

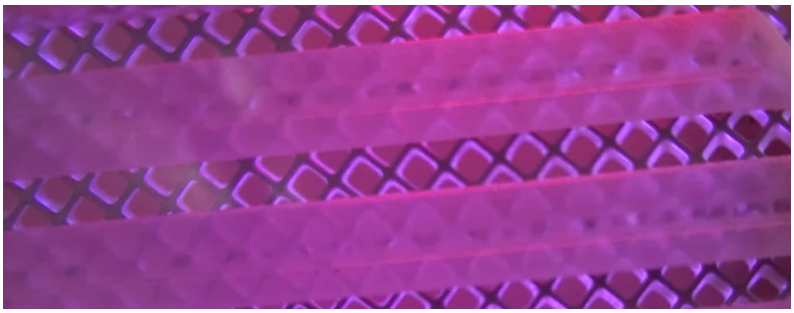

Figure 3.10 – Detailed zoomed-in view of the plasma discharge and the mutual position of the grid-like electrodes.

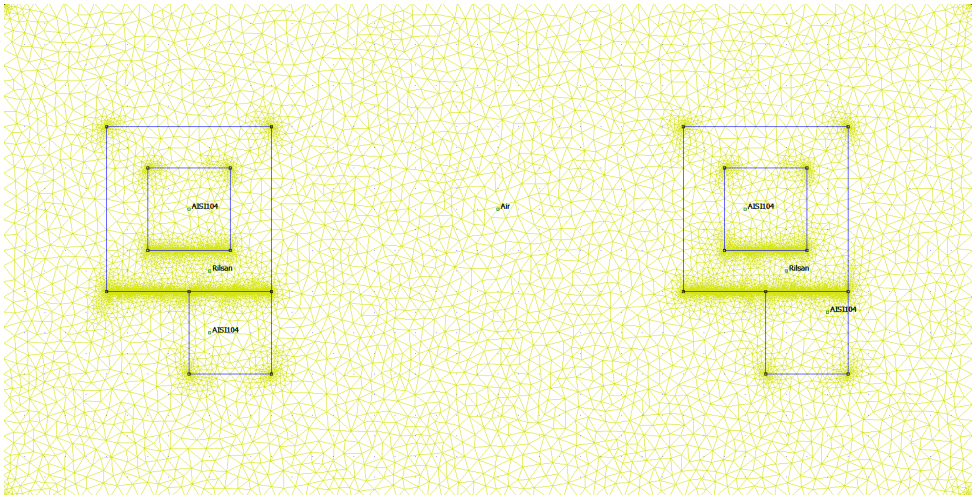

Figure 3.11 – Illustration of the 2D model geometry and mesh of GAPS used in the simulations. The model includes the assignment of materials AISI 104 steel for the electrodes and Rilsan for the dielectric layer. The configuration is surrounded by air. The view is a cut plane of the real DBD reactor, of which only 2 cells are represented.

where V is the applied voltage across the electrodes in volts and W_c is the energy in joules. The integral of the electric field energy density, $u = \frac{1}{2}\epsilon E^2$, over the volume of the capacitor is computed to determine the total stored energy W_c:

$$W_c = \int \frac{1}{2}\epsilon E^2 \, dV$$

where ϵ is the permittivity of the dielectric material, E is the electric field strength, and dV is the differential volume element.

The simulation results are obtained with a fixed potential on the coated electrode of 400V to prove the initiation of the discharge presented in the previous section by the equivalent circuit results. The simulation results indicate a capacitance of 500 pF for the aligned configuration and 150 pF for the displaced configuration, closely aligning with the experimental observations. Notably, the actual configuration of the reactor electrodes is displaced, as substantiated by the observed capacitance value of 147 pF,

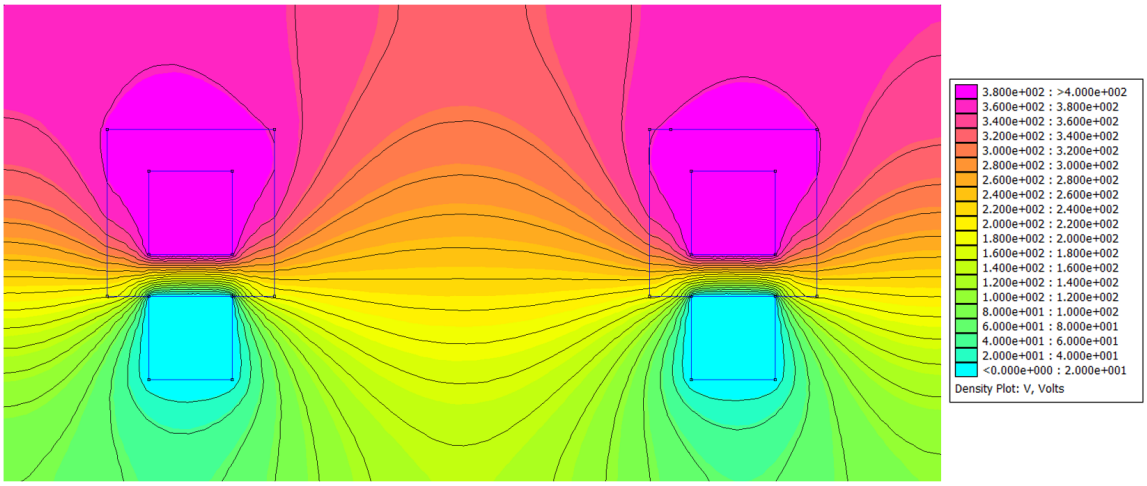

(a) Potential distribution with HV electrode at 400V, before the discharge ignition, for the aligned configuration.

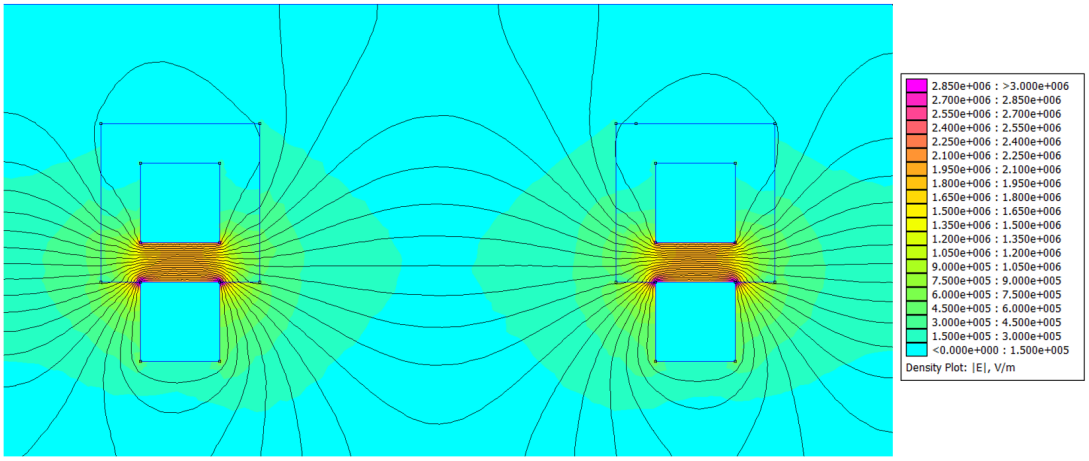

(b) Electric field intensity when the HV electrode is at 400V, before the discharge ignition, for the aligned configuration.

Figure 3.12 – (a) Potential distribution for the aligned electrode configuration, with electrodes perfectly parallel. The color legend ranges from blue (low voltage, ground) to red (high voltage, 1.2 kV). (b) Electric field intensity map.

both with the Lissajous figure slope and the LCR meter measure, suggesting a robust correlation with the experimental data.

Figures 3.12 and 3.13 illustrate the density plots of electric field intensity and the potential for each configuration, aligned and displaced, respectively. In both configurations, a pronounced electric field is concentrated at the interface where the exposed electrode and the dielectric layer meet, around the edges. A zoom-in view of the electric field intensity around the edge is show in Figure 3.14 for a more comprehensive view of the femm simulation results. The intensity profile of the electric field ($|E|$) near the electrodes contact line (red line L in Figure 3.14) is further explored in Figure 3.15a and 3.15b. Here, the peak intensities are localized at the edge (end of red line), where the dielectric strength of air of 3 kV/mm is exceed allowing the ignition of the discharge.

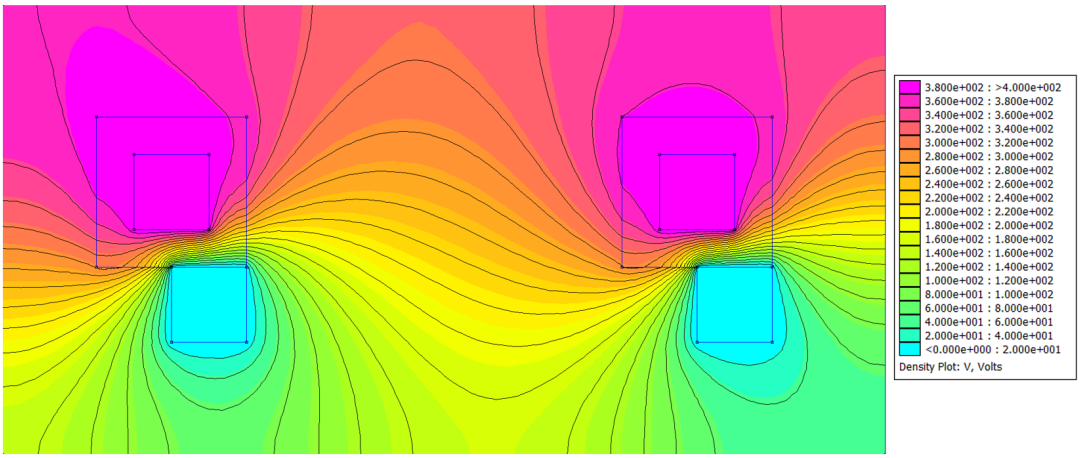

(a) Potential distribution with HV electrode at 400V, before the discharge ignition, for the misaligned configuration.

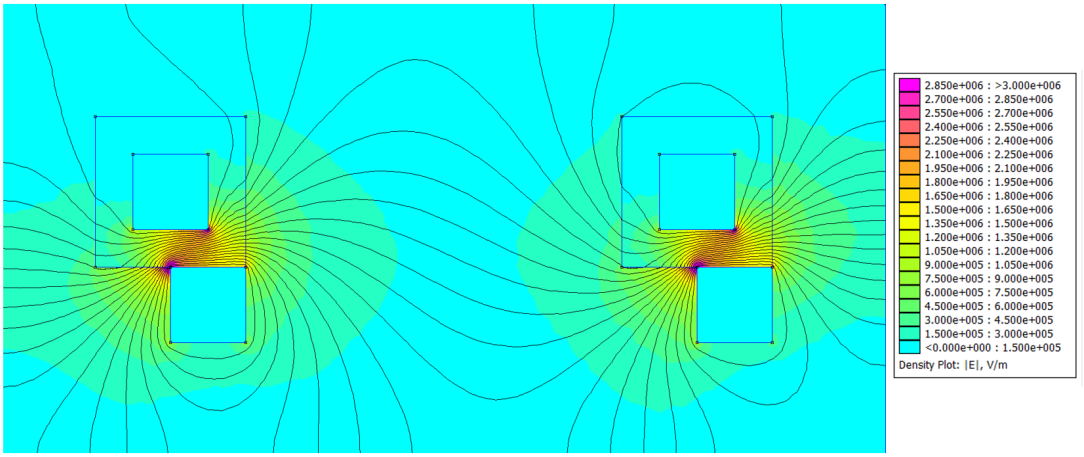

(b) Electric field intensity when the HV electrode is at 400V, before the discharge ignition, for the misaligned configuration. Equipotential lines are shown.

Figure 3.13 – (a) Potential distribution for the misaligned electrode configuration, where the electrodes are slightly offset. The color legend ranges from blue (low voltage, ground) to red (high voltage, 1.2 kV). (b) Electric field intensity map.

This result is in line with the results found with the analytical model. Figure 3.4 vividly captures the plasma discharge occurring precisely at these high-intensity points. The 3.15b shows the result for the same identical simulation but with the high voltage electrode at 1200V before the discharge, to evaluate the behaviour in the case of the applied voltage before the ignition is higher than the effective one, and is the peak voltage of 1.2 kV supplied by the pulsed generator. The graph shows that the intensity of the electric field remains within the dielectric withstand limit of Rilsan ®, which guarantees a dielectric strength up to 10 kV/mm for thicknesses up to 100 μm.

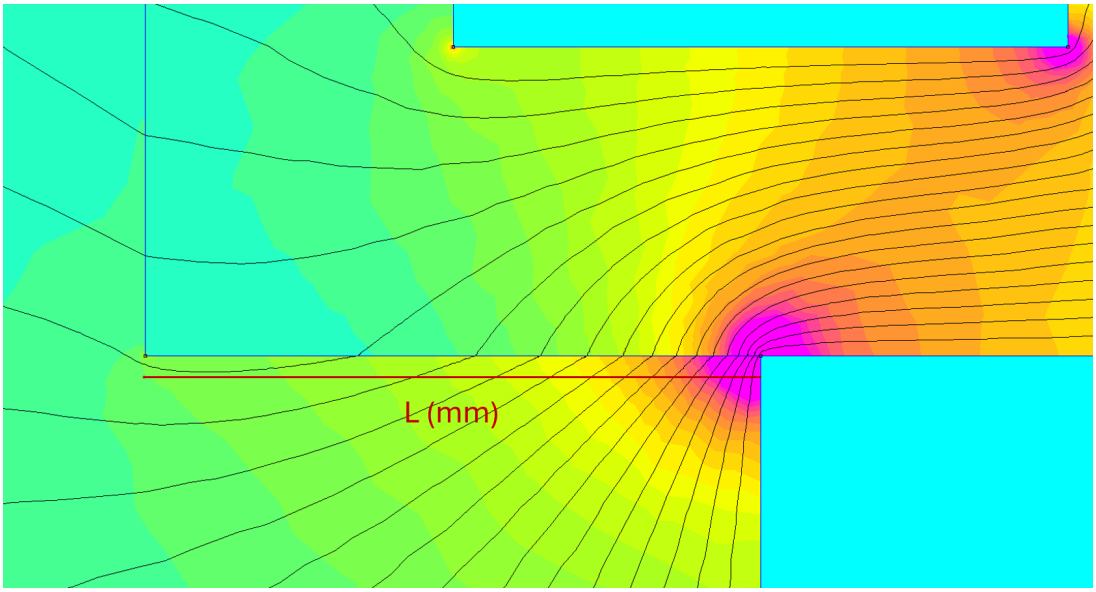

Figure 3.14 – A zoom-in view of the electric field intensity around the edge of the exposed electrode. The red line 'L' represents the path along which the electric field intensity profile is evaluated.

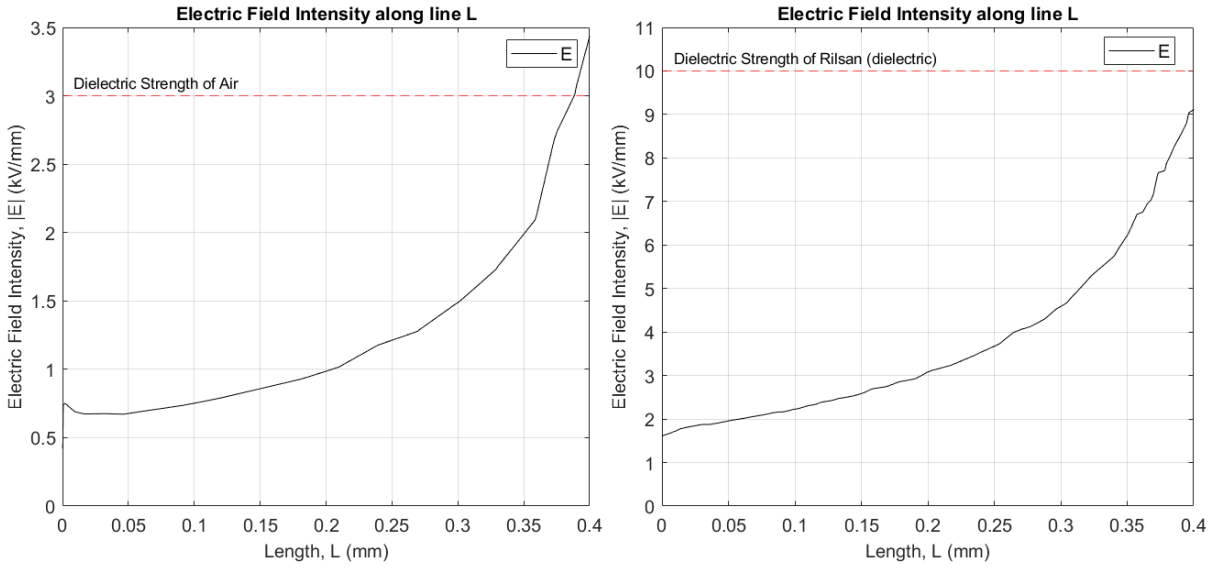

(a) Electric Field Intensity along line L for 400V. **(b)** Electric Field Intensity along line L for 1200V.

Figure 3.15 – Plot of the electric field intensity ($|E|$) evaluated in kV/mm along the designated path red line L, for different high voltages.

3.1.2 Fluidodynamic Charatcerization

Computational Fluid Dynamics (CFD) is a numerical approach used to simulate fluid flow and analyze various physical phenomena associated with fluid behavior, such as velocity distribution, pressure gradients, and turbulence effects. In this study, CFD was employed to understand the fluid dynamics within the proposed DBD reactor, providing insights into the motion of bioaerosols and the influence of flow characteristics on treatment efficiency.

The simulations were conducted using SimScale, a cloud-based platform that offers powerful tools for solving complex fluid flow problems. SimScale was chosen due to its versatility and ease of use, allowing for efficient setup, mesh generation, and solution computation. The main objective of this simulation is to visualize the flow profile inside the reactor under defined operating conditions, ensuring that the reactor's design supports uniform distribution and effective interaction of bioaerosols with the plasma areas. For this reason, the domain considered for the 3D simulation is the space inside the GAPS through which the bioaerosol would pass. To obtain this volume, a 3D CAD of the entire GAPS was made by using SolidEdge (see Figure 2.12) and create the 'negative' volume of the geometry, thus obtain the empty spaces. The final results is shown in Figure 3.16.

Simulation Parameters and Boundary Conditions

For the CFD simulations, air was used as the working fluid, assuming standard atmospheric conditions. The inlet velocity was derived based on the volumetric flow rate of 12.5 LPM (Liters Per Minute) used in the experimental setup. Given the cross-sectional area of the inlet pipe (FESTO fitting) of 25 mm^2, the resulting inlet velocity was calculated as follows:

$$\text{Inlet velocity} = \frac{\text{Flow rate}}{\text{Cross-sectional area}} = \frac{12.5\,\text{LPM} \times \frac{1}{60}\,\text{m}^3/\text{s}}{25 \times 10^{-6}\,\text{m}^2} \approx 8.3\,\text{m/s} \tag{3.1}$$

The inlet velocity boundary condition was set to 8.3 m/s, while the outlet was defined with an atmospheric pressure boundary condition (0 bar pressure gauge) to match the conditions measured in the experimental setup using a manometer. A reference image of the boundary conditions is shown in Figure 3.16, where the inlet and outlet surfaces, along with the reactor walls, are clearly marked.

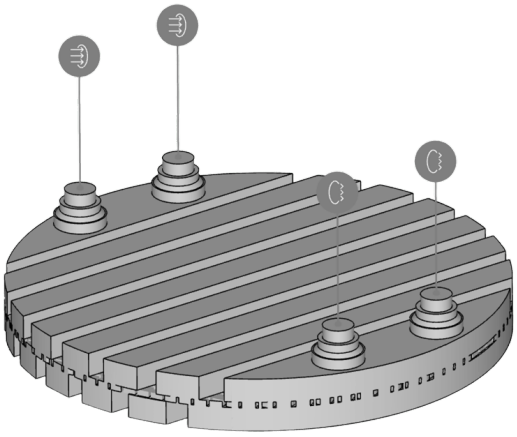

Figure 3.16 – CAD of the volume affected by the bioaerosol flow inside the GAPS used for the 3D CFD simulation. Boundary conditions selection of inlet velocity and outlet pressure are shown.

Mesh Creation

A structured mesh was generated for the reactor geometry to ensure an accurate representation of the flow field, focusing on the regions around the inlet and outlet where high gradients in flow variables are expected. The mesh was created with tetrahedral elements, with local refinements around critical areas such as the inlet, outlet, and chamber edges to capture the fine details of the flow. Mesh details are shown in Figure 3.17.

Key mesh parameters:

- **Element type**: Tetrahedral
- **Maximum element size**: 0.001 mm
- **Minimum element size**: 0.0001 mm
- **Number of nodes**: 14 million (to ensure adequate resolution of flow features)
- **Boundary layer refinement**: Three layers were used around the walls to resolve the near-wall flow accurately.
- **Mesh independence**: Mesh sensitivity analysis was conducted to confirm that further refinement did not significantly alter the results.

These parameters were chosen to balance computational cost with the accuracy of the solution, ensuring a good representation of the flow dynamics while maintaining reasonable computational time, which was around 3 hour over 300 cores.

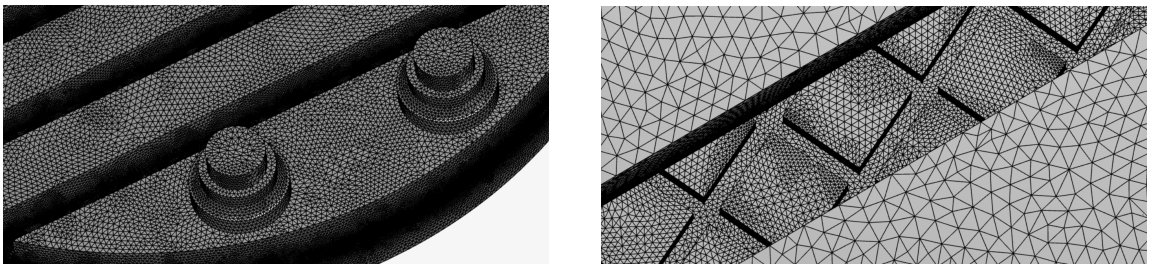

(a) (b)

Figure 3.17 – Mesh details used for the CFD simulation of the DBD fluid dynamics. (a) Inlet/outlet region, and (b) grid-electrode intersection area.

Simulation Setup and Solver Parameters

The flow within the reactor was modeled as an incompressible fliud in steady-state. The governing equations for mass and momentum conservation were solved using the standard k-omega SST turbulence model, which is suitable for capturing turbulence effects in confined flows like the one inside the DBD reactor.

Simulation setup parameters:

- **Fluid**: Air (incompressible)
- **Solver type**: Steady-state, simple algoritm
- **Turbulence model**: k-omega SST

The choice of these parameters was based on standard CFD practices for internal flows, ensuring numerical stability and convergence of the solution.

Simulation Results

The simulation was executed on SimScale servers, with cores automatically allocated based on the project settings. The total simulation time was 311 minutes, utilizing 322.15 core hours. The simulation results are visualized using particle tracing to illustrate the airflow pattern within the DBD reactor. Figure 3.19 shows the particle trajectories, indicating the flow direction and velocity distribution inside the reactor. The particle tracing revealed a uniform flow distribution along the central axis of the reactor, with slight recirculation zones near the inlet and outlet regions. These results confirm that the designed flow conditions support effective transport and mixing of bioaerosols, ensuring consistent and homogeneous exposure to the plasma treatment. The velocity profile of a GAPS section between one inlet and one outlet of the 3D CFD simulation is

shown in Figure 3.18, where the color scale is the same of that used for particle tracing representations (Figure 3.19).

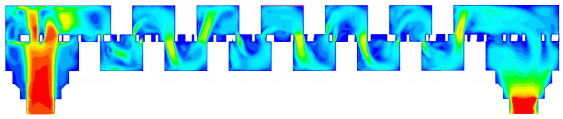

Figure 3.18 – The velocity profile of a GAPS section between one inlet and one outlet of the 3D CFD simulation performed with SimScale.

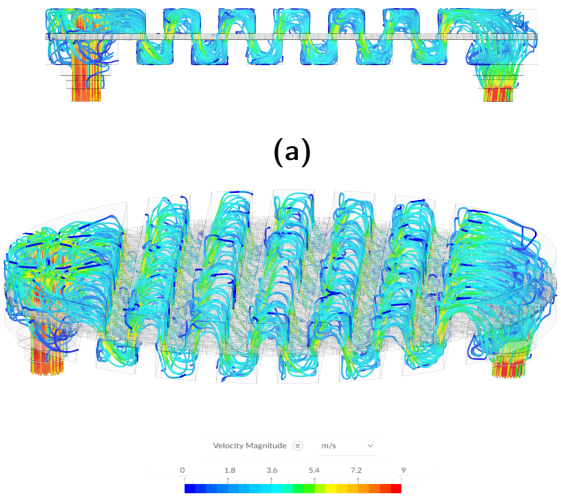

(a)

(b)

Figure 3.19 – The particle tracing results of the 3D CFD simulation performed with SimScale. (a) Isometric view. (b) Side view.

The airflow enters the reactor through the inlet ports, and as shown in the particle tracing in Figure 3.19a and 3.19b, it extends across the entire surface of the electrodes, covering the full area of the DBD. This configuration facilitates both direct and indirect treatment of the bioaerosol. Direct treatment occurs as the bioaerosol passes through the grid electrodes and comes into direct contact with the plasma discharge, while indirect treatment happens in the serpentine path, which becomes filled with reactive species produced by the discharge, which will be analyzed in Section 3.2.

It is challenging to estimate the direct and indirect treatment times separately due to uncertainties in the actual plasma volume generated. However, the residence time of the

bioaerosol within the reactor, which combines both direct and indirect treatment, can be measured. It is possible to obtain a first estimate of the residence time by considering the total volume traversed by the flow and the given flow rate. The volume traversed by the bioaerosol flow, estimated using the geometry from the CAD model created with SolidEdge software, is:

$$V_{\text{bioaerosol}} = 35860.186\,\text{mm}^3 = 3.586 \times 10^{-5}\,\text{m}^3 \tag{3.2}$$

The flow rate is 12.5 LPM, the same as used in the real experiment, and can be converted to cubic meters per second as follows:

$$\dot{V} = 12.5\,\frac{\text{L}}{\text{min}} = \frac{12.5 \times 10^{-3}\,\text{m}^3}{60\,\text{s}} = 2.083 \times 10^{-4}\,\frac{\text{m}^3}{\text{s}} \tag{3.3}$$

The estimated residence time, $t_{\text{res}_{\text{est}}}$, of the bioaerosol inside the reactor is then calculated as:

$$t_{\text{res}_{\text{est}}} = \frac{V_{\text{bioaerosol}}}{\dot{V}} = \frac{3.586 \times 10^{-5}\,\text{m}^3}{2.083 \times 10^{-4}\,\frac{\text{m}^3}{\text{s}}} \approx 0.172\,\text{s} \tag{3.4}$$

However, this estimation does not account for the actual geometry and flow path inside the reactor, which strongly influences the residence time. The trajectory of the bioaerosol depends on the internal geometry and flow distribution rather than just the total volume.

To refine the estimate, calculations were performed considering the shortest possible path from the inlet to the outlet, accounting only for the geometric constraints of the reactor's serpentine structure, without additional flow deviations. Using the velocity profile obtained from the CFD simulation, the residence time for this shortest path was determined to be $t_{\text{res}} = 25\,\text{ms}$. Conversely, considering the longest plausible path—following the perimeter of the reactor's circular section—the residence time is approximately doubled, yielding to $t_{\text{res,longest}} \approx 47\,\text{ms}$. These results highlight the strong dependence of residence time on the actual bioaerosol trajectory, demonstrating that a simple volume-to-flow-rate ratio is not sufficient for an accurate estimation of exposure within the reactor.

During this residence time, the bioaerosol is exposed to the plasma discharge generated by a micropulsed power supply, which produces a square wave of ± 1.2 kV at a frequency of one pulse every 1 ms. Given the residence time of 0.025 seconds, the bioaerosol is subjected to approximately 50 discharges (double discharge per period, as

explained in 3.1.1) while passing through the reactor. This ensures that the bioaerosol receives multiple exposures to both the direct and indirect plasma treatment in the serpentine path. This exposure to dozens of discharges during each passage through the reactor ensures high treatment efficacy and efficiency. In fact, as demonstrated by Friedman and Gallagher et al. [14], a significantly lower number of discharge exposures is already sufficient to achieve a good treatment outcome.

3.2 FTIR Chemical Analysis Results

This section details the in-situ FTIR measurements conducted using GAPS configuration utilized for the non-biological experiments within the bio-plasma reactor chamber specifically adapted for FTIR analysis, as already described in Section 2.3.4. The GAPS reactor, operating with a microsecond square waveform bipolar voltage at peak levels of ± 1.2 kV and a total bipolar pulse length of 8 microseconds at 1 kHz, was enclosed within a bio-plasma reactor chamber equipped for FTIR measurements. Figure 3.20 illustrates the experimental setup. The setup involved two distinct experimental conditions:

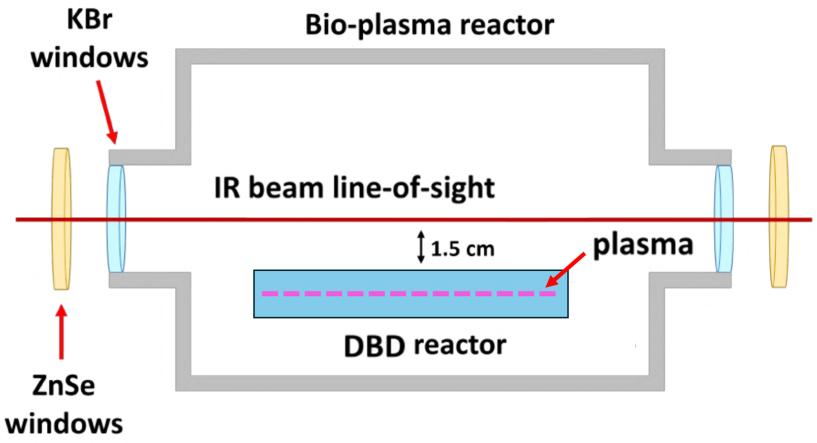

Figure 3.20 – Schematics of the in-situ FTIR experimental setup of the GAPS reactor measurements.

- Static mode without airflow, ambient air, low humidity equal to 20%.
- Dynamic mode with an airflow rate of 12.5 LPM, humid air at 70% RH.

FTIR spectra were acquired over a 15-minute duration with measurements taken every 30 seconds. Figures 3.21 and 3.21 show a significant absorption peak of KBr at around 1352 cm^{-1}, indicative of the irreversible surface transformation of the reactor windows.

This phenomenon was consistently observed across different settings. The evolving spectra, captured under both static and flow conditions, highlighted notable differences in peak formations, specifically the Ozone peak results are quite different. To better represent the time evolution in the two configurations, a few time steps are shown in Figures 3.22 and 3.24.

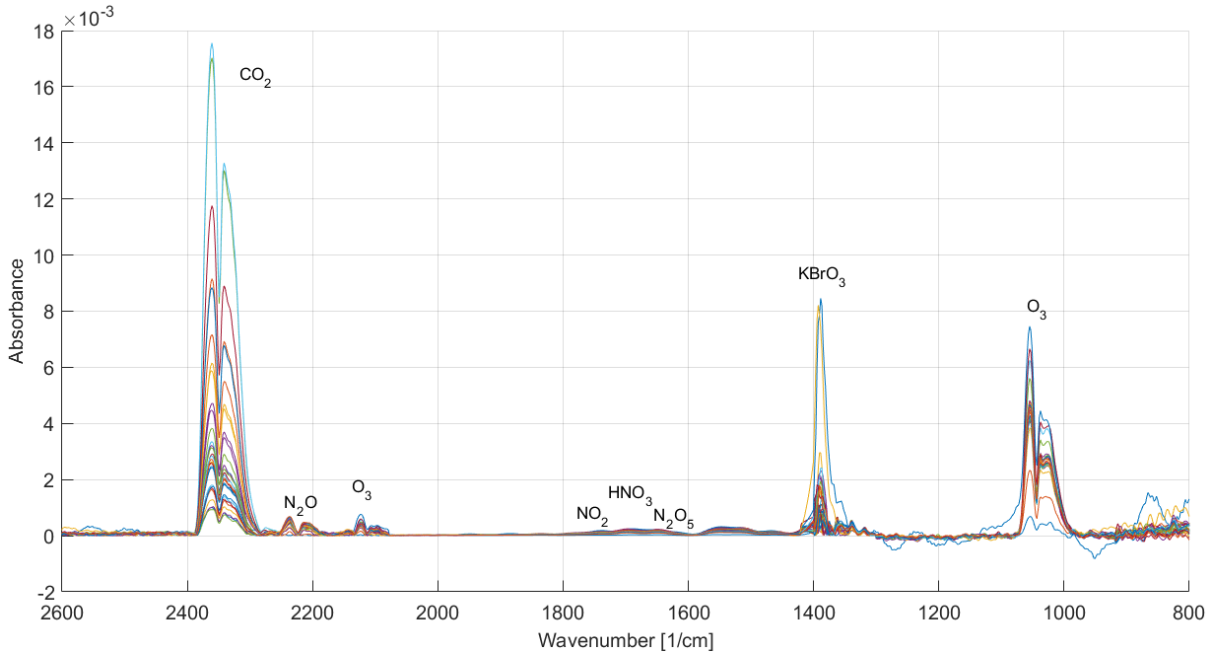

Figure 3.21 – FTIR spectra, represented in arbitrary units, across the *full* wavelength range, recorded during a 15-minute operation of GAPS in static mode at 20 %RH static configuration, illustrating the dynamic buildup of different chemical species across consecutive spectral acquisitions (distinct colors).

To achieve a humidity level of 70% RH the BLAM nebulizer is used (for more details see Section 2.1), but with the solution to be nebulized devoid of biological samples. The humidity level and temperature are measured inside the bio-plasma reactor chamber by a Vaisala HM42PROBE (see Figure 3.25). This configuration, 12.5 LPM 70%RH, is tailored to replicate biological experimental conditions.

In Figure 3.26 and 3.27, the distinct temporal trends of O_3 and N_2O during the FTIR measurements are showcased for static and dynamic (12.5 LPM airflux) case respectively. The examination of the data reveals significantly different behaviors for ozone under the two scenarios analyzed. In the flow configuration, there is no noticeable increase in ozone concentration, attributable to the lack of accumulation due to the continuous air renewal. In contrast, in the static setup, there is a clear progressive increase in ozone. This rise is particularly marked in the initial minutes of full plasma operation, followed

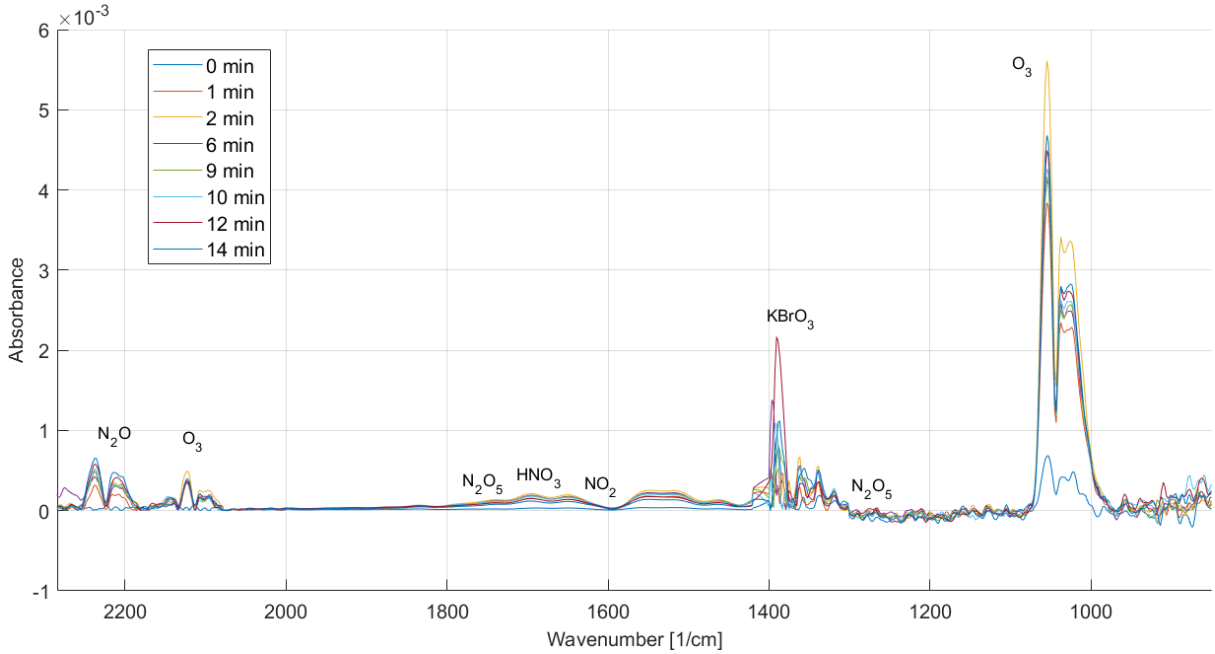

Figure 3.22 – FTIR spectra, represented in arbitrary units, across a *zoomed* wavelength range, recorded during a 15-minute operation of GAPS in static mode at 20 %RH static configuration, illustrating the dynamic buildup of different chemical species across consecutive spectral acquisitions (distinct colors).

by a highly dynamic decrease of ozone concentration. The decrease rise time is not seen by the FTIR measurements due to the high sampling rate of 30 seconds. This decrease is in line with GAPS behaviour in static condition after flux condition, as seen in 3.1.1 , where the discharge gradually switches off and reaches a stable low power plasma discharge condition. This latter condition still permits a gradual accumulation of the chemical species, that for the ozone seems to stabilize at 45 ppm.

The lower value in ozone concentration between the fluxed and the static set-up highlights the difference in relative humidity, in fact with higher %RH the ozone is expected to decrease. The concentration of NO_2 is not shown due to the noisy signal found for both configurations. Figure 3.26b and 3.27b shows that the concentration of N_2O keeps around few ppm, not precisely showing any trend differences between the two case. The ozone concentration significantly surpasses that of the other species, attributed to the low surface power density of GAPS plasma discharge. The power used in this setup is approximately $\simeq$ 0.6 W and assuming that the plasma-covered surface is 4033.97 mm^2 (half the grid-electrode surface area), the surface power density is approximately $\simeq 0.014\, W/cm^2$. This value is notably below the $\simeq 0.1 W/cm^2$ threshold identified in [95], which distinguishes the so-called 'ozone-mode' from the 'nitrogen oxides-mode'. According to [96], the CT value for the exposure of *E. coli* to the ozone is $4 \times 10^{-2}\, mg \cdot min/l$ with a two-log reduction in the viable microorganism concentration. The CT value, or so called contact time, is the product $[A] \cdot t$, where $[A]$ is the

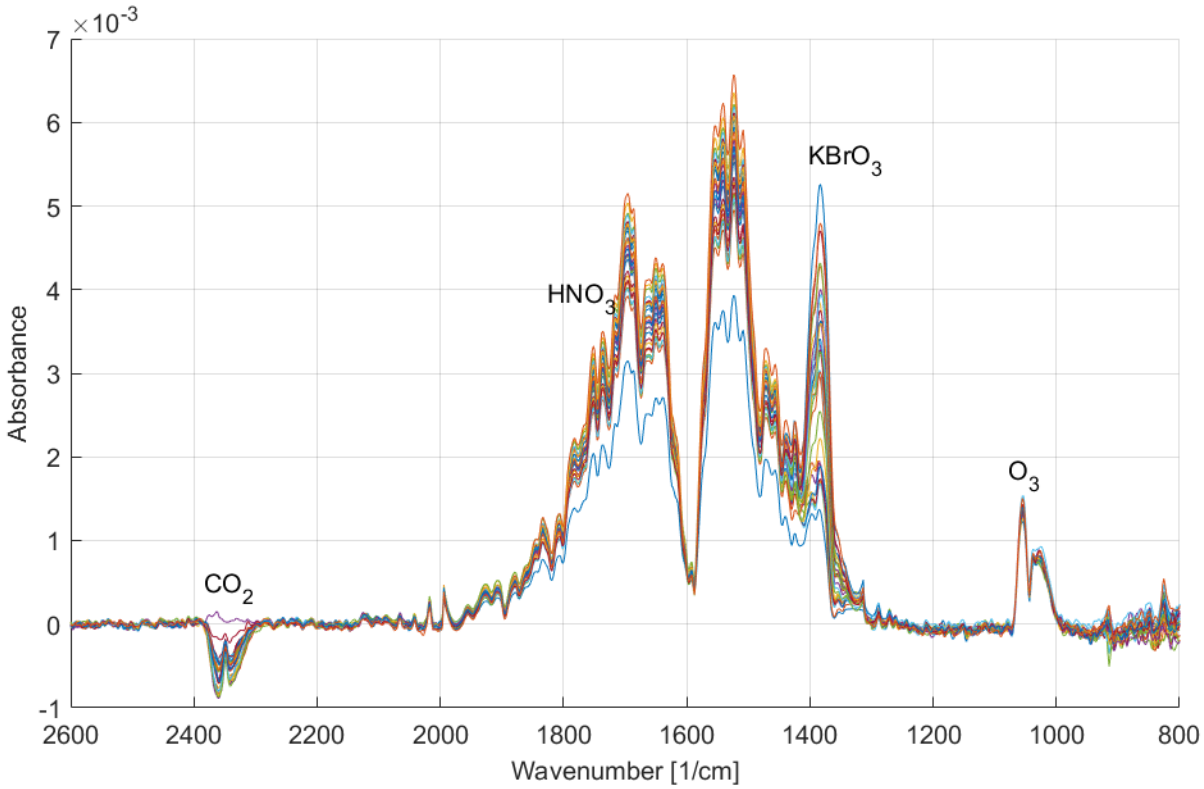

Figure 3.23 – FTIR spectra, represented in arbitrary units, across the *full* wavelength range, recorded during a 15-minute operation of GAPS in flow mode at 70 %RH configuration, illustrating the dynamic buildup of different chemical species across consecutive spectral acquisitions (distinct colors).

concentration of the interacting species and t is the time of exposure. Given the amount of ozone produced by GAPS during an exposure time of $t_{\text{res}} = 25\,ms$, the calculation is:

$$\frac{ppm \cdot PM}{25.45} = \frac{9 \cdot 48}{25.45} = 17.67\,mg/m^3 = 0.017\,mg/l \tag{3.5}$$

$$CT = \frac{0.017 \cdot 25 \cdot 10^{-3}}{60} = 4{,}1 \cdot 10^{-4}\,mgmin/l \tag{3.6}$$

The value $4{,}1 \times 10^{-4}\,mg \cdot min/l$ is two orders of magnitude below the above mentioned value. Although the CT value is a target expressed for ozone treatment only, and in a plasma treatment the actors are surely more, it can be used to assess that ozone is probably not the main agent for the decontamination. In fact, one can say that the main role is played by the short lived species acting during the direct plasma treatment. Moreover, the electrode surface temperature of GAPS was measured by FLIR T1020 infrared-thermal camera and found to be around room temperature, $\simeq 30°C$ (Figure 3.28).

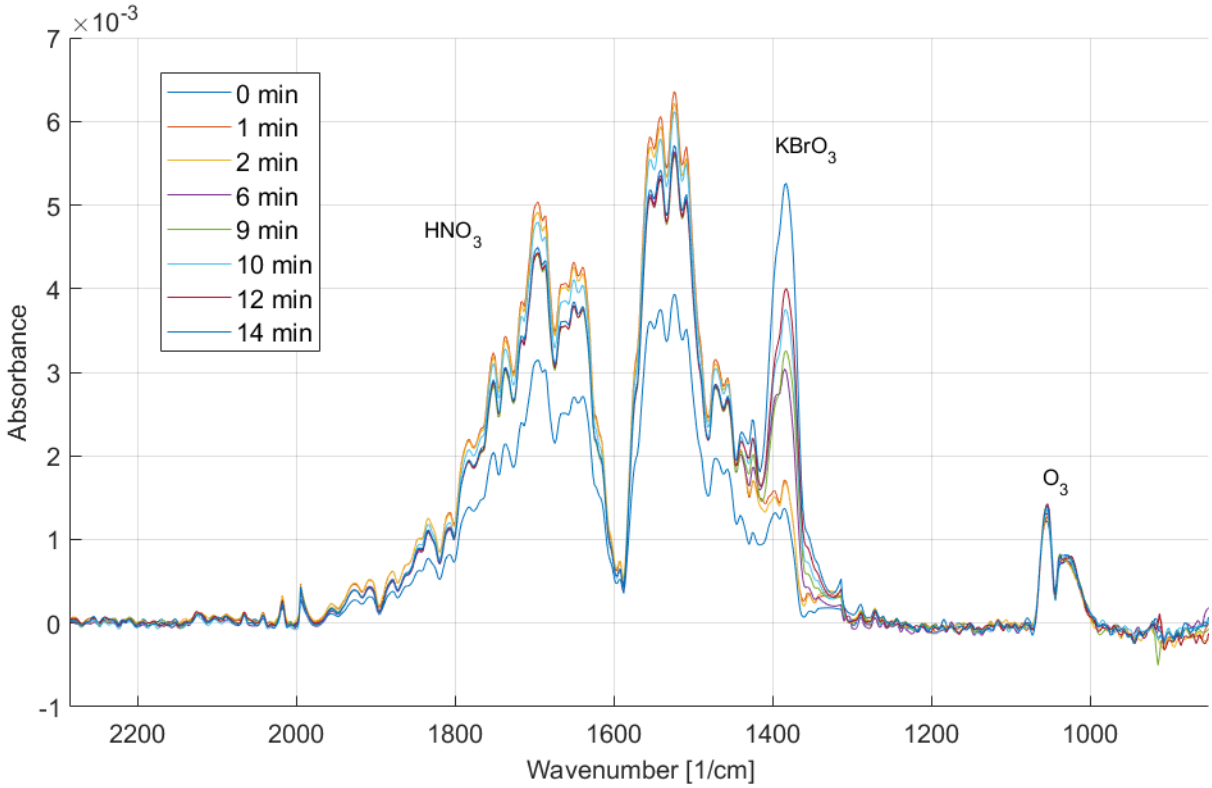

Figure 3.24 – FTIR spectra, represented in arbitrary units, across a *zoomed* wavelength range, recorded during a 15-minute operation of GAPS in flow mode at 70 %RH configuration, illustrating the dynamic buildup of different chemical species across consecutive spectral acquisitions (distinct colors).

Figure 3.25 – Vaisala HM42PROBE humidity probe used to measure %RH level inside the bio-plasma reactor chamber for FTIR spectra acquisition.

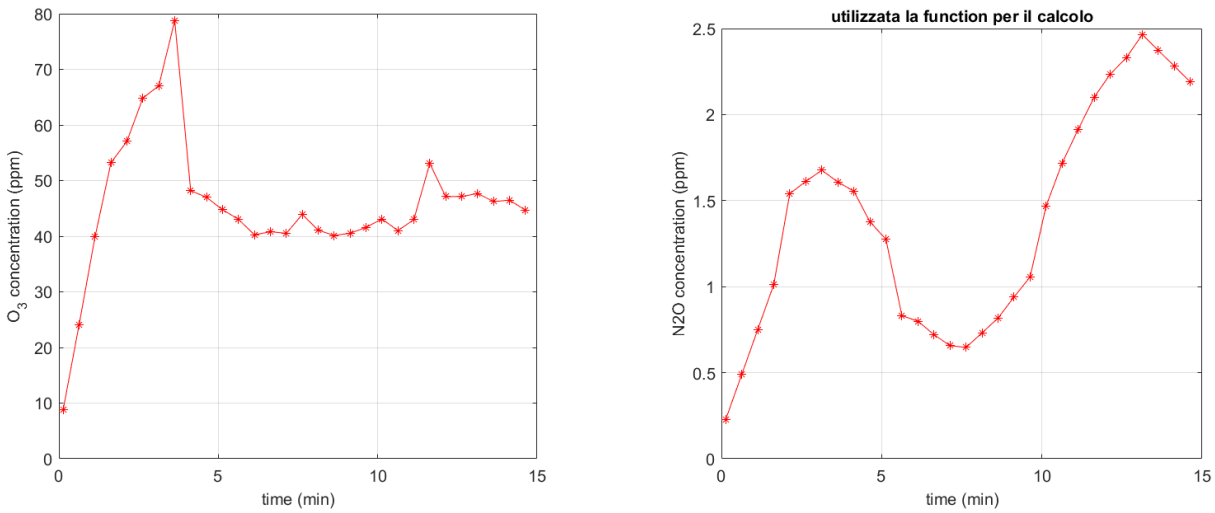

(a) (b)

Figure 3.26 – Temporal concentration trends of chemical species measured using FTIR for static 20%RH condition. (a) Ozone (O_3). (b) Nitrous oxide (N_2O).

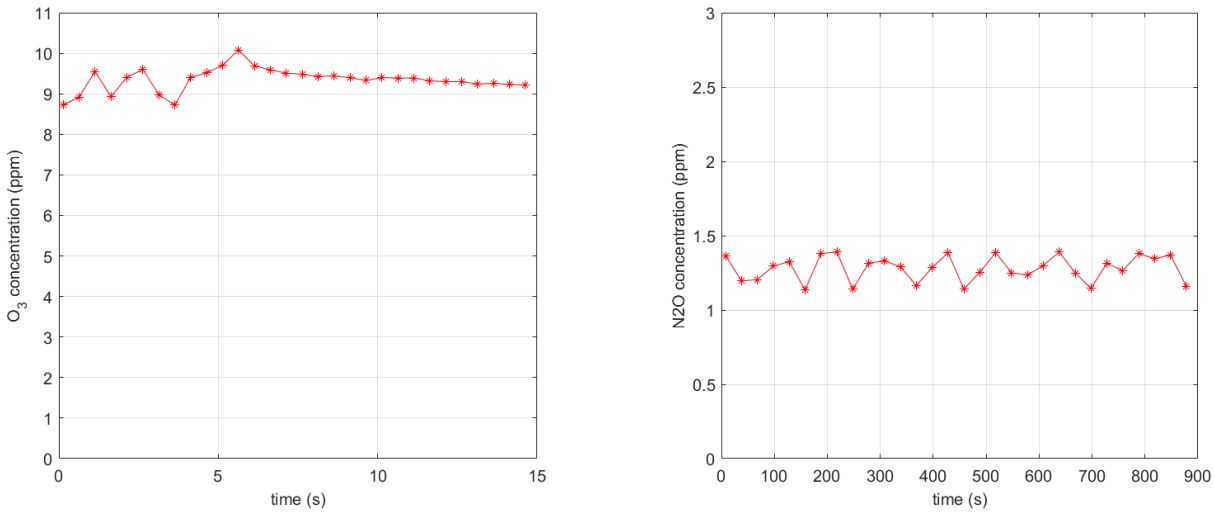

(a) (b)

Figure 3.27 – Temporal concentration trends of chemical species measured using FTIR for 12.5 LPM airflux 70%RH condition. (a) Ozone (O_3). (b) Nitrous oxide (N_2O).

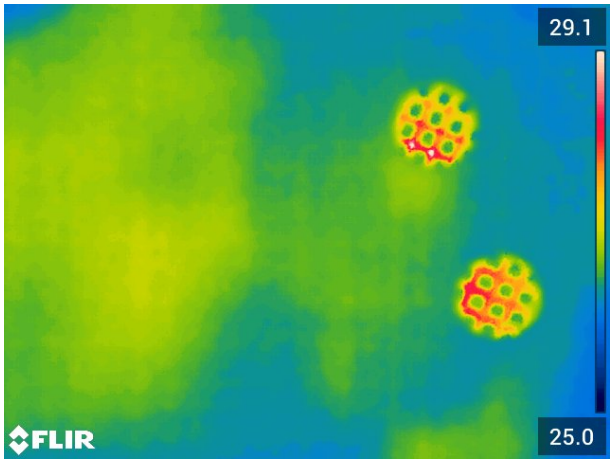

Figure 3.28 – Temperature distribution on GAPS electrode surface with FLIR T1020 infrared-thermal camera.

3.3 Biological Treatment

In this section, the results obtained from biological tests conducted using the experimental setup described in Chapter 2 are presented. The real laboratory set-up is shown in Figure 3.29. The figure shows also a detailed photo of the GAPS set-up inside the experiment configuration (3.29b) and its relative discharge (3.29c). The GAPS is inside a custom 3D-printed support, needed for the 12.5 LPM airflux mode. These results were carried out in the Bio-plasmas lab, at SPC in Lausanne. This laboratory is equipped with the necessary infrastructure for the safe handling and management of non-pathogenic bacteria (BSL1 - biological safety level). The laboratory includes essential equipment such as laminar flow cabinets, ultra-cold freezers ($-80°C$), autoclaves, and more. The Bio-plasmas lab stands out as a unique laboratory that accommodates both the biological and physiochemical aspects of this research.

In order to assess GAPS efficiency and efficacy in bioaerosol treatment, the setup was employed in two configurations: *plasma-off* and *plasma-on*. The *plasma-off* configuration allowed us to assess and quantify any inherent losses within the setup itself, specifically those not attributable to plasma treatment. This approach is essential to establish a reliable baseline for subsequent plasma-on experiments. In fact, measuring the bacterial losses without the discharge permits to evaluate the set-up efficiency in generating and sampling the bioaerosol. Moreover, comparing the concentration inside the two impinger, *Control* and *Treated*, when no discharge is ON, is essential to claim that the results inside the Biosamplers are comparable.

When operating in plasma-off mode, significant losses were observed from the initial nebulization stage to the first control measurement, as depicted in column bars comparison in Figure 3.30a. These losses are attributed to various factors, including the materials used in the setup, the inherent inefficiency of the nebulization process, and the sampling method's own efficiency limitations. Notably, these losses were prominent between the nebulization and the control sample stages, while no further reduction was noted between the *Control* and *Treated* samples under plasma-off conditions (see column bars in Figure 3.30b). This finding confirmed that any observed microbial reduction in subsequent plasma-on experiments would be solely due to the plasma treatment and not influenced by additional setup losses.

To illustrate this, Figure 3.30 presents a graph showing the concentration at the nebulization stage when the bacterial concentration is the one inside the syringe ready for nebulization process (*syringe* labeled bar), followed by a noticeable decrease in the control concentration (*Control* labeled bar). This reduction highlights losses inherent in the setup and sampling processes, as previously discussed. As already presented

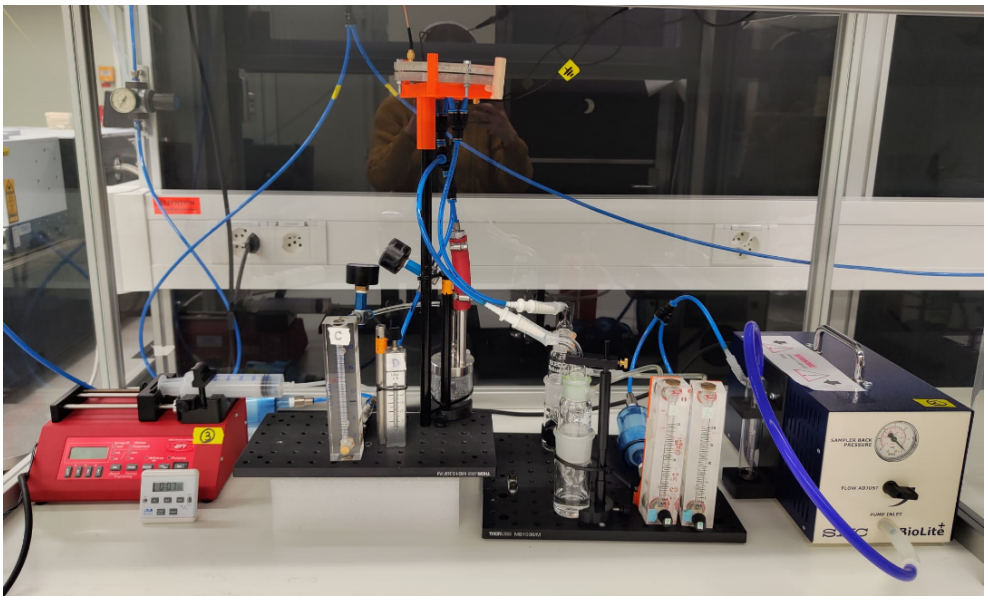

(a)

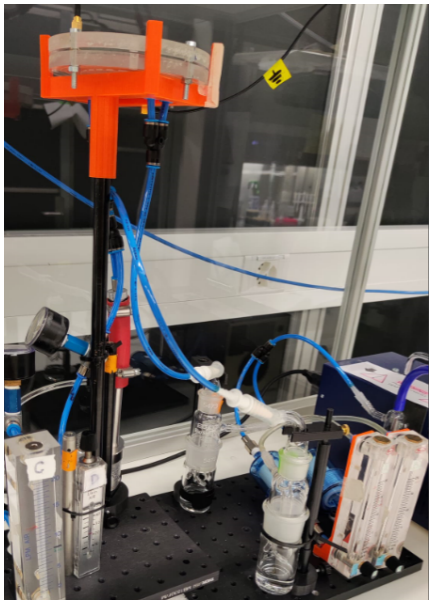

(b)

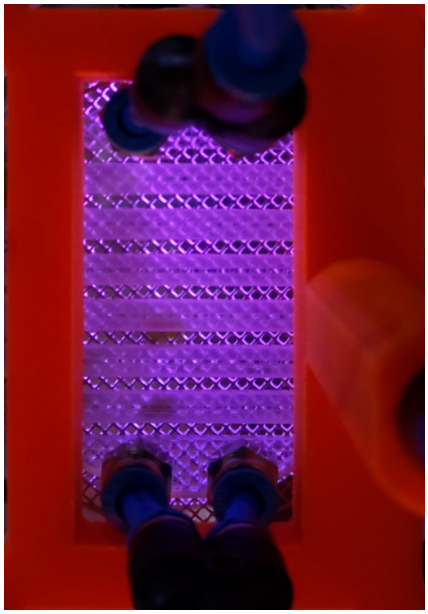

(c)

Figure 3.29 – Photographic documentation of the experimental setup. (a) inside the hood. (b)Detailed view of the reactor. (c) Plasma discharge inside the experimental set-up.

in sub-section 2.2.3, we can account for the nebulization losses and dilution in the airflow to account for an ideal initial bacterial concentration (*Ideal* labeled bar). This ideal concentration is find by dividing the Equation 2.5 by the actual volume inside the BioSampler at the end of the experiment in plasma-off conditions.

In Figure 3.30a, the portion due to set-up losses is shown (between the lowest and middle dashed lines), excluding those from nebulization (between the higher and middle dashed lines) which are unchangeable. To improve set-up losses, one potential modification is the use of conductive tubes instead of the polyurethane (PU) tubes

used in this setup. Conductive materials could mitigate the memory effect of the PU, thereby reducing bacterial accumulation due to electrostatic effects. Additionally, the length of the tubing can also influence setup losses. The label 'ideal' in Figure 3.30 shows the bar relative to the real losses due to the set-up losses and sampling. The difference between this value and the Control concentration, even if does not directly affect the treatment results (thanks to the double impinger solution), is important in the view of set-up optimization. In fact, to prove higher log-reduction one should see a higher concentration in the Control sampler, thus lowering the sampling losses. This was done by trying different volumes of the collection liquid inside the BioSampler. As explained in 2.2.1, PBS is the collection liquid used in the experiments and by increasing the liquid volume inside the BioSampler from 15 to 20 ml, we achieved significantly improved results. Specifically, the concentration detected within the *Control* sampler increased, thereby reducing sampling losses, and also the reduction between the *Control* and *Treated* sampler was reduced, as shown in Figure 3.32.

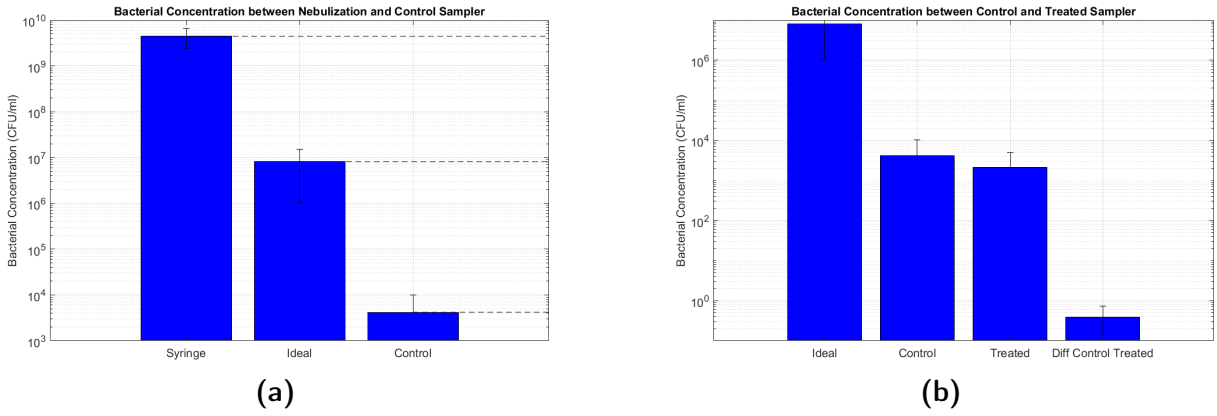

Figure 3.30 – Bacterial concentration in the various steps of the bioaerosol treatment set-up. (a) Bacterial concentration inside the syringe (before nebulization), ideal case (counting for nebulization efficiency), inside control sampler (accounting for setup losses and sampling losses). (b) Bacterial concentration for ideal case, control sampler, treated sampler (accounting for GAPS switched off losses) and difference between *Control* and *Treated* (with GAPS switched off).

Additionally, the difference between the BioSamplers' concentrations, is directly linked to the reliability of the treatment results. In fact, the minimal reduction observed between the points of collection — before and after treatment when the plasma is off — indicates that any variations post-treatment can be directly attributed to the effects of the plasma treatment itself. This is shown in Figure 3.30b and optimized as described above and shown in Figure 3.31.

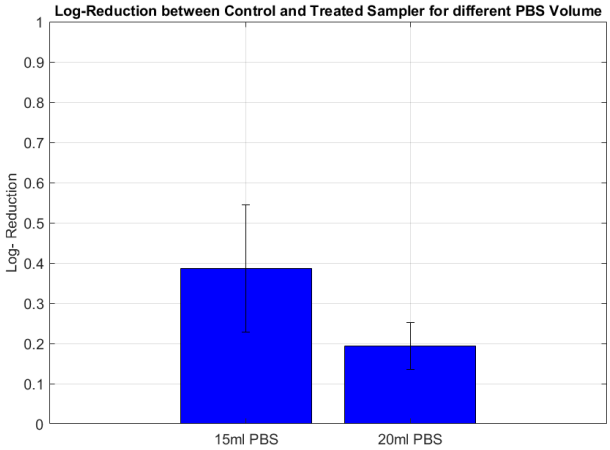

Figure 3.31 – Logaritmic reduction between *Control* and *Treated* sampler for different PBS (collection liquid) volume, 15ml and 20ml.

Subsequent experiments were conducted with the plasma-on configuration, where GAPS reactor was activated to treat the *E. Coli* bioaerosol. These experiments were repeated multiple times to ensure consistent reproducibility, with error bars included to represent the variability observed across trials. The *plasma-on* results demonstrated a significant log reduction between *Control* and *Treated* samples, reaching up to a 4-log reduction, as shown in Figure 3.32. This indicates the high efficacy of the plasma treatment in inactivating microbial load within the bioaerosol samples. The results of GAPS switch on, but without the stable condition of the flux mode (50% of the discharge area compared to the flux condition) are presented, showing a lower log-reduction but still quite high. These results remarks upon the higher efficiency of direct treatment and the need of optimize the interaction area between plasma and bioaerosol. [14].

The biological results were quantified using the CFU counting method, as illustrated in Figure 3.33, which displays the Agar Plates for both the *Control* and *Treated* samples. The control plate shows a visible presence of bacterial colonies, while the treated sample plate reveals a complete absence of detectable colonies. This finding supports a 4-log reduction in bacterial count, indicating that the plasma treatment was highly effective. Importantly, no bacteria were observed on the treated plates, reaching the experimental detection limit of 0.33 CFU per milliliter (0 bacteria over 3 Agar Plate of 1ml of bacterial solution). This suggests that the actual log reduction achieved could potentially exceed 4 logs, as our detection method limits further quantitative verification. This is represented with a dashed black line in the Figure 3.32, depicted as the 'Detection Limit', to indicate that the log-reduction could be higher.

The reduced plasma exposure, the 50% discharge mode, yielded a 2-log reduction in bacterial counts, against the > 4-log obtained in the 100% discharge mode. This result suggests a proportional relationship between the extent of plasma coverage and the

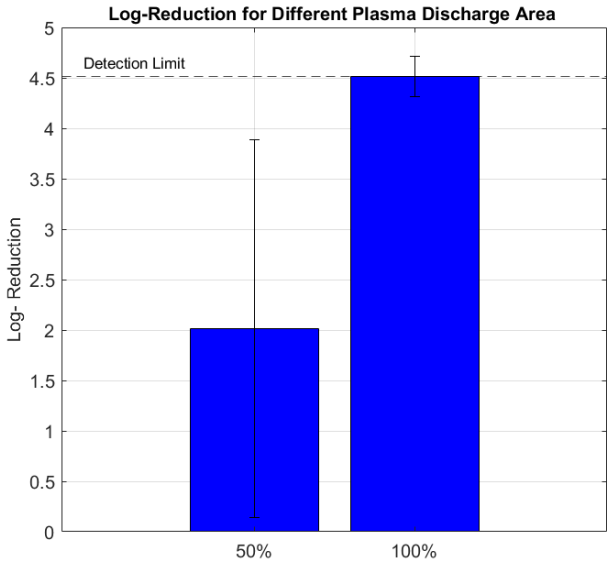

Figure 3.32 – Logaritmic reduction for different plasma discharge area, 50% and 100% (relative to the discharge area obtained with 12.5 LPM air flux condition.)

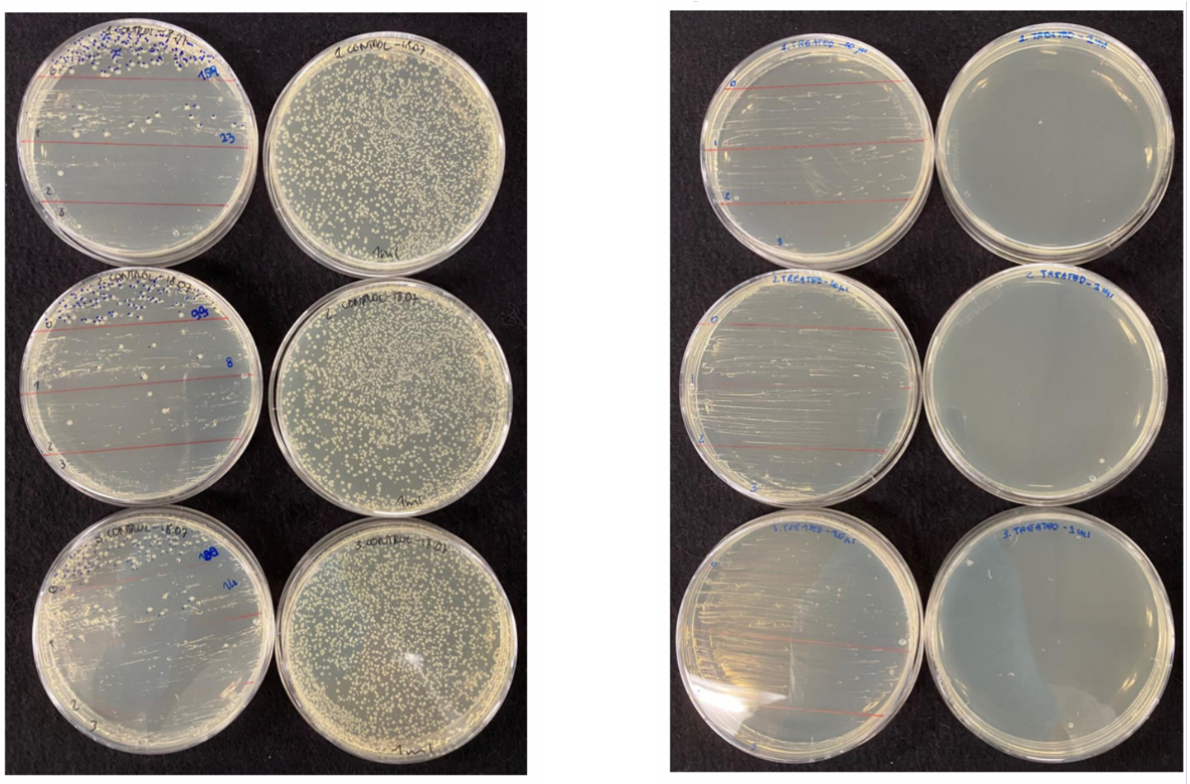

(a) **(b)**

Figure 3.33 – Examples of the agar plate for CFU counting method for (a) Control sample and (b) Treated sample.

degree of microbial reduction, indicating a potential linear correlation between plasma generation and treatment efficacy. This can be helpful to try to evaluate the actual efficiency of the DBD reactor in order to compare it with other existing devices. This can be done with the Electrical Energy per Order (EEO) index, explained in the next section.

3.4 GAPS Reactor Efficiency

The Electrical Energy per Order (EEO) is a parameter used to evaluate the energy efficiency of systems designed for contaminant reduction, particularly in air and water disinfection applications. The EEO quantifies the amount of electrical energy required to reduce the concentration of a contaminant by one order of magnitude (i.e., a 90% reduction, or 1-log reduction). This parameter is essential for comparing the energy efficiency of different treatment technologies, such as electrostatic precipitators (ESP), ozonizers, plasma reactors, and other purification systems.

The EEO is calculated using the following formula:

$$\text{EEO} = \frac{P \times t}{V \times \log_{10}\left(\frac{C_{\text{in}}}{C_{\text{out}}}\right)} \tag{3.7}$$

where:

- P is the electrical power consumed by the system, measured in kilowatts (kW),
- t is the exposure or treatment time, measured in hours (h),
- V is the total volume of gas or liquid treated, measured in cubic meters (m^3) or liters (L),
- C_{in} is the initial concentration of the contaminant,
- C_{out} is the concentration of the contaminant after treatment.

The EEO is typically expressed in units of kWh/m^3 per order or J/L per order, where 1 kWh/m^3 is equivalent to $3600 J/L$. The choice of units depends on the treatment context (air or water).

The EEO represents the energy required to achieve an exponential reduction in contaminant concentration. In practice:

- A *1-log reduction* implies a 90% decrease in the initial concentration,
- A *2-log reduction* implies a 99% decrease,
- A *3-log reduction* implies a 99.9% decrease, and so forth.

Thus, if a device has an EEO of, for example, 0.2 kWh/m^3 per order, it means that 0.2 kilowatt-hours are needed to reduce the contaminant concentration by one order of magnitude for each cubic meter of air or liquid treated.

The EEO enables a fair comparison of various treatment technologies under similar conditions. For instance, lower EEO values indicate higher energy efficiency, as less energy is required to achieve the *same contaminant* reduction. It is important to note that the EEO is an average indicator and does not account for variables such as contaminant type, operating conditions (e.g., temperature, humidity), and concentration distribution within the treated volume. Therefore, for an accurate comparison, the EEO should be interpreted within the context of similar experimental conditions. This can be misleading because inactivation efficacy strongly depends on the initial concentration, that it is not taken into account in the index. In fact, reaching 1-log with low efficiency is much easier than reaching a higher log-reduction and then accounting for it by dividing for the log-reduction achieved in Equation 3.7. Nonetheless, it is still a good indicator and can be used to qualitatively compare different devices. For this purpose, the EEO for the proposed DBD reactor is calculated below.

In this research, we observed that a 2-log reduction was achieved with roughly 0.2 W, while a 4-log reduction was achieved with 0.6 W of power. This suggests a quasi-linear relationship between the power applied and the log reduction, implying a consistent EEO value across different power levels. Since the power measured for the 100% discharge mode is more accurate, it will be utilized for the index calculation.

Table 3.2 – Comparison of EEO values for *Escherichia coli* disinfection across different air disinfection technologies. Adapted from [97].

Air Disinfection Technology	**EEO** (kWh m^{-3} $order^{-1}$)	**Ref**
UV disinfection and photocatalysis	6.6×10^{-3}	[98]
	2.0×10^{-4}	[99]
	3.3×10^{-3}	[100]
Ozone disinfection	2.4×10^{-4}	[101]
	2.0×10^{-4}	[14]
Electrified disinfection	1.2×10^{-4}	[102]
Electrostatic precipitation	8×10^{-4}	[103]
	6.5×10^{-4}	[104]
	4.4×10^{-4}	[105]
Plasma disinfection	1.90×10^{-2}	[106]
	1.2×10^{-2}	[107]
	7.18×10^{-2}	[107]
Microwave disinfection	2.8×10^{-1}	[108]

For the index calculation, the following parameters are used:

- $P = 0.6\,\mathrm{W} = 0.6 \cdot 10^{-3}\,kW$
- $t = 25\,\mathrm{ms} = 6.94 \cdot 10^{-6}\,h$, treatment time of one pass of the bioaerosol.
- $V = 12.5\,LPM \cdot 25\,ms = 12.5\,LPM \cdot 4.16 \cdot 10^{-4}\,min = 5 \cdot 10^{-6}\,m^3$, the treated volume during one bioaerosol pass.
- $\log_{10}\left(\frac{C_{\mathrm{in}}}{C_{\mathrm{out}}}\right) = 4$

Substituting the values into the Equation 3.7 we obtain:

$$\mathrm{EEO} = \frac{0.6 \cdot 10^{-3} \times 6.94 \cdot 10^{-6}}{5 \cdot 10^{-6} \times 4} = 2 \times 10^{-4}\,\mathrm{kWh/m^3}\ \text{per order}$$

This result indicates that the EEO for a single plasma treatment is $2 \times 10^{-4}\,\mathrm{kWh/m^3}$ per order, demonstrating an efficient energy consumption for this plasma disinfection setup. Compared to other existing devices based on plasma treatment, as summarized in Table 3.2, the energy consumption is 2 order of magnitude lower than the existing plasma technology [97].

Chapter 4

Conclusions and Future Research

The quality of air has become, in recent years, the subject of numerous studies aimed at improving air quality by inactivating microorganisms present in recirculated airflows and optimizing technologies dedicated to air disinfection. . Traditional air purification technologies, while effective, such as High-Efficiency Particulate Air (HEPA) filters and ultraviolet germicidal irradiation (UVGI), have revealed limitations in fully addressing the range of challenges posed by airborne pathogens. HEPA filters, adept at trapping particulate matter, do not neutralize pathogens but rather prevent their circulation, and UVGI systems, though effective in microbial inactivation, require stringent operational conditions to achieve desired outcomes. In this context, atmospheric pressure non-thermal plasma (NTP) generated by Dielectric Barrier Discharge (DBD) has attracted significant attention in the biomedical field over the past few decades. Although DBD has been widely studied for surface sterilization, there is a noticeable lack of research focused on its use in air sanitization. In this context, the development of a novel Cold Atmospheric Plasma (CAP) based device designed for continuous bioaerosol flux treatment in indoor environments represents a significant advancement. This thesis provides a comprehensive characterization of a newly designed CAP Dielectric Barrier Discharge (DBD) reactor, named **GAPS — Grid-like Air Plasma Sanitizer**, developed to optimize the interaction between plasma discharge and bioaerosol flux. The research encompassed extensive electrical, chemical, and biological assessments to validate the efficacy and efficiency.

The electrical and fluid dynamic characterizations have confirmed the operational stability and homogeneity of the plasma discharge and treatment area. Computational Fluid Dynamics (CFD) simulations provided essential insights into the airflow patterns within the reactor, ensuring a homogenous distribution of bioaerosols and effective interaction with the plasma. The results of the fluid dynamics simulation performed

using SimScale demonstrate that the serpentine design ensures multiple passages of the airflow through the discharge zones. The temperature on the electrode surface does not exceed 30°C, and the power consumption under nominal flow rate conditions and maximum discharge surface is $0.65W$. Considering the plasma surface as the entire electrode in contact with the dielectric, the specific power is calculated to be $0.014W/cm^2$. The specific power is low compared to other air disinfection technologies and also compared to other plasma DBD reactor aimed for air disinfection. From a chemical perspective, the reactor's plasma was analyzed using Fourier-transform infrared (FTIR) spectroscopy, which elucidated the formation of reactive oxygen and nitrogen species (RONS) crucial for the oxidative degradation of pathogens. The operational regime at full capacity was identified as 'ozone mode', producing 9 ppb of ozone and less than 2 ppm of nitrous oxide. The comparison with the standard CT value for *Escherichia Coli* showed that ozone is probably not the main actor in the decontamination process. In fact, most of the inactivation rersults from the short lived species acting during the direct plasma treatment. Biological testing showed the reactor's significant efficacy in inactivating *Escherichia coli*, thereby underscoring the potential of CAP technology to reduce bioaerosol loads effectively. The microbial viability assays demonstrated the effectiveness of plasma treatment in significantly reducing bacterial counts and enabled the calculation of the Electrical Energy per Order (EEO) index. The EEO was determined to be $2 \times 10^{-4}\ kWh/m^3$ per order, , which is two orders of magnitude lower than that of other plasma-based air disinfection technologies.

Despite these promising results, the study acknowledges certain limitations, particularly concerning the variability of bioaerosol composition and environmental conditions, which may influence treatment outcomes. Future research should therefore focus on exploring these variables in greater depth to optimize reactor performance comprehensively. Additional studies should be conducted to scale the device up for a real-world applications and analyze its energy efficiency in a real-world environments. Additionally, the measurement set-up for bioaerosol treatment should be optimized to extend the achievable log reduction. Finally, ozone measurements were not compared to the limit levels suggested by European standards, as the technology is still far from commercialization. Moreover, various ozone filters (such as activated carbon filters, catalytic ozone destructors, and metal oxide-based filters) are already available on the market and could be integrated into a future final version of the reactor. This thesis contributes to the field by detailing the development and validation of an innovative CAP device, GAPS, for air decontamination. It offers a robust platform for future research efforts to explore and refine this technology, aiming to enhance its applicability and effectiveness in real-world settings. The potential for GAPS device to be integrated into existing air

purification systems opens up new avenues for creating more resilient and healthier indoor environments in the post-pandemic era.

Appendix A

Laboratory Prototype

The development of the first prototype of the proposed Cold Atmospheric Plasma (CAP) Dielectric Barrier Discharge (DBD) reactor, GAPS - Grid-like Air Plasma Saitizer, was a long and challenging journey, marked by numerous errors and iterations, particularly in configuring the grid-like electrodes. As shown in the figures, the initial grids featured an interwoven structure, which led to multiple failures during testing and significant difficulties in selecting an appropriate coating. Over time, the transition to flat grids proved to be a breakthrough, facilitating testing and enabling a much more reproducible discharge configuration.

Additionally, the external structure of the reactor underwent several modifications to achieve a robust design while ensuring efficient plasma discharge and bioaerosol flow through the reactor. A critical aspect of the redesign was preventing leakages and guiding the bioaerosol precisely through the perforations in the grid-like electrodes, optimizing its exposure to the plasma treatment. These improvements ultimately resulted in a more reliable and scalable prototype, paving the way for further experimental validation and potential applications.

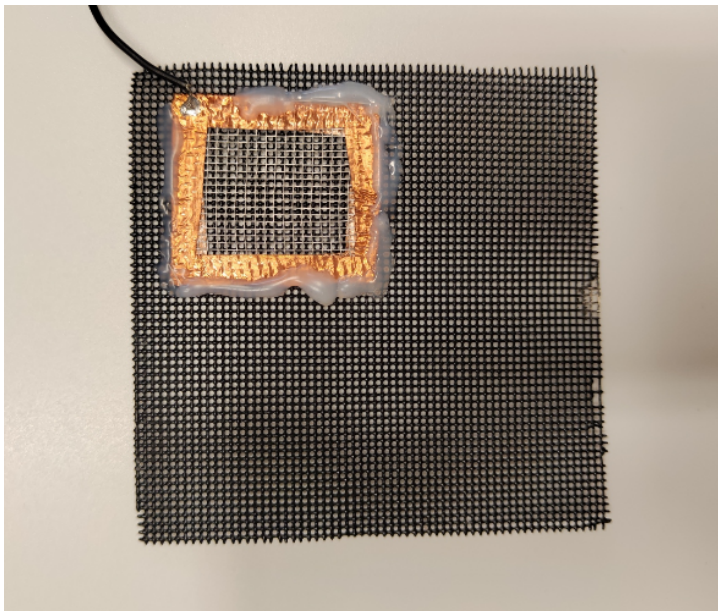

(a)

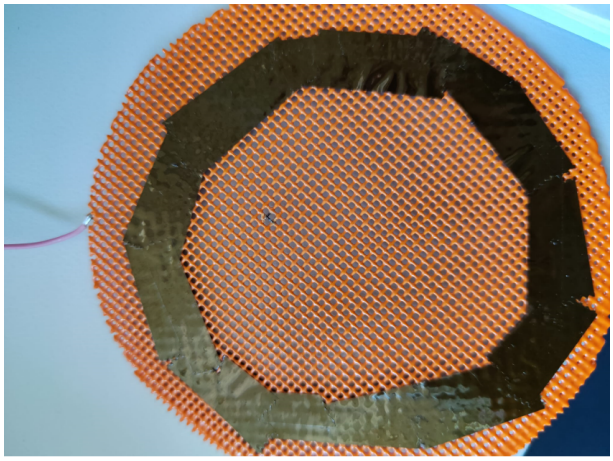

(b)

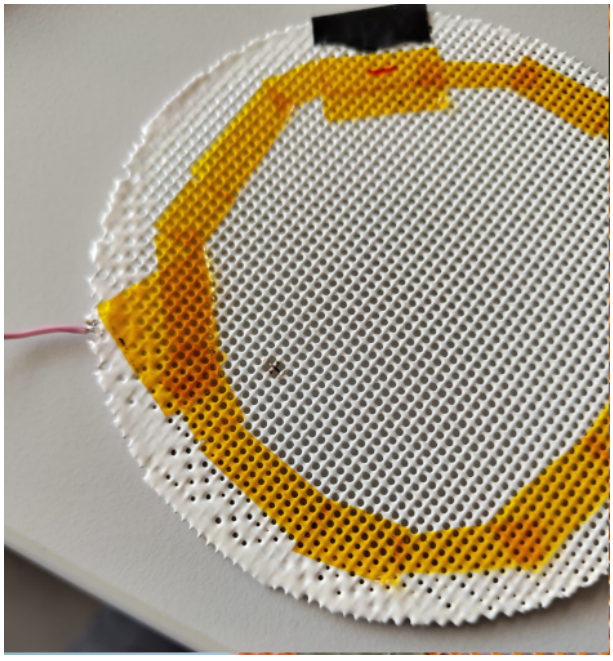

(c)

Figure A.1 – First attempts of choosing, building and designing the grid-like electrode and its relative coating material.

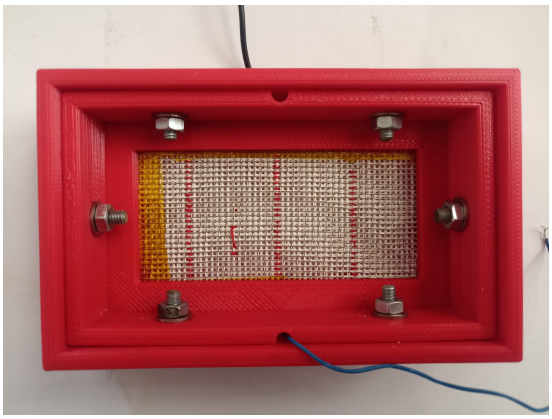

(a) Rectangular Prototype

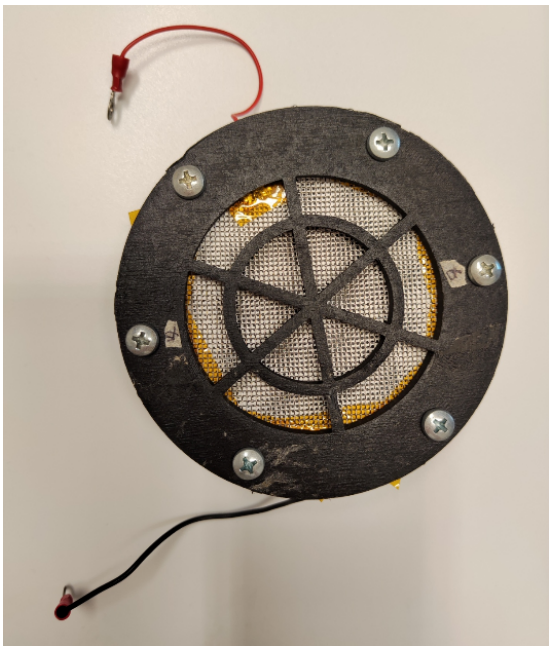

(b) Open Circular Design - 1

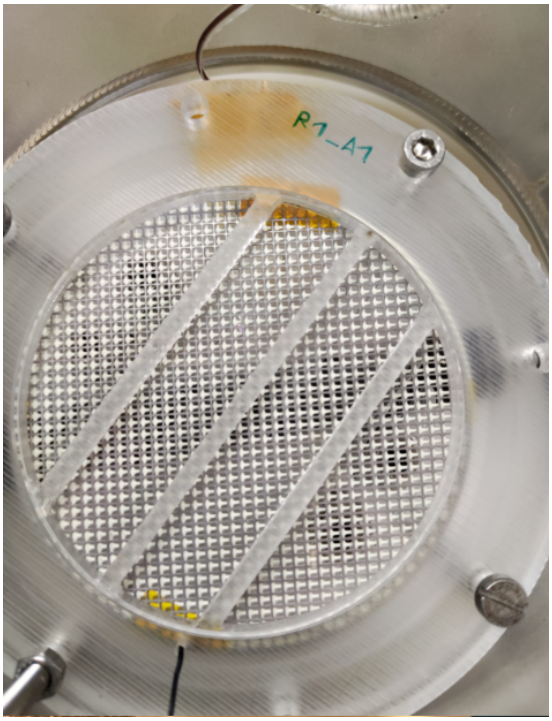

(c) Open Circular Design - 2

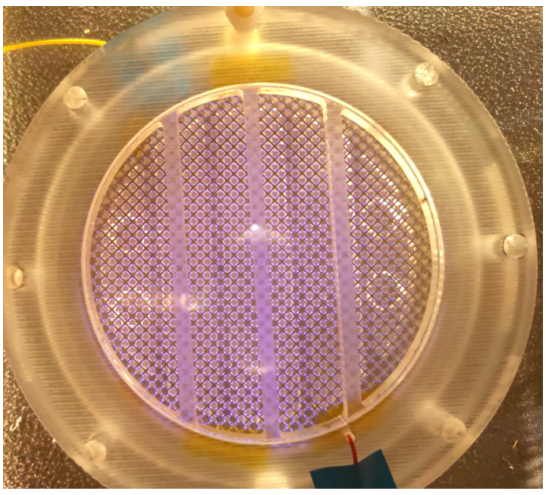

(d) Open Circular Design - on

Figure A.2 – First GAPS reactor prototype designs.

List of Figures

List of Tables

Bibliography

[1] L. Morawska and J. Cao. "Airborne transmission of SARS-CoV-2: The world should face the reality". In: *Environment International* 139 (2020), p. 105730.

[2] Joseph G Allen and Linsey C Marr. "Recognizing and controlling airborne transmission of SARS-CoV-2 in indoor environments". In: *Indoor air* 30.4 (2020).

[3] James E Farnsworth et al. "Development of a method for bacteria and virus recovery from heating, ventilation, and air conditioning (HVAC) filters". In: *Journal of Environmental Monitoring* 8.10 (2006), pp. 1006–1013.

[4] F. Memarzadeh, R. N. Olmsted, and J. M. Bartley. "Applications of ultraviolet germicidal irradiation disinfection in health care facilities: Effective adjunct, but not stand-alone technology". In: *American Journal of Infection Control* 38.5 SUPPL. (2010), S13–S24.

[5] Y. Li et al. "Role of ventilation in airborne transmission of infectious agents in the built environment–a multidisciplinary systematic review". In: *Indoor air* 17.1 (2007), pp. 2–18.

[6] S. Escobedo and H. de Lasa. "Photocatalysis for Air Treatment Processes: Current Technologies and Future Applications for the Removal of Organic Pollutants and Viruses". In: *Catalysts* 10 (2020), p. 966. DOI: 10.3390/catal10090966. URL: https://doi.org/10.3390/catal10090966.

[7] Gentry Berry et al. "A review of methods to reduce the probability of the airborne spread of COVID-19 in ventilation systems and enclosed spaces". In: *Environmental Research* 203 (2022), p. 111765.

[8] Mounir Laroussi. "A Brief Note on the History of the Dielectric Barrier Discharge and Its Application for Biological Decontamination". In: *IEEE Transactions on Radiation and Plasma Medical Sciences* 6.1 (2022), pp. 121–125. DOI: 10.1109/TRPMS.2021.3051805.

[9] Kolawole Adesina et al. "A Review of Dielectric Barrier Discharge Cold Atmospheric Plasma for Surface Sterilization and Decontamination". In: *IEEE Transactions on Radiation and Plasma Medical Sciences* (2024). DOI: 10.1109/TRPMS.2024.1234567.

[10] Haotian Gao et al. "Atmospheric-pressure non-equilibrium plasmas for effective abatement of pathogenic biological aerosols". In: *Plasma Sources Science and Technology* 30.5 (2021), p. 053001.

[11] Mounir Laroussi et al. "Low-temperature plasma for biology, hygiene, and medicine: Perspective and roadmap". In: *IEEE Transactions on Radiation and Plasma Medical Sciences* 6.2 (2021), pp. 127–157.

[12] Dana Ziuzina et al. "Atmospheric cold plasma inactivation of Escherichia coli in liquid media inside a sealed package". In: *Journal of applied microbiology* 114.3 (2013), pp. 778–787.

[13] Fuxiang Liu et al. "Inactivation of bacteria in an aqueous environment by a direct-current, cold-atmospheric-pressure air plasma microjet". In: *Plasma Processes and Polymers* 7.3-4 (2010), pp. 231–236.

[14] Michael J Gallagher et al. "Rapid inactivation of airborne bacteria using atmospheric pressure dielectric barrier grating discharge". In: *IEEE Transactions on Plasma Science* 35.5 (2007), pp. 1501–1510.

[15] Gediminas Mainelis. "Bioaerosol sampling: Classical approaches, advances, and perspectives". In: *Aerosol Science and Technology* 54.5 (2020), pp. 496–519.

[16] Nguyen Trung Hiep et al. "A review on sterilization methods of environmental decontamination to prevent the coronavirus SARS-CoV-2 (COVID-19 virus): A new challenge towards eco-friendly solutions". In: *Science of The Total Environment* 904 (2023), p. 166021.

[17] Neha Kaushik et al. "The inactivation and destruction of viruses by reactive oxygen species generated through physical and cold atmospheric plasma techniques: Current status and perspectives". In: *Journal of Advanced Research* 43 (2023), pp. 59–71.

[18] Torsten Gerling, Andreas Helmke, and Klaus-Dieter Weltmann. "Relevant plasma parameters for certification". In: *Comprehensive Clinical Plasma Medicine: Cold Physical Plasma for Medical Application* (2018), pp. 43–70.

[19] Zhitong Chen et al. "Cold atmospheric plasma for addressing the COVID-19 pandemic". In: *Plasma Processes and Polymers* 19.9 (2022), p. 2200012.

[20] Iwona Niedźwiedź et al. "The state of research on antimicrobial activity of cold plasma". In: *Polish Journal of Microbiology* 68.2 (2019), pp. 153–164.

[21] T. Xia et al. "Inactivation of airborne viruses using a packed bed non-thermal plasma reactor". In: *Journal of Physics D: Applied Physics* 52.25 (2019), p. 255201. DOI: 10.1088/1361-6463/ab1466. URL: https://doi.org/10.1088/1361-6463/ab1466.

[22] Alina Bisag et al. "Cold atmospheric plasma decontamination of SARS-CoV-2 bioaerosols". In: *Plasma Processes and Polymers* 19.3 (2022), e2100133.

[23] Liyang Zhang et al. "In-duct grating-like dielectric barrier discharge system for air disinfection". In: *Journal of Hazardous Materials* 435 (2022), p. 129075.

[24] T Xia et al. "Inactivation of airborne porcine reproductive and respiratory syndrome virus (PRRSv) by a packed bed dielectric barrier discharge non-thermal plasma". In: *Journal of hazardous materials* 393 (2020), p. 122266.

[25] Jae-Seung Jung and Jin-Gyu Kim. "An indoor air purification technology using a non-thermal plasma reactor with multiple-wire-to-wire type electrodes and a fiber air filter". In: *Journal of Electrostatics* 86 (2017), pp. 12–17.

[26] Liang Yongdong et al. "Rapid Inactivation of Biological Species in the Air using Atmospheric Pressure Nonthermal Plasma". In: *Environmental Science & Technology* 46.6 (2012).

[27] Nachiket D Vaze et al. "Inactivation of bacteria in flight by direct exposure to nonthermal plasma". In: *IEEE transactions on plasma science* 38.11 (2010), pp. 3234–3240.

[28] V. R. Després et al. "Primary biological aerosol particles in the atmosphere: a review". In: *Tellus B: Chemical and Physical Meteorology* 64.1 (2012), p. 15598.

[29] J. Fröhlich-Nowoisky et al. "Review: Bioaerosols in the Earth system: Climate, health, and ecosystem interactions". In: *Atmospheric Research* 182 (2016), pp. 346–376. DOI: 10.1016/j.atmosres.2016.07.018.

[30] Byron J Lambert et al. "Sterility Assurance Across-Sectors—New Paradigms and Tools". In: *Frontiers in Medical Technology* 3 (2021), p. 622710.

[31] United States Environmental Protection Agency. *Ventilation and Air Quality in Non-Industrial Settings*. Tech. rep. EPA 402-K-02-005. Accessed: 2024-10-31. Environmental Protection Agency, 2021. URL: https://www.epa.gov/iaq.

[32] Francis F Chen. *Introduction to plasma physics*. Springer Science & Business Media, 2012.

[33] U. Kogelschatz. "Dielectric-barrier discharges: their history, discharge physics, and industrial applications". In: *Plasma Chem. Plasma Process.* 23 (2003), pp. 1–46. DOI: 10.1023/A:1022470901385.

[34] Y. Mu and P. T. Williams. "Recent advances in the abatement of volatile organic compounds (VOCs) and chlorinated-VOCs by non-thermal plasma technology: a review". In: *Chemosphere* 308 (2022). DOI: 10.1016/j.chemosphere.2022.136481.

[35] K. Ollegott et al. "Fundamental properties and applications of dielectric barrier discharges in plasma-catalytic processes at atmospheric pressure". In: *Chem. Ing. Tech.* 92 (2020), pp. 1542–1558. DOI: 10.1002/cite.202000075.

[36] Thu Minh Nguyen et al. "The outlook of flexible DBD-plasma devices: Applications in food science and wound care solutions". In: *Materials Today Electronics* 2023 (2023), p. 100087. DOI: 10.1016/j.mtelec.2023.100087.

[37] D. Cardenas S. Portugal B. Choudhury. "Advances on aerodynamic actuation induced by surface dielectric barrier discharges". In: *Front. Phys.* 10 (2022). DOI: 10.3389/fphy.2022.923103.

[38] K. Pai et al. "Investigation of the roles of plasma species generated by surface dielectric barrier discharge". In: *Sci. Rep.* 8 (2018), pp. 1–13. DOI: 10.1038/s41598-018-35166-0.

[39] G. Fridman et al. "Floating electrode dielectric barrier discharge plasma in air promoting apoptotic behavior in Melanoma skin cancer cell lines". In: *Plasma Chem. Plasma Process.* 27 (2007), pp. 163–176. DOI: 10.1007/s11090-007-9048-4.

[40] A. M. Jones and R. M. Harrison. "The effects of meteorological factors on atmospheric bioaerosol concentrations—a review". In: *Science of The Total Environment* 326.1-3 (2004), pp. 151–180.

[41] Malin Alsved et al. "Natural sources and experimental generation of bioaerosols: challenges and perspectives". In: *Aerosol Science and Technology* 54.5 (2020), pp. 547–571.

[42] Silvia G. Danelli et al. "Comparative characterization of the performance of bio-aerosol nebulizers in connection with atmospheric simulation chambers". In: *Dipartimento di Fisica – Università di Genova, INFN – Sezione di Genova* (2020).

[43] T. Reponen, S.A. Grinshpun, and K. Willeke. "Techniques for dispersing microorganisms into air". In: *Aerosol Science and Technology* 27.3 (1997), pp. 405–421. DOI: 10.1080/02786829708965478.

[44] G. Mainelis et al. "Collection of airborne microorganisms by bubbling into a non-toxic liquid." In: *Journal of Aerosol Science* 36.5 (2005), pp. 681–694. DOI: 10.1016/j.jaerosci.2004.12.007.

[45] H Zhen et al. "Evaluation of factors affecting culturable aerosol concentrations and bacterial culturability". In: *Journal of Aerosol Science* 70 (2014), pp. 67–79.

[46] Jean-François Doussin et al. *A Practical Guide to Atmospheric Simulation Chambers*. Springer, 2020.

[47] CH Technology. *Blaustein Atomizer (BLAM) Multi-jet Model User's Manual*.

[48] Christopher S Cox and Christopher M Wathes. *Bioaerosols Handbook*. CRC Press, 1995.

[49] WD Griffiths and IW Stewart. "Approaches to measuring bioaerosols exposure". In: *Applied Occupational and Environmental Hygiene* 14.10 (1999), pp. 669–676.

[50] David P Simon, Ting Han, and Gediminas Mainelis. "Improved liquid collection in bioaerosol samplers to minimize evaporation losses". In: *Journal of Aerosol Science* 92 (2016), pp. 55–62.

[51] T. Han, D.E. Fennell, and G. Mainelis. "Development and evaluation of an electrostatic precipitator-based bioaerosol sampler using field-collected organisms". In: *Journal of Aerosol Science* 81 (2015), pp. 53–66.

[52] X. Lin, K. Willeke, and S.A. Grinshpun. "Effects of sampling time and air humidity on the bioaerosol collection efficiency of impingers". In: *Aerosol Science and Technology* 30 (1999), pp. 215–228.

[53] C.-W. Chang, Y.-T. Ting, and Y.-J. Horng. "Collection efficiency of liquid-based samplers for fungi in indoor air". In: *Indoor Air* 29.3 (2019), pp. 380–389. DOI: 10.1111/ina.12535.

[54] Robert S Dungan and April B Leytem. "Impact of bioaerosols on health and productivity in animal agriculture: Current knowledge and future directions". In: *Journal of Animal Science* 94.6 (2016), pp. 2052–2064.

[55] Hao Zhen, Gediminas Mainelis, and William G Lindsley. "Membrane integrity assessment of airborne microorganisms". In: *Applied and Environmental Microbiology* 79.3 (2013), pp. 738–745.

[56] T. Han and G. Mainelis. "Design and performance evaluation of an electrostatic precipitator with superhydrophobic surface for bioaerosol collection". In: *Journal of Aerosol Science* 43 (2012), pp. 151–161.

[57] S. A. Grinshpun et al. "Control of aerosol contaminants in indoor air: combining engineering controls and personal protection equipment (PPE)". In: *Environmental Health Perspectives* 123 (2015), pp. 128–135.

[58] M. Yao and G. Mainelis. "Performance of portable microbial samplers at different flow rates under various environmental conditions". In: *Aerosol Science and Technology* 41.7 (2007), pp. 661–672.

[59] C.-W. Chang and F.-C. Chou. "Methodologies for quantifying bioaerosols". In: *Journal of Aerosol Science* 42.5 (2011), pp. 350–364. DOI: 10.1016/j.jaerosci.2011.01.005.

[60] Zhenzhong Wang, Klaus Willeke, and Sergey A Grinshpun. "Effect of long-term air sampling on the structural integrity of collected microorganisms". In: *Applied and Environmental Microbiology* 67.4 (2001), pp. 1639–1645.

[61] Estelle Levetin. "Sampling strategies for fungal bioaerosols". In: *Journal of Environmental Monitoring* 6.10 (2004), pp. 821–826.

[62] G. Mainelis and E. Tabayoyong. "Influence of sampling time on collection efficiency of bioaerosol samplers". In: *Aerosol Science and Technology* 44 (2010), pp. 1221–1231.

[63] R. L. Gorny. *Bioaerosol sampling methodologies: Past, present, and future*. Springer, 2020.

[64] Christopher S Cox and William G Lindsley. "Assessing microbial bioaerosols in cleanroom environments: Implications of microbial biodiversity for the performance of biotechnology facilities". In: *Aerosol Science and Technology* 51.3 (2017), pp. 115–127.

[65] B. Crook. "Review of methods to detect microbial contaminants in the environment". In: *Journal of Aerosol Science* 26 (1995), pp. 1289–1302.

[66] M. Yao and G. Mainelis. "Investigation of cut-off sizes and collection efficiencies of portable microbial samplers at different sampling conditions". In: *Aerosol Science and Technology* 41.6 (2007), pp. 516–524.

[67] S.L. Stewart, S.A. Grinshpun, and K. Willeke. "Effect of impact stress on microbial recovery on an agar surface". In: *Applied and Environmental Microbiology* 61 (1995), pp. 1232–1239.

[68] K. Willeke, X. Lin, and S.A. Grinshpun. "Improved aerosol collection by combined impaction and centrifugal motion". In: *Aerosol Science and Technology* 28 (1998), pp. 439–456.

[69] Chun-Chieh Tseng et al. "Optimization of Propidium Monoazide Quantitative PCR for Evaluating Performances of Bioaerosol Samplers for Sampling Airborne Staphylococcus aureus". In: *Aerosol Science and Technology* 48.12 (2014), pp. 1308–1319. DOI: 10.1080/02786826.2014.985780.

[70] C.R. Berry. "Electrostatic precipitation for the recovery of airborne Serratia marcescens". In: *Journal of Bacteriology* 41 (1941), pp. 215–220.

[71] Daniel Verreault, Sylvain Moineau, and Caroline Duchaine. "Methods for Sampling of Airborne Viruses". In: *Microbiology and Molecular Biology Reviews* 72.3 (2008), pp. 413–444. DOI: 10.1128/MMBR.00002-08.

[72] Jana Kesavan, Deborah Schepers, and Andrew R McFarland. "Sampling and retention efficiencies of batch-type liquid-based bioaerosol samplers". In: *Aerosol Science and Technology* 44.10 (2010), pp. 817–829.

[73] Bilal Sajjad et al. "Comprehensive insights into advances in ambient bioaerosols sampling, analysis and factors influencing bioaerosols composition". In: *Environmental Pollution* 322 (2023), p. 122473. DOI: 10.1016/j.envpol.2023.122473.

[74] Maria D King et al. "Assays and enumeration of bioaerosols-traditional approaches to modern practices". In: *Aerosol Science and Technology* 54.5 (2020), pp. 611–633.

[75] Frederick R. Blattner et al. "The Complete Genome Sequence of Escherichia coli K-12". In: *Science* 277 (1997), pp. 1453–1462. DOI: 10.1126/science.277.5331.1453.

[76] Sean C. David et al. "Stability of influenza A virus in droplets and aerosols is heightened by the presence of commensal respiratory bacteria". In: *Journal of Virology* 98 (2024), e00409–24. DOI: 10.1128/jvi.00409-24. URL: https://doi.org/10.1128/jvi.00409-24.

[77] Filopimin Andreas Dragonas. "Arbitrary Waveform Multilevel Generator for High Voltage High Frequency Plasma Actuators". PhD thesis. University of Bologna, 2014.

[78] AV Pipa et al. "Experimental determination of dielectric barrier discharge capacitance". In: *Review of Scientific Instruments* 83.7 (2012).

[79] Andrei V. Pipa and Ronny Brandenburg. "The Equivalent Circuit Approach for the Electrical Diagnostics of Dielectric Barrier Discharges: The Classical Theory and Recent Developments". In: *Atoms* 7.1 (2019). ISSN: 2218-2004. DOI: 10.3390/atoms7010014.

[80] Marcin Hołub. "On the measurement of plasma power in atmospheric pressure DBD plasma reactors". In: *International Journal of Applied Electromagnetics and Mechanics* 39.1-4 (2012), pp. 81–87.

[81] M Kuchenbecker et al. "Characterization of DBD plasma source for biomedical applications". In: *Journal of Physics D: Applied Physics* 42.4 (2009), p. 045212.

[82] AV Pipa et al. "The simplest equivalent circuit of a pulsed dielectric barrier discharge and the determination of the gas gap charge transfer". In: *Review of Scientific Instruments* 83.11 (2012).

[83] Floran Peeters and Tom Butterworth. "Electrical diagnostics of dielectric barrier discharges". In: *Atmospheric Pressure Plasma-from Diagnostics to Applications* (2019), p. 13.

[84] Hui Jiang et al. "Experimental study of QV Lissajous figures in nanosecond-pulse surface discharges". In: *IEEE Transactions on Dielectrics and Electrical Insulation* 20.4 (2013), pp. 1101–1111.

[85] Peter R Griffiths. "Fourier transform infrared spectrometry". In: *Science* 222.4621 (1983), pp. 297–302.

[86] Bruker. *FT-IR or IR Spectroscopy?* https://www.bruker.com/it/products-and-solutions/infrared-and-raman/ft-ir-routine-spectrometer/what-is-ft-ir-spectroscopy/difference-ir-vs-ftir.html.

[87] M. Y. Naz et al. "Optical characterization of non-thermal plasma jet energy carriers for effective catalytic processing of industrial wastewaters". In: *Scientific Reports* 11 (2021). ISSN: 2045-2322. DOI: 10.1038/s41598-021-82019-4.

[88] Lorenzo Ibba. *Characterization of low-temperature plasmas generated by dielectric barrier discharges for bacterial inactivation*. Tech. rep. EPFL, 2024.

[89] Elise Vervloessem et al. "NH3 and HNOx Formation and Loss in Nitrogen Fixation from Air with Water Vapor by Nonequilibrium Plasma". In: *ACS Sustainable Chemistry & Engineering* 11.10 (2023), pp. 4289–4298. DOI: 10.1021/acssuschemeng.3c00208.

[90] Klaas De Baerdemaeker et al. "Non-Thermal Plasma Decontamination Using a Multi-Hollow Surface Dielectric Barrier Discharge: Impact of Food Matrix Composition on Bactericidal Efficacy". In: *Foods* 12.2 (2023). DOI: 10.3390/foods12020386. URL: https://www.mdpi.com/2304-8158/12/2/386.

[91] Alexandra Waskow et al. "An In Situ FTIR Study of DBD Plasma Parameters for Accelerated Germination of Arabidopsis thaliana Seeds". In: *International Journal of Molecular Sciences* 22.21 (2021), p. 11540. DOI: 10.3390/ijms222111540. URL: http://dx.doi.org/10.3390/ijms222111540.

[92] Yukinori Sakiyama et al. "Plasma chemistry model of surface microdischarge in humid air and dynamics of reactive neutral species". In: *Journal of Physics D: Applied Physics* 45.42 (2012). DOI: 10.1088/0022-3727/45/42/425201. URL: https://dx.doi.org/10.1088/0022-3727/45/42/425201.

[93] Feng Zhang, Xiaojun Tang, and Lin Li. "Origins of baseline drift and distortion in Fourier transform spectra". In: *Molecules* 27.13 (2022), p. 4287.

[94] *HITRAN*. URL: https://hitran.tsu.ru/.

[95] Tetsuji Shimizu et al. "The dynamics of ozone generation and mode transition in air surface micro-discharge plasma at atmospheric pressure". In: *New Journal of Physics* 14.10 (2012), p. 103028.

[96] Min Cho et al. "Linear correlation between inactivation of E. coli and OH radical concentration in TiO2 photocatalytic disinfection". In: *Water research* 38.4 (2004), pp. 1069–1077.

[97] Fangzhou Liu et al. "Reactive air disinfection technologies: principles and applications in bioaerosol removal". In: *ACS ES&T Engineering* 3.5 (2023), pp. 602–615.

[98] S. Lu et al. "Photocatalytic inactivation of airborne bacteria in a polyurethane foam reactor loaded with a hybrid of MXene and anatase TiO2 exposing 001 facets". In: *Chemical Engineering Journal* 404 (2021), p. 126526. DOI: 10.1016/j.cej.2020.126526.

[99] C. Wang, S. Lu, and Z. Zhang. "Inactivation of airborne bacteria using different UV sources: Performance modeling, energy utilization, and endotoxin degradation". In: *Science of The Total Environment* 655 (2019), pp. 787–795. DOI: 10.1016/j.scitotenv.2018.11.266.

[100] S. S. Nunayon, H. Zhang, and A. C. K. Lai. "Comparison of disinfection performance of UVC-LED and conventional upper-room UVGI systems". In: *Indoor Air* 30 (2020), pp. 180–191. DOI: 10.1111/ina.12619.

[101] J. Lynn Heffron and Mayer. "Electrocoagulation as a Pretreatment for Electroxidation of E. coli". In: *Water* 11 (2019), p. 2509. DOI: 10.3390/w11122509.

[102] J. Wang, Y. Zhang, L. Kuang, et al. "Low-voltage driven Ag-Co3O4 textile device for multifunctional air cleaning". In: *Chemical Engineering Journal* 424 (2021), p. 130320. DOI: 10.1016/j.cej.2021.130320.

[103] M. Park, A. Son, and B. Chua. "Microorganism-ionizing respirator with reduced breathing resistance suitable for removing airborne bacteria". In: *Sensors and Actuators B* 276 (2018), pp. 437–446. DOI: 10.1016/j.snb.2018.08.133.

[104] M. Yao, G. Mainelis, and H. R. An. "Inactivation of microorganisms using electrostatic fields". In: *Environmental Science & Technology* 39 (2005), pp. 3338–3344. DOI: 10.1021/es048808x.

[105] G. Q. Gu, C. B. Han, J. J. Tian, et al. "Triboelectric nanogenerator enhanced multilayered antibacterial nanofiber air filters for efficient removal of ultrafine particulate matter". In: *Nano Research* 11 (2018), pp. 4090–4101. DOI: 10.1007/s12274-018-1992-1.

[106] F. Prehn, E. Timmermann, M. Kettlitz, et al. "Inactivation of airborne bacteria by plasma treatment and ionic wind for indoor air cleaning". In: *Plasma Processes and Polymers* 17 (2020), p. 2000027. DOI: 10.1002/ppap.202000027.

[107] J. H. Martínez-Montelongo et al. "Development of a sustainable photocatalytic process for air purification". In: *Chemosphere* 257 (2020), p. 127236. DOI: 10.1016/j.chemosphere.2020.127236.

[108] C. Wang et al. "Microwave-induced release and degradation of airborne antibiotic resistance genes (ARGs) from Escherichia coli bioaerosol based on microwave absorbing material". In: *Journal of Hazardous Materials* 394 (2020), p. 122535. DOI: 10.1016/j.jhazmat.2020.122535.

[109] W. C. Hinds. *Aerosol technology: properties, behavior, and measurement of airborne particles*. John Wiley & Sons, 1999.

[110] J. M. Blatny et al. "Airborne microorganisms and endotoxin in endotoxin-free clinical areas". In: *Indoor Air* 18.4 (2008), pp. 241–247.

[111] J. B. Morrow et al. "Critical Capability Needs for Reduction of Transmission of SARS-CoV-2 Indoors". In: *Frontiers in Bioengineering and Biotechnology* 9 (2021), p. 641599. DOI: 10.3389/fbioe.2021.641599.

[112] W. J. Fisk et al. "Economizer system cost effectiveness: Accounting for the influence of ventilation rate on sick leave". In: *IAQ applications* 4.3 (2003), pp. 7–11.

[113] A. J. Prussin II and L. C. Marr. "Sources of airborne microorganisms in the built environment". In: *Microbiome* 3.1 (2015), p. 78.

[114] C. B. Beggs. "The airborne transmission of infection in hospital buildings: fact or fiction?" In: *Indoor and Built Environment* 12.1-2 (2003), pp. 9–18.

[115] E. Noriega et al. "Cold atmospheric gas plasma disinfection of chicken meat and chicken skin contaminated with Listeria innocua". In: *Food Microbiology* 28.7 (2011), pp. 1293–1300.

[116] M. Laroussi. "Cold Plasma in Medicine and Healthcare: The New Frontier in Low Temperature Plasma Applications". In: *Frontiers in Physics* 8 (2020), p. 74. DOI: 10.3389/fphy.2020.00074.

[117] S. Perni et al. "Cold atmospheric plasma decontamination of the pericarps of fruit". In: *Journal of Food Protection* 71.2 (2008), pp. 302–308. DOI: 10.4315/0362-028X-71.2.302.

[118] James Kesavan, Sergey A Grinshpun, and Klaus Willeke. "Evaporation effects in liquid-based bioaerosol samplers". In: *Journal of Aerosol Science* 41.3 (2010), pp. 285–294.

[119] Huajun Zhen et al. "A systematic comparison of four bioaerosol generators: Affect on culturability and cell membrane integrity when aerosolizing Escherichia coli bacteria". In: *Rutgers University, Department of Environmental Sciences* (2020).

[120] Rob Bowers et al. "Sources of bacteria in outdoor air across cities in the midwestern United States". In: *Applied and Environmental Microbiology* 77.18 (2010), pp. 6350–6356.

[121] Susannah M Burrows et al. "Bacteria in the global atmosphere–Part 1: Review and synthesis of literature data for different ecosystems". In: *Atmospheric Chemistry and Physics* 9.23 (2009), pp. 9263–9280.

[122] B Marthi et al. "Survival of bacteria during aerosolization". In: *Applied and Environmental Microbiology* 56.11 (1990), pp. 3463–3467.

[123] Pierre Amato et al. "Microbial population in cloud water at the Puy de Dôme: Implications for the chemistry of clouds". In: *Atmospheric Environment* 87 (2015), pp. 87–95.

[124] Dario Massabò, Santiago Bernal, Simona Federici, et al. "ChAMBRe: A new atmospheric simulation chamber for aerosol modelling and bio-aerosol research". In: *Atmospheric Environment* 175 (2018), pp. 100–108.

[125] S Terzieva et al. "Collection of airborne microorganisms by a new electrostatic precipitator". In: *Aerosol Science and Technology* 25.4 (1996), pp. 426–436.

[126] Alexander Fridman. *Plasma chemistry*. Cambridge university press, 2008, pp. 866–874.